Ultrafast Submillimeter Dynamic Breast Imaging: A Foundation for Rapid Screening and Lesion Characterization

By
Jorge E. Jimenez

A dissertation submitted in partial fulfillment of the requirements for the Degree of

Doctor of Philosophy

Department of Medical Physics

University of Wisconsin – Madison
2018

Date of final oral examination: **06/04/2018**

The dissertation is approved by the following members of the final oral Committee:

Walter F. Block, Professor, Medical Physics

Sean B. Fain, Professor, Medical Physics

Edward F. Jackson, Professor and Chair, Medical Physics

Scott B. Reeder, Professor, Radiology

Roberta M. Strigel, Associate Professor, Radiology

TABLE OF CONTENT

DEVELOPMENT AND VALIDATION OF A 3D RADIAL DCE-MRI METHODOLOGY FOR AN ABBREVIATED BREAST SCREENING PROTOCOL

THESIS DISSERTATION

JORGE E. JIMENEZ, MS

PERFORMED UNDER THE SUPERVISION OF

ROBERTA M. STRIGEL, MD, MS

WALTER F. BLOCK, PHD

ABSTRACT

Dynamic contrast enhanced (DCE) MRI is the most sensitive imaging technique for detecting breast cancer. Unfortunately, breast DCE MRI is primarily recommended in patients at high risk for breast cancer. As a result, relatively few women benefit from breast MRI. Shortening MR breast imaging protocols is a key requirement to reduce cost and improve patient access to this powerful imaging tool for the detection of breast cancer. We developed a new technology for bilateral breast imaging that learns and models temporal behaviors through a local low rank (LLR) constraint that differs from previous approaches in breast MR iterative image reconstruction. We present an imaging methodology that delivers simultaneously higher spatial and temporal resolution than any previously published methods and a robust technology whose performance does not depend on lesion size, morphology or heterogeneity. Furthermore, we adopt an early enhancement phase approach which provides similar or more valuable information than the current methodology with a much shorter scan time.

We present an ultra-fast (10 s) volumetric bilateral breast MRI exam with 0.8 mm isotropic resolution, surpassing today's standard clinical resolution while providing temporal resolutions six-to-eighteen-fold faster. By simultaneously providing high spatial and temporal information of the brief but important early enhancement phase, we provide clinicians and researchers with the capability to extract

all the diagnostic and lesion characterization data possible from early enhancement phase. The goal for this project was to develop and demonstrate the feasibility of a high-performance sequence for abbreviated breast MRI. Though numerous accelerated methods have previously been proposed, very little validation of the information they derive has been generated due to the complexity of testing reconstruction methods and lesion-dependent imaging performance without a reference standard for comparison. We validated the effectiveness of the method to create high temporal fidelity in a digital phantom and demonstrated the feasibility of our proposed approach with 11 clinical subjects.

To my wife, Vanessa R. Jimenez

ACKNOWLEDGEMENTS

This work was financially supported by NIH R25 GM083252, K24 DK102595, T32CA009206, and F31CA217160, RSNA Research & Education Foundation, the Department of Radiology R & D Fund at the University of Wisconsin, Wisconsin Women's Health Foundation, the Science and Medicine Graduate Research Scholars and GE Healthcare.

Thank you to my advisor, Dr. Walter F. Block, whose patience and guidance made this PhD a reality. I am extremely grateful for Wally's support since the very beginning of the program, for the many hours in his office discussing how I could refine and improve my experiments, for all the encouragement when things did not work as planned but most importantly for showing me how to maintain a good balance between scientific endeavors and family. His tremendous optimism made the most stressful situations manageable for me. Many of my academic successes would not have been possible without him.

Thank you to my co-advisor, Dr. Roberta M. Strigel, for her support and understanding throughout these 5 years. Berta's willingness to work with me and her crucial role in the most clinical areas of my research helped me to cultivate an appreciation for interdisciplinary collaborations. From facilitating the recruitment of volunteers to reading manuscripts, her genuine care for my ideas and projects helped me become an independent researcher while building my confidence.

I would also like to thank Dr. Scott B. Reeder whose involvement and interest in my scientific growth was vital to my success in major keystones during my PhD program. Becoming a recipient of the R25 TEAM Science fellowship, awardee of a NIH F31 grant and acceptance to my post-doc/residency at MD Anderson Cancer Center are some accomplishments that would not have been possible without his support. Although our interactions were few, he was always there when I needed him and those memories I will take with me forever.

I am thankful for Dr. Sean Fain's kindness during my first year in the medical physics program. As a teacher for the MP 573 class, he made the necessary arrangements to provide accommodations for my learning disabilities. Small changes that made a huge impact on my educational development and paved the road for my success. More recently, as preliminary examination committee chair, he became a tremendous resource and his input into my work greatly improved this project. Likewise, I would also like to thank Dr. Edward Jackson, as a member for my preliminary examination and defense committee, for his support, advice and generous time.

Several friends and colleagues were incredibly important in guiding and training me during my first couple years of PhD. Daniel Gomez Cardona, Larry Hernandez, Miles Olsen, Erin Adamson, Jacob Macdonald, Kai Ludwig, Jacob Johnson and Jose Guerrero. I would like to specifically thank Dr. Leah Henze Bancroft for the many one-on-one training sessions from teaching me how to use an MRI scanner to the career advice that she gave me to save a lot of frustration and time. However, I am more grateful for her unconditional friendship. Likewise, Dr. Kevin M. Johnson for never turning me down the hundreds of times I asked for help coding PSDs or compiling the reconstructions. Kevin's remarkable skills as an MRI scientist not only inspired my project but also provided an invaluable source of knowledge.

My most sincere appreciation to my mother, Dora Alicia Jimenez Blanco, whose steady faith and love helped me believe that one day I would be able to become a scientist. I would also like to acknowledge the unequivocal trust from my parents-in-law, Ray and Jan Richards, who never question my decisions but, on the contrary, provide everything in their means to support my ambitions and dreams. Nonetheless, my deepest gratitude goes to my wife, Vanessa Richards Jimenez, who sacrificed so much so I could obtain this degree. Only a life time will be enough to thank her for going above and beyond during this 5 years of graduate school. Her encouragement to achieve academic excellence while enjoy life to its fulness provided me with an unlimited source of strength. Esther (5 years old), Alice (3

years old) and George Jimenez (1 year old) are just a testimony of that. Lastly, I would like to thank God for all his blessings and for making this miracle possible.

Jorge E. Jimenez

LIST OF FIGURES

LIST OF TABLES

INTRODUCTION

According to the American Cancer Society (ACS), breast cancer is the second most frequently diagnosed cancer among American women. Around 12.4% or 1 in 8 U.S. women will develop some form of invasive breast cancer over the course of her lifetime. In 2018, an estimated 266,120 new cases of invasive breast cancer are expected to be diagnosed, along with 63,960 new cases of non-invasive (in situ) breast cancer[1]. Furthermore, approximately 40,920 women in the U.S. are expected to die in 2018 from breast cancer, though death rates have been decreasing since 1989. Women under 50 have experienced larger decreases. These decreases are thought to be the result of treatment advances, earlier detection through screening, and increased awareness. Magnetic resonance imaging (MRI) of the breast has contributed to improved screening, diagnosis, and assessment of treatment response in patients with breast cancer[2].

MRI is a well-established medical imaging technology for breast, with a diverse variety of clinical applications, including the non-invasive differentiation between benign and malignant breast lesions, preoperative staging, detection of scar versus recurrence, implant assessment, and the evaluation of high-risk patients[78]. However, dynamic contrast-enhanced MRI is presently the most sensitive imaging technique for breast cancer diagnosis[3,4]. Currently, new methodologies are being developed to increase the adoption of MR in breast imaging, including the development of abbreviated protocols to improve patient access to this powerful imaging tool for the detection of breast cancer[5].

Motivation

Over the past 15 years, the clinical breast MR imaging community has become increasingly accustomed to examining the entire dynamic passage of an intravenous contrast injection with submillimeter resolution in at least two spatial dimensions. Increasingly, higher spatial resolution has become the standard-of-care through the use of modest temporal resolution, improved coil arrays, 3T imaging, and new MR acquisition methods. The information obtained from these dynamic contrast enhanced (DCE) exams has made MR the most sensitive imaging technique for detecting breast cancer, identifying a remarkable 14.7 additional cancers per 1,000 exams beyond the 11.4 detected by mammography alone in patients at high risk for breast cancer[6]. In contrast, large-scale efforts to supplement mammography with ultrasound screening have netted only an additional 2.7-3.9 cancers per 1,000 exams[6]. Clearly, there is a tremendous opportunity to improve breast cancer screening with MRI, but a significant cost differential steers screening methods towards ultrasound and digital x-ray tomosynthesis. Long and complicated MR breast protocols remain a key hindrance to reducing costs and improving patient access to a remarkable imaging technology for breast cancer detection.

Recent findings by two independent groups using abbreviated MR breast protocols that focus on the initial enhancement phase with modest spatial resolution have received significant interest. First, Kuhl et al[7]. maintained sensitivity to cancer detection with subtraction of a single pre-enhancement volume from a post-enhancement volume[7]. Second, studies of 7-second snapshots of the initial enhancement phase, despite clinically-significant loss of spatial resolution, demonstrated the value of higher temporal resolution during initial enhancement by obtaining statistically significant differences between benign and malignant lesions[8,9]. Thus any "loss" of the delayed dynamic contrast enhancement pattern through abbreviating the full protocol could potentially be balanced by detailed evaluation of the initial enhancement phase but requires high spatial resolution (submillimeter) AND high temporal resolution (less than 10 s) in the initial enhancement phase (less than 180 s), currently technically

impossible. Though promising, widespread clinical adoption of any abbreviated method will depend on 1) providing the high spatial resolution to which clinicians have become accustomed and 2) clinical validation that initial enhancement phase alone is sufficient compared with evaluation of the entire dynamic contrast enhancement pattern. Simultaneously achieving high spatial and temporal resolution requires subsampling spatial and temporal dimensions and then compensating for the missing data using a constrained reconstruction method. Though numerous accelerated methods have been proposed, very little validation of the information they derive has been generated due to the complexity of testing reconstruction methods and lesion-dependent imaging performance without a reference standard for comparison.

Objectives

We created an ultra-fast (10 s) volumetric bilateral breast MR imaging exam with 0.8 mm isotropic resolution, surpassing today's standard clinical resolution while providing temporal resolutions six-to-eighteen-fold faster. The fundamental basis for the proposed performance improvement was achieved by combining three techniques in a manner inspired by the recent Kuhl et al. work[7]: 1) A 3D radial acquisition that meets image reconstruction regularization requirements, 2) dynamic subtraction to provide the image sparsity needed to fuel local low rank (LLR) constraints of temporal behavior and 3) a second reconstruction using compressed sensing (CS) and fat/water separation to provide an anatomical map of the breast. We validated the effectiveness of the method to create high temporal fidelity in a digital phantom and demonstrate the feasibility of our proposed approach with 11 clinical subjects. This research built upon past success at the University of Wisconsin involving critical components of 3D radial MR sequences and fat/water separation developed by researchers at UW.

Aim 1. Validation of a 3D acquisition method with capabilities essential for accelerated breast MR imaging over the first 180 seconds of the initial enhancement phase.

Aim 2. Develop reconstruction algorithms with robust high spatiotemporal resolution.

- **2.1.** Develop constrained reconstruction with subtraction, CS and LLR capabilities.
- **2.2.** Benchmark 0.8-mm isotropic and 10 second spatiotemporal resolution using a digital phantom.

Aim 3. Demonstrate implementation feasibility of our technique with a pilot study of 11 patients with enhancing lesions comparing the clinical standard MRI protocol to our proposed abbreviated MR protocol.

Our methodology creates a foundation for a robust ultra-fast imaging technique with multiple applications. This new technology can be expanded to study the heterogeneity of tumor response during therapy, assess tumor biology, and ultimately predict prognosis and survival. However, we will first showcase it in a breast screening application, where we believe it can most quickly benefit the greatest number of women.

Summary of chapters

To summarize, the development and presentation of this dissertation is briefly detailed below and is organized into four sections:

Chapter 1: Fundamental concepts for breast MRI imaging and those relevant to this work are presented. An introduction to 3D radial trajectories, constrained reconstruction and fat/water separation is given and illustrated using experiments that preceded this work. Preliminary results are shown to further justify the rationale on some of the sampling and reconstruction parameters utilized in this dissertation project.

Chapter 2: The technological development for 3D radial abbreviated protocol for cancer screening is presented. A feasibility study for protocol validation that focuses only on the early enhancement phase of a DCE MRI scan is shown. In vivo images show the capabilities of the proposed SVIPR STELLR methodology for providing high spatiotemporal resolution and fat/water images using the same acquired data set and second reconstruction.

Chapter 3: A digital phantom is used to generate a realistic dynamic data set that matches in vivo observations seen in chapter 2. The dynamic data set (SVIPR) is then reconstructed using the STELLR approach along with 3 other reconstruction schemes. The STELLR reconstruction is compared against known truth from the digital phantom using quantitative measurements. The other three reconstructions are also compared against the digital phantom ground truth and used to illustrate the advantages of STELLR.

Chapter 4: An experimental non-Cartesian abbreviated protocol for breast screening is compared against a clinical Cartesian protocol. The non-Cartesian protocol consists of one 3D radial acquisition scheme and three reconstructions to provide all the information in the first 3-minutes of post-contrast. The clinical protocol is retrospectively created from a full diagnostic protocol using standard

of care sequences. Eleven patients were scanned in two different imaging sessions to show the value of the VIPR abbreviated protocol.

Chapter 5: The results of this dissertation are summarized, and future work is discussed

Chapter I BACKGROUND

1 MRI IN BREAST IMAGING

Portions of this chapter have been previously presented at the 2015 and 2016 annual meetings of the International Society for Magnetic Resonance in Medicine (ISMRM).

1.1 Clinical Breast MRI

Magnetic resonance imaging (MRI) has become a ubiquitous technology in modern medical imaging. High contrast between soft tissues and non-ionizing radiation are two main characteristics that have contributed to its high adoption among multiple medical applications. The first reported use of MRI in breast tissue to examine pathology occurred in 1973[10]. However, it was not until 1986, when contrast agents were used to differentiate between malignant and healthy tissue, that MRI received more attention[11]. Since then, numerous technological innovations have been developed to enhance the usefulness of MRI in breast imaging, including the introduction of dedicated breast coils in 1985[12]. The first MRI Scanner was approved by the FDA in 1984 as a Premarket Approval (PMA) process for a class III device. Gadolinium-based contrast agents (GBCAs) received FDA clearance in 1988 and still are the only FDA-approved contrast agents for evaluation of the breast. Finally, in 1991 MRI was reclassified for use as a supplement to mammography to diagnose breast cancer[13].

The Centers for Medicare and Medicaid Services (CMS) began reimbursing for breast MRI in November 1985. Although no National Coverage Determination (NCD) was given specifically for contrast MRI, legislation in 2000 directed the Health Care Financing Administration to create separate billing codes for contrast agents and imaging procedures, which allowed CMS to pay for these separately. Since 2012, as a result of the Medicare Improvements for Patients and Providers Act of 2008 (MIPPA), facilities are required to use breast coils in order to receive Medicare reimbursements for

breast. Although today most insurers reimburse for breast MRI exams, the implementation of breast MRI is primarily limited to patients at elevated risk for breast cancer and patients with a known diagnosis of breast cancer who are undergoing staging and extent of disease evaluation, partially because of the high cost.

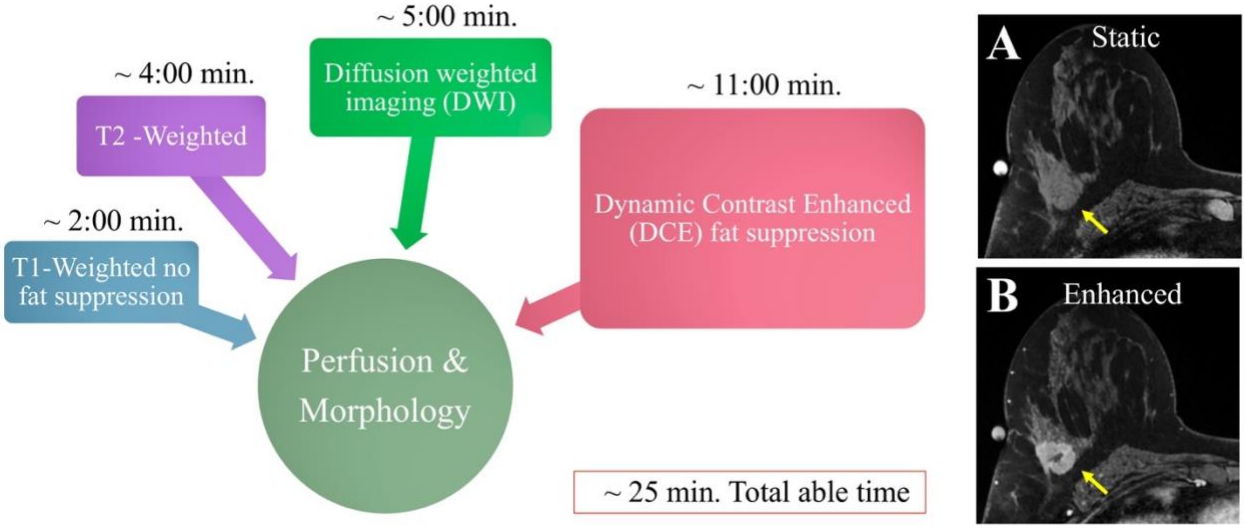

Figure 1.1 *Graphical representatin of a diagnostics MRI breast exam (left). A) Image acquired before contrast (static). B) Image acquired after contrast injection. Yellow arrows indicate the cancerous tumor.*

A common breast MR protocol consists of a series of scans with an average table time of 25 minutes (Figure 1.1). Typically, a protocol will include a T2-weighted sequence, a T1-weighted sequence without fat suppression, a dynamic contrast enhanced (DCE) T1-weighted sequence with fat suppression, and more recently, a diffusion weighted imaging (DWI) sequence. The most important part of the protocol is the DCE exam because it allows for a dramatic contrast difference between healthy and abnormal tissue (Fig. 1.1A-B). A time series is acquired as the contrast perfuses within the breast. The frame rate between time measurements is dictated by the imaging capabilities of the MR system, including hardware and software. Typically, clinical breast DCE MR exams have temporal resolutions on the order of 60-180 seconds[14,15].

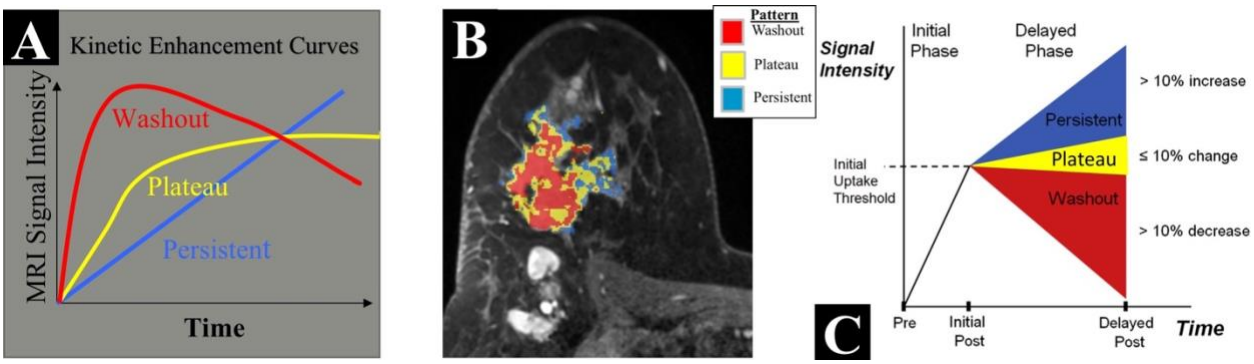

Figure 1.2 *A) Type of kinetic curves generated from breast lesions after contrast injection: persistant, plateau and washout. B) Unilateral visualzatiion of the breast with color kinetic overlay analysis. C) Graphical representation of clinical enhancement classification, which is simplistic due to low clinical temporal resolution.*

Standard-of-care clinical strategies rely on a long MRI acquisition session to evaluate lesion perfusion over 6-11 minutes (Fig. 1.2). The temporal kinetic analysis is performed based on two methods. The first approach attempts to qualitatively classify the signal intensity (SI) of breast lesions into a wash-in, plateau, wash-out model (Fig. 1.2C). The classified shape of the signal intensity time curve is then used to improve specificity for breast cancer[16]. Due to its simplicity, this method has been widely used in clinical practice since the technical demands are limited and it can be achieved in routine practice. The second primary approach is pharmacokinetic (Pk) modeling of gadolinium contrast dynamics, which requires a higher temporal resolution than what most clinical strategies can provide (Fig. 1.3). In addition, the interpretation is computationally demanding and lacks clinical standardization for analysis and interpretation[17]. However, some studies of Pk modeling have shown promising results for the quantitative evaluation of tumor response, biology assessment and prediction of prognosis and survival.

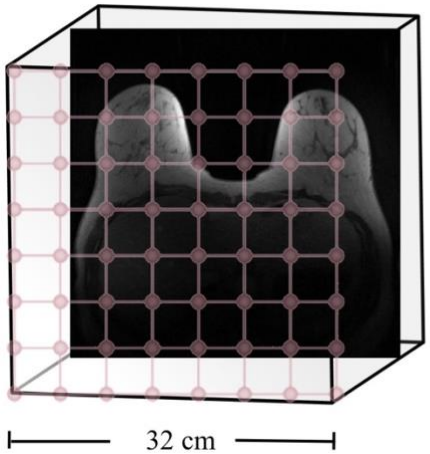

Nyquist criterion for 32 x 32 x 24 cm bilateral FOV:

$$\frac{320\times320\times240\ mm^3}{(0.8\ mm)^3} = 48\times10^6\ samples$$

MRI system sampling rate:

$$500\ KHz_{\ Max} \times 10\ s \times 0.5 = 2.5\times10^6 \text{ samples}$$

Undersample rate:

$$\frac{48\times10^6 \text{ samples}}{2.5\times10^6 \text{ samples}} = \textbf{19.2 R}$$

Figure 1.3 *A bilateral breast exam (320 mm FOV) acquiring data during 50% of the TR interval at a 500 kHz sampling rate and a 10 second frame interval would need a 19x factor of acceleration to achieve the minimum temporal performance for pharmacokinetic modeling implementation. Parallel imaging today can achieve only factors of approximately 4 in clinical practice. Considerable innovation within the development of this project describes how to achieve the needed R factor of 19.*

1.2 Radial Trajectories

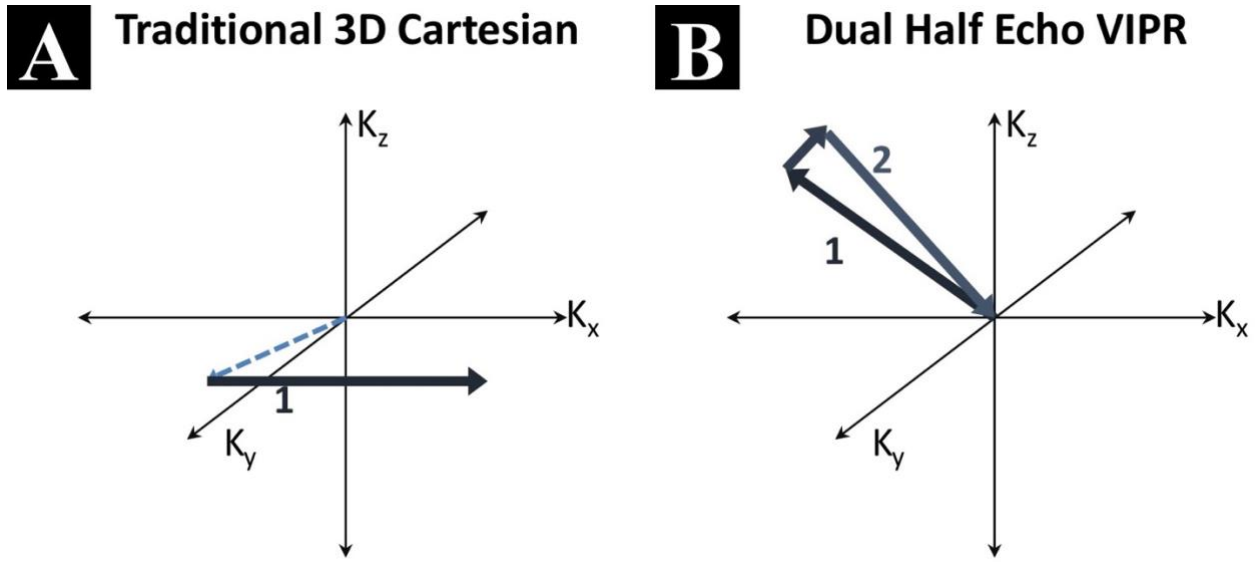

Figure 1.4 *Sampling trajectory comparison. A) Cartesian trajectories need to "walk" through k-space to find the assigned phase encode location before turning on the radiofrequency receiver (RFC) to acquire data. B) Radial trajectories start sampling k-space right after the excitation pulse. In a dual half echo trajectory, the center of k-space is sampled twice every TR while the Cartesian trajectory allows for only one sample in the entire trajectory.*

Although radial sequences were the first to be used in MRI, Cartesian trajectories have become more popular and now they are the prevailing choice for clinical applications. This is primarily due to the development of discrete fast Fourier transform (FFT) used for conversion from the Cartesian grid to image space and the limited computing power available in the early years of MRI to perform the computational analysis needed for non-Cartesian imaging. However, non-Cartesian trajectories, such as radial, have their known advantages over Cartesian trajectories. For instance, they are more efficient at sampling k-space (Fig. 1.4), reducing scan time and increasing temporal performance in a dynamic acquisition. Radial sampling schemes start acquiring information immediately after the radiofrequency (RF) excitation pulse, unlike Cartesian sampling which must first stablish the correct phase encode location. Furthermore, they are able to sample the center of k-space, where most of the contrast information is contained, during every repetition time (TR). Lastly, a multi-echo approach can be

adopted to sample more data with a single TR or to meet timing criteria for post-processing algorithms such as fat/water separation.

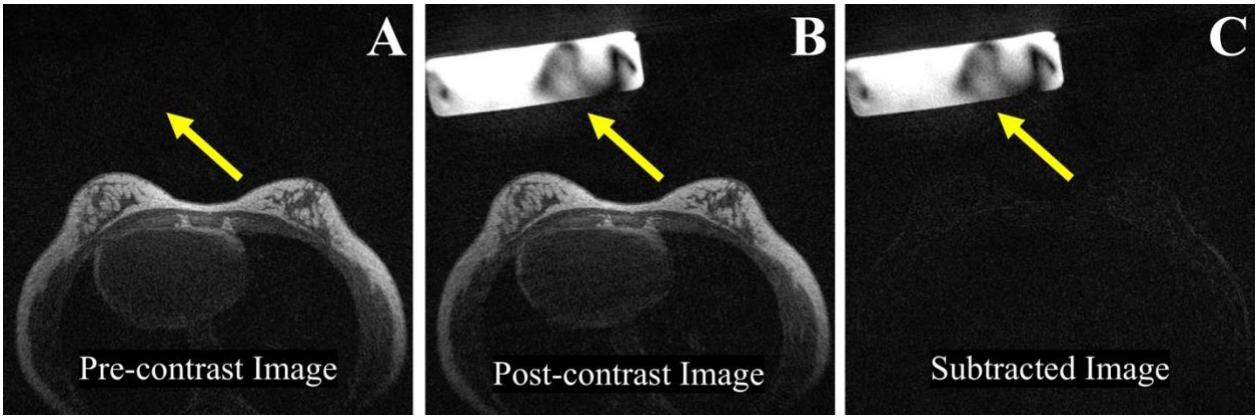

Figure 1.5 *DCE T1-weighted subtraction simulation using a volunteer and a water phantom. Pre- and post-contrast images were simulated with the addition of a water phantom at the bottom of the breast coil between scans (yellow arrows). The resultant subtracted image is shown in C, where little signal from static tissue can be observed. Subtraction is able to increase sparsity within DCE images, allowing visualization of only the enhancing tissue (water phantom).*

Another inherent advantage of radial sampling is robustness to motion artifacts. Although less respiratory motion is seen in breast MR due to prone positioning of the patient compared with supine positioning for most applications, motion artifacts are still a concern in breast imaging, including from the heart which is in the field-of-view (FOV). Radial trajectories are less susceptible to motion, particularly 3D radial sequences where the signal phase change due to motion is spread throughout three diminutions. Such benefits are of particular interest in breast DCE MR exams, where subtraction plays a key role in the interpretation process. An example of subtraction with a 3D radial trajectory is shown in Figure 1.5. The additional sparsity created by a robust subtraction technique can be further exploited by a sparse reconstruction such as compressed sensing (CS).

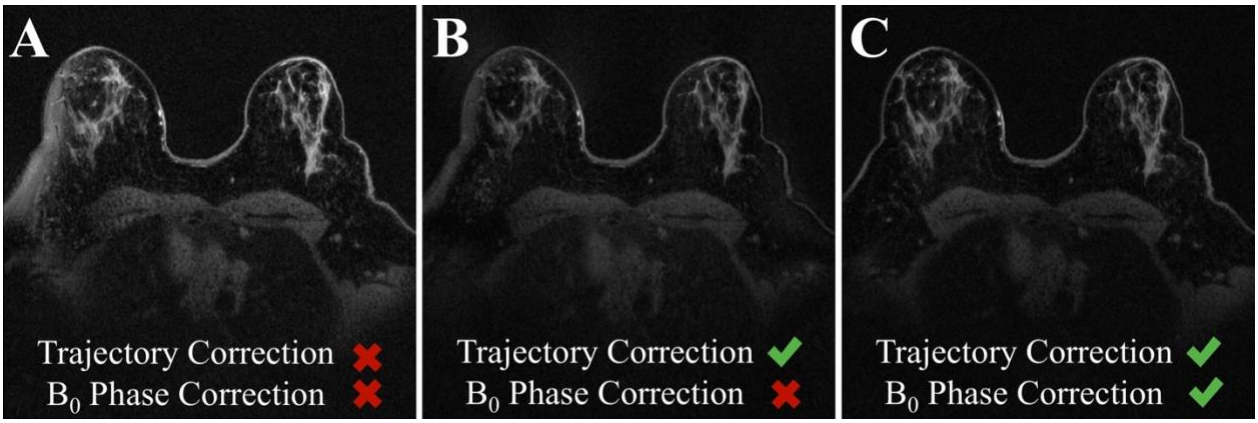

Figure 1.6 *In vivo rendering of three reconstructions. A) 3D radial trajectory with no calibration corrections. B) Same data set with addition of linear eddy current corrections. C) Reconstructed image with linear eddy current and phase correction from calibration pile. The 3D radial high sensitivity to eddy currents from the gradients are shown in A. Therefore, effective calibration is required to produce an aceptable radial MR image.*

Unfortunately, advantages of radial trajectories do not come without limitations. 3D radial sampling achieves a high performance by aggressively ramping on and off the MRI gradients to their limit, i.e., the maximum slew rate. The rapid changes in the magnetic field generate linear eddy currents which translate into phase change in the signal. The difference in accrued phase, $\Delta\varphi$, can be measured in a calibration test before or after the scan using two separate slices a known distance apart for each axis and is given by this equation:

$$\Delta\varphi_r(t) = \int_0^t \gamma \cdot G_r(t) \cdot D_r \cdot dt = D_r \cdot k_r(t),$$

where r is the encoding direction (x, y, or z), γ is the gyromagnetic ratio, G_r is the spatial encoding gradient amplitude, D_r is the slice distance to gradient isocenter, and k_r is the k-space trajectory. The calculated $\Delta\varphi_r(t)$ is used to correct for the linear eddy currents in all three axes. Furthermore, non-Cartesian trajectories are highly sensitive to variable system delays. The discrepancy between the real-time frequency demodulation hardware and the receiver results in an incorrect representation of each k-space data sample location. The real-time frequency demodulation signal,

$$\Delta f(t) = \gamma(G_x(t)d_x + G_y(t)d_y + G_z(t)d_z)$$

is used to center the image at a position d_x, d_y and d_z from the nominal k-space locations. The calculated $\Delta f(t)$ is used to correct the "delayed" k-space location. The effects from phase errors due to linear eddy current and trajectory deviations due to hardware delays can be appreciated in Figure 1.6A. The significant image improvement when a calibration correction is applied is shown in Fig. 1.6B-C.

Despites these two disadvantages, arguably the major reason for the slow adoption of radial trajectories into clinical application is the intensive computing required to reconstruct such data sets. Most of the computing time is dedicated to the gridding of k-space as part of a non-uniform Fourier transform (NUFFT). Currently, no major MRI vender provides a non-Cartesian product sequence for breast MRI. Nevertheless, due to the dramatic increase of computing capabilities in modern MRI hardware and the fast adoption of graphic processing units (GPU) for reconstructions, the clinical adoption of non-Cartesian trajectories is expected to grow.

1.3 Constrained Reconstructions

First proposed for image compression, compressed sensing was adopted by MRI in 2007 when Lustig et al.[18] presented their first work. CS is founded on the premise of reconstructing an image from an incompletely filled k-space by assuming prior knowledge and constraining the underdetermined system to be solve as an optimization problem. There are two characteristics that the data need in order to fulfill the CS requirements: sparsity and incoherence. In a more rigorous description, CS states that a known sparse signal $\boldsymbol{x}$ can be recovered from an underdetermined series of linear measurements $y := A\hat{\boldsymbol{x}}$ which is against the Shannon-Nyquist sampling theorem if A is populated with random entries and the $spark(A)$, smallest number of columns of A that are linearly dependent, is greater than twice the number of undersampled measurements in $\hat{\boldsymbol{x}}$. Then a suitable solution to recover $\boldsymbol{x}$ can be found by the following minimization problem:

$$\hat{\boldsymbol{x}} = arg.\ min. \|\boldsymbol{x}\|_0 \qquad s.t. \qquad y = A\boldsymbol{x}.$$

In practice, ℓ_0-solutions are difficult to compute since the ℓ_0-norm is non-convex. However, establishing the Restricted Isometry Property (RIP) for matrix A guarantees that the solution to the ℓ_1-minimization problem is equivalent to the solution to the ℓ_0-minimization problem. Therefore, the problem becomes more manageable.

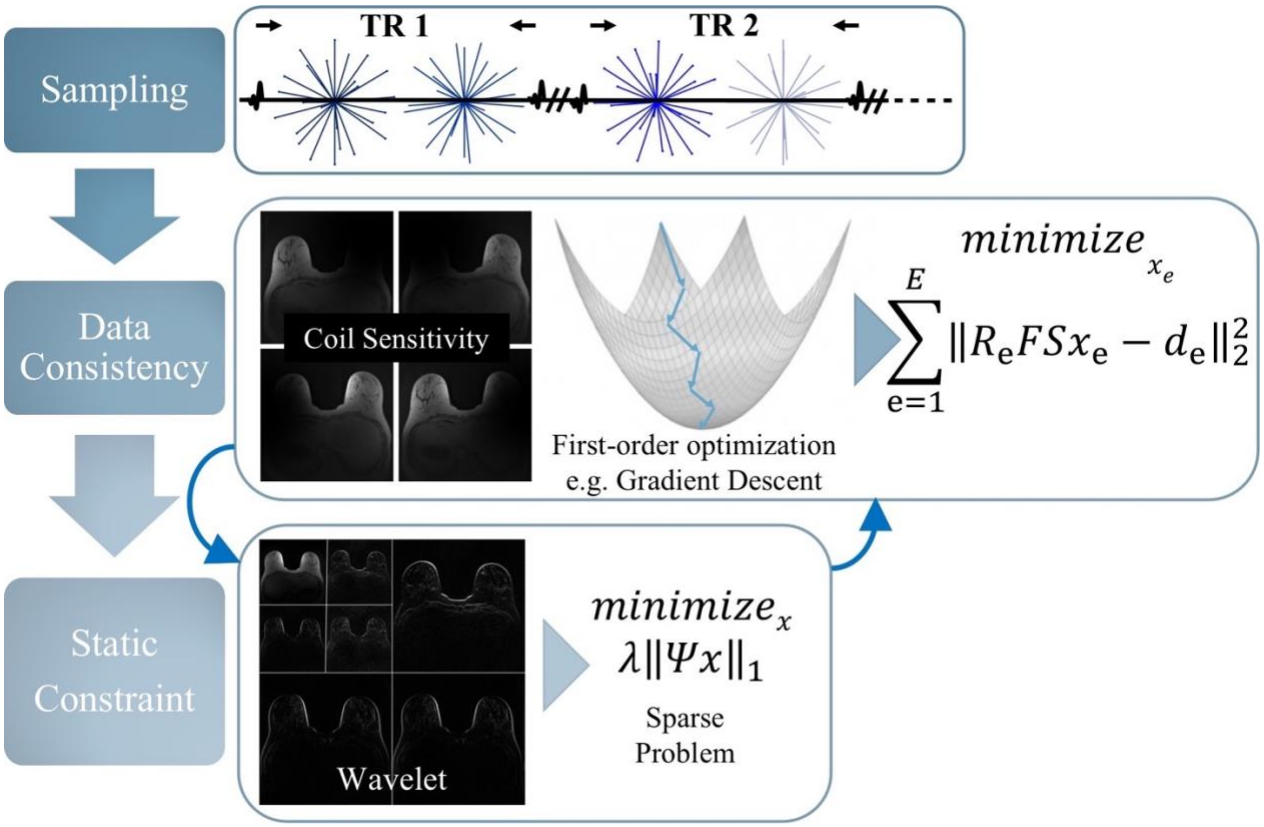

Figure 1.7 *Pictoral overview of CS reconstruction. Four unique radial samplings at four echo times within 2 TRs are acquired. There are two main steps: data consistency and spatial constraint. First, a gradient descent algorithm is used to optimize the reconstuction. Second, an L_1-norm-based shrinkage function is used to enforce sparsity. The iteration between these two steps continues until an error magnitude is achieved allows for the improvement of the image without losing important infromation.*

Radial trajectories are an attractive alternative for compressed sensing due to the inherent presence of incoherent aliasing artifacts in multiple dimensions, even for regular undersampling, which enables us to exploit additional sparsity and incoherence along frequency-encoding dimensions (not feasible in Cartesian sampling). Usually, CS reconstructions are designed based on a Projection Over Convex Sets (POCS)-type algorithm to produce an alternating method between two or more close-convex sets[19]. Standard CS implementations alternate between a data consistency step and sparse constraint (Fig. 1.7). Such steps are described by the two terms inside the following optimization problem:

$$\min_x \ \|DFSx - d\|_2 + \lambda\|\Psi x\|_1$$

where x is the combined image from all coils), D is a subsample operator, F is Fourier encoding, S represents the coil sensitivities and d is the measured k-space data. The first part of the equation refers to the data consistency portion of the reconstruction in which the benefits of parallel imaging, Figure 1.8, are exploited through a gradient descent-based algorithm. The second term describes the spatial constraint using the ℓ_1-norm ($\|x\|_1$). A wavelet transform (Ψ) is commonly used as sparsifying encoder. Lastly, λ represents the weighting of the sparse constraint. However, it is important to emphasize that an unbalanced weighting can lead to artifacts (Fig. 1.9).

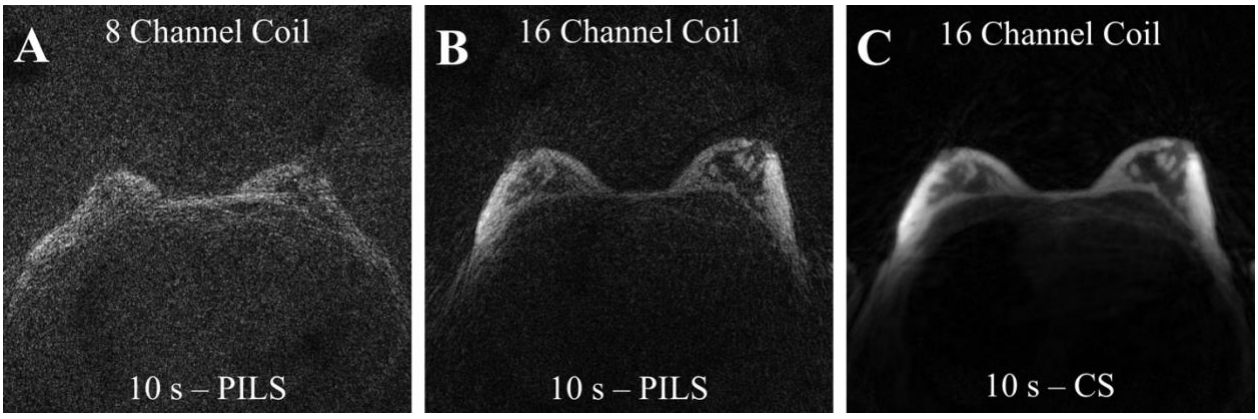

Figure 1.8 *10 seconds of k-space data were acquired and reconstructed with varying hardware and software arrangements. A) Aquisiton with an 8-channel breast coil and reconstructed using parallel imaging; high noise levels are visible due to the 45X undersample rate at the edge of k-space and some streaking artifacts are noticeable as well. B) Aquisition with a 16-channel breast coil and reconstructed using only parallel imaging, reduction in noise and undersampling artifacts are noticeable. C) The same 10 seconds of data from B were reconstructed using compressed sensing. Dramatic noise reduction is achieved and streaking artifacts are not evident, although there is not enough detail present in the image to resolve structural details inside the breast.*

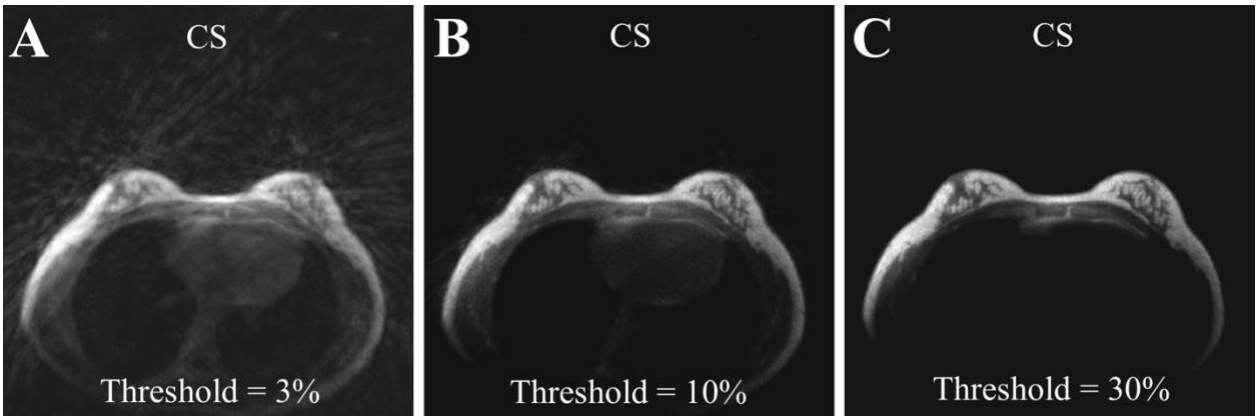

Figure 1.9 *Comparison between three CS reconstuctions with three different thresholding values using 3 minutes worth of static data. Fractional thresholding of 3% (A), 10% (B) and 30% (C) were used. The 3% value is too small and consequently generates overfitting errors while the 30% is too aggresive and overgeneralization errors are present. Overfitting leads to model the noise as part of the important information while the overgeneralization creates losses of subtle contrast or small important features in the image.*

Sparse reconstructions such as CS benefit from high dimensional problems in which data redundancy can be exploited even further. CS theory states that the minimum required amount of data to recover an image decreases when the dimensionality of the data set increases as long as the measurements fulfill the criteria explained above. As a result, CS algorithms are able to deliver greater performance with dynamic (4D) data set where there is abundant redundancy between temporal measurements. Although a 4D CS reconstruction is expected to deliver better performance than a 3D CS reconstruction, there are other temporal constraints that have shown superior results under certain circumstances. Low-rank models are one of them.

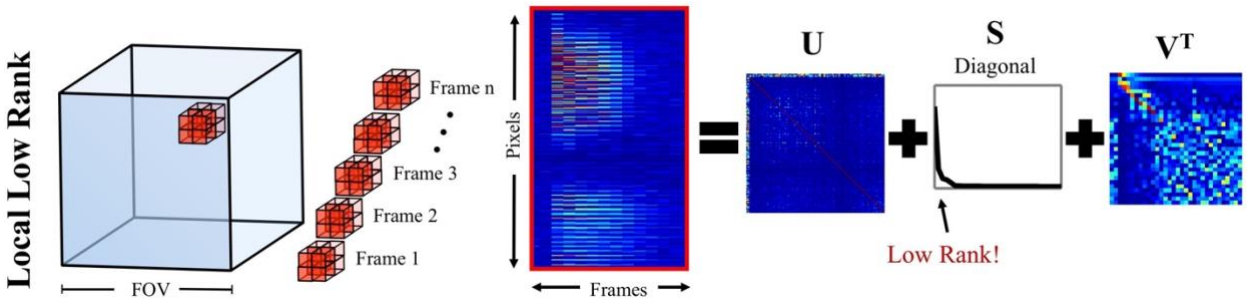

Figure 1.10 *Local low-rank work flow diagram for a temporal constraint. The 3D set is broken into smaller sub-blocks (red cubes). The pixels from the sub-block at all acquired time points are rearranged into a single matrix where the columns represent individual single pixel locations and the rows containts their kinetic behavior. A SVD is used to decompose the signal into spatial and temporal components.*

Temporal components are then utilized to constrain the acquired data set. This process is repeated until the entire volume is covered in every iteration.

Unlike CS, low-rank methods rather than surmising sparsity in an already predetermined domain (e.g. wavelet domain) are data driven. Low-rank uses a singular-value decomposition (SVD) factorization to estimate or essentially "learn" an optimal domain for a given data set in which the information can be low-rank. In certain circumstances, these learned domains are able to represent the information with a higher degree of sparsity than in the wavelet domain. Subtracted dynamic information is an example of such data sets. However, there is one limitation: if the number of independent enhancing patterns is high, then temporal "rank" of the system will not be small. Alternately, a local low-rank (LLR) approach minimizes this limitation by enforcing only a temporal constraint in one sub-area of the image individually (Fig. 1.10). If even the rank of a dynamic set is high, each individual sub-area is able to maintain a relative low-rank, which is required for these algorithms to work. The addition of a temporal LLR constraint to a CS problem can be defined as:

$$\min_{\mathrm{x}} \ \|\mathrm{DFSx} - \mathrm{d}\|_2 + \lambda_{CS}\|\Psi \mathrm{x}\|_1 + \lambda_{LLR}\sum_{\mathrm{b}=1}^{\mathrm{N_b}}\|\mathrm{C_b x}\|_*$$

The third term defines the local temporal constraint part, where C_b refers to an operator that selects image blocks throughout all T temporal volumes. The number of blocks by which the volume is sub-divided N_b, and $\|x\|_*$ is the nuclear norm of a matrix A[20]. Variables $\boldsymbol{\lambda_{CS}}$ and $\boldsymbol{\lambda_{LLR}}$ are regularization parameters to weigh the relative importance of global constrained spatial and local temporal constraint, respectively. A diagram of a dual constraint reconstruction can be seen in Figure 1.11.

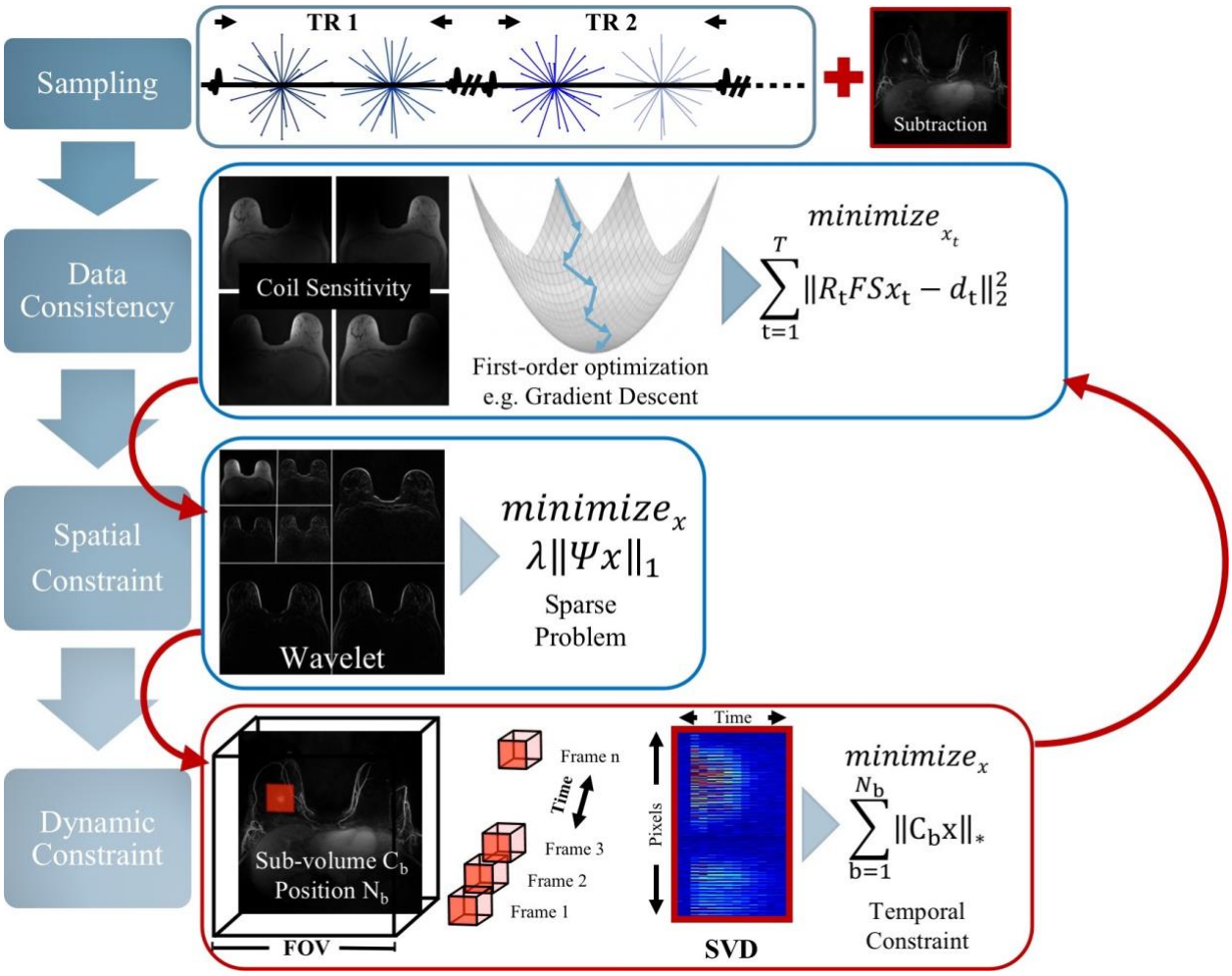

Figure 1.11 *Pictoral overview of iterative reconstruction with two constraints. Four unique radial samplings at four echo times within 2 TRs are acquired. A data consistency constraint uses parallel imaging principles to offset high undersampling. An L1 minimization (CS) is used as the first constraint through a global thresholding to improve depiction of the breast architecture. An LLR constraint along the temporal dimension is used to exploit the data redundancy between time points.*

1.4 Fat/water Separation

Fat suppression is required in breast MRI due to the high T1-weigheted signal of fat, which makes it difficult to differentiate from contrast enhancement in potential breast lesions. One efficient way to solve this difficulty is subtraction, which is widely used in clinical practice. Another solution is the use of radiofrequency (RF) pulses to excite the fatty tissue in a timely manner in order to suppress the fat signal. RF fat suppression approaches in the presence of homogenous magnetic field (B_0) are able to produce suitable results (Fig. 1.13A). Nonetheless, preserving a homogeneous B_0 over the large field-of-view (FOV) required to image bilateral breasts is challenging. Inhomogeneities in B_0 diminish the efficacy of the fat suppression RF pulses (Fig. 1.13B). Even with modern advances in hardware capabilities that allow for the development of water-only excitation pulses, inhomogeneous B_0 reduces the robustness of this approach.

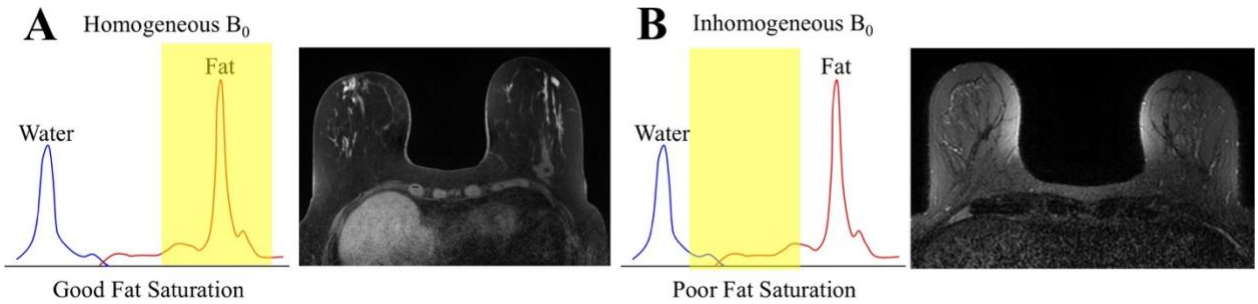

Figure 1.12 *T1-weighted breast images with with fat suppression in a homogeneous (a) and inhomogeneous magnetic field. The fat exitation pulse is able to effectely suppresed only the fat peak when the B_0 field is uniform. In contrast, the inhomogeneity "shift" the fat exitation pulse such that it only exites a portion of the fat peak and part of the water signal.*

The idea of acquiring fat and water signals together to later separate them into two images was first presented in 1984 by Dixon et al[21]. Dixon-based methods require at least two measurements: an image with fat and water in phase and another image where fat and water are out of phase. Then, a simple linear matrix multiplication is used to produce a fat and water image. Successful methods have been developed that are able to correct for B_0 inhomogeneities. Reeder et al. proposed in 2005 a fat/water decomposition method with an Iterative Decomposition with Echo Asymmetry and Least squares estimation (IDEAL)[22]. Although IDEAL provides more flexibility over echo timing, since it is not

limited to in and out of phase images, Cartesian trajectory applications in the breast compromise spatial resolution to achieve proper TEs. Alternatively, a 3D radial trajectory with its efficient sampling is able to increase imaging performance, thus expanding the range of echo selections. For instance, an implementation of fat/water decomposing using IDEAL in combination with a 3D radial trajectory was proposed in 2014[23]. The problem can be represented as a linear system of linear equation:

$$\boldsymbol{A}\rho(r) = s_n(r)$$

where $\boldsymbol{A}$ is a predicted phase model using water as reference, $\rho(r)$ the species in which the signal is going to be decomposed (water and fat) and $s_n(r)$ is the fat/water combined images. This can be written in more conventional linear algebra style as:

$$\begin{pmatrix} 1 & e^{i\theta_1} \\ 1 & e^{i\theta_2} \\ 1 & e^{i\theta_3} \\ 1 & e^{i\theta_4} \end{pmatrix} \cdot \begin{pmatrix} W \\ F \end{pmatrix} = \begin{pmatrix} TE_1 \\ TE_2 \\ TE_3 \\ TE_4 \end{pmatrix}$$

The chemical shift experienced by the fat in each echo time, $e^{i\theta_n}$, is defined as:

$$e^{i\theta_n} = \sum_{m=1}^{M} \rho_m \, e^{-i2\pi\Delta f_m t_n}$$

which is the summation of spectral peaks with a chemical shift, Δf_m, among the total number of included peaks, M, and then scaled by the contribution fraction of each peak (ρ_m). Then, a Moore-Penrose pseudo-inverse of matrix $\boldsymbol{A}$, represented with the symbol +, can be multiplied by the B_0-corrected images to decompose the signal from the four echoes into fat and water images:

$$\begin{pmatrix} W \\ F \end{pmatrix} = \begin{pmatrix} 1 & e^{i\theta_1} \\ 1 & e^{i\theta_2} \\ 1 & e^{i\theta_3} \\ 1 & e^{i\theta_4} \end{pmatrix}^{+} \cdot \begin{pmatrix} TE_1 \\ TE_2 \\ TE_3 \\ TE_4 \end{pmatrix}$$

IDEAL iteratively calculates a B_0 map that fits the signal model within a small margin of error in order to improve fat/water decomposition. However, the successful decomposition of species relies

on an adequate echo selection. Cramér-Rao bounds analysis can be used to determine optimal TEs that produce the highest estimated number of signals averaged (NSA) for a four-point method. Figure 1.13 shows three echo selections, in which the 0.852 milliseconds delay between TRs allows for the best imaging performance (smallest TR) while maintaining a relatively high NSA. In vivo image reconstruction, Figure 1.14, confirmed the theoretical results from the simulations.

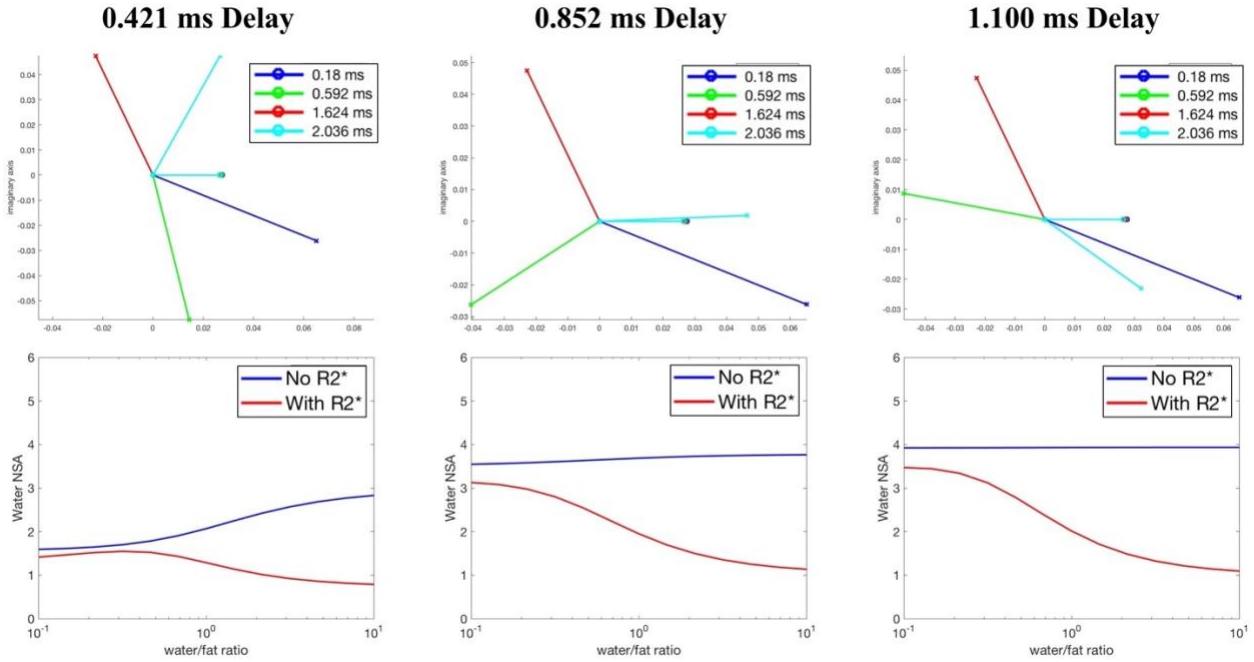

Figure 1.13 *Echo times analysis for four-point Dixon method.* ***Top:*** *Complex plot showing echo phase at three different TEs.* ***Bottom:*** *Cramér-Rao bounds analysis to identify optimal TEs that produce the highest estimated number of signals averaged (NSA) for our four- point method.*

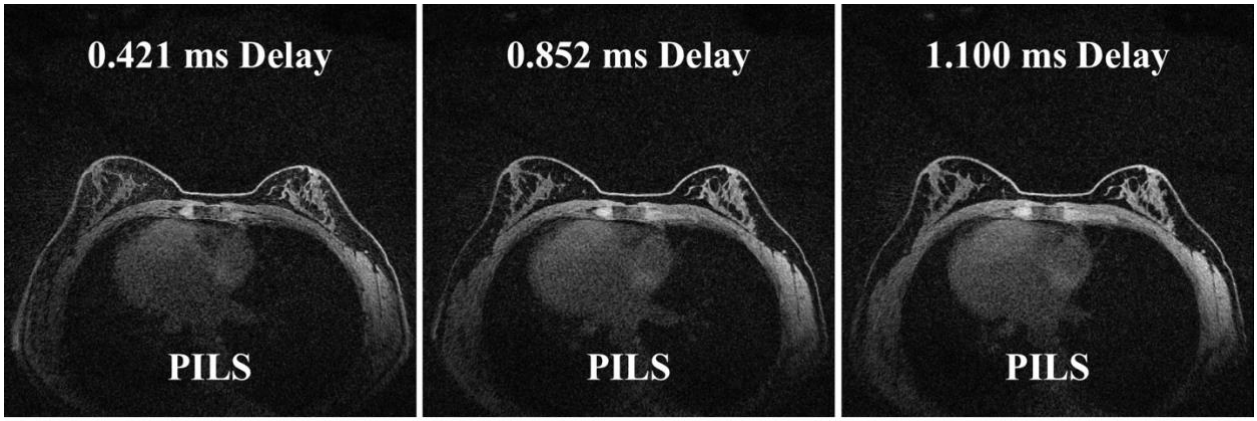

Figure 1.14 *Reconstruction of in vivo water images using IDEAL and three different echo delays. All reconstrucions were performed with parallel imaging (PILS). The 0.421 ms delay produced a none-uniform far/water separation while 1.100 ms produce the best results. However, 0.852 allows for a*

relative good compromise between image quality and image performce since this delay let us maintain a relatively small TR of 4.3 ms.

Finally, IDEAL fat/water separation can take advantage of higher channel count arrays and iterative reconstructions. First, increasing the number of coils in a breast coil can impact IDEAL performance in two ways: increasing SNR when the acquisition stays constant (Fig. 1.15) or reducing the scan time required to achieve a comparable image. Faster acquisition allows for greater flexibility in echo selection or makes it possible to achieve higher spatial resolution.

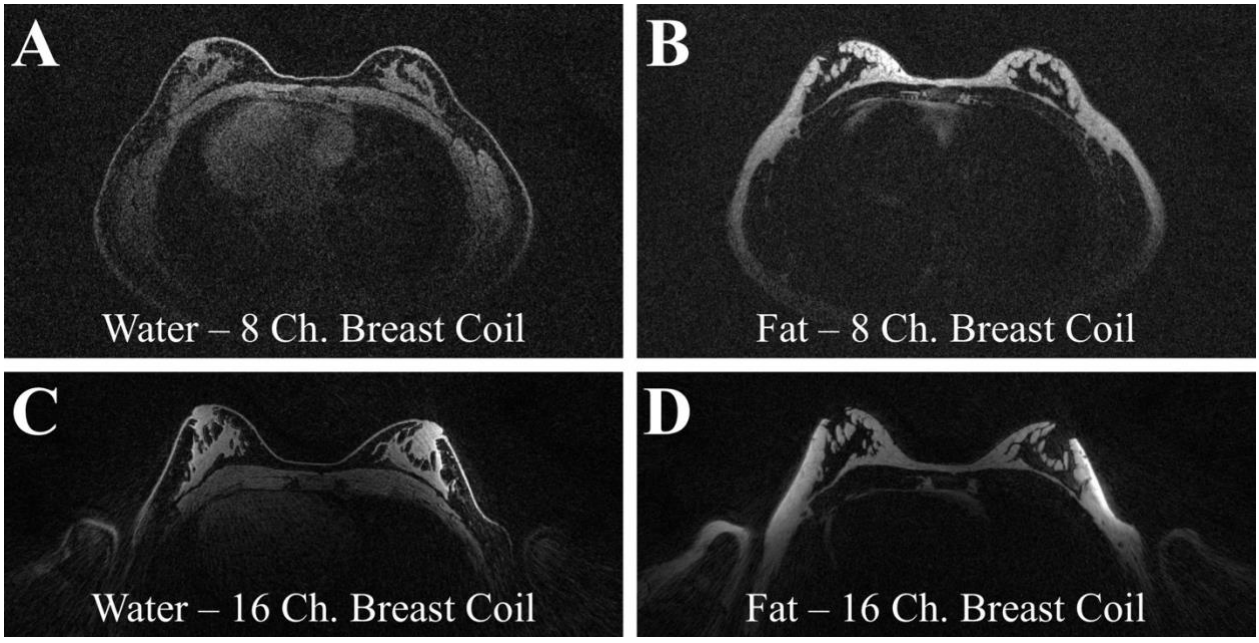

Figure 1.15 *Visualization of two data aquisitions with different breast coil arrays.* ***Top:*** *a Breast MR image acquired using a 8-channel breast coil. Water and fat images are displayed (A-B).* ***Bottom:*** *Similar experiment was performed on a 16-channel breast coil. Water and fat images (C-D) show less coverage compared to the 8-channel array due to the smaller elements. However, there is noticeable increment in signal contrast. The smaller coverage from the 16-channel coil increases sparsity by not being sensitive to the most posterior areas of the breast, which is beneficial for CS algoritms.*

Second, CS reconstructions are able to minimize the noise or undersampling artifacts while increasing SNR (Fig. 1.16). The signal smoothing from CS improves the performance of the B0 field map estimation since there is less noise in which the region growing algorithm could potentially fail by misregistering some pixels that ultimately could result in fat/water swaps. Similar to higher-element coil arrays, the use of CS with IDEAL can be utilized in various ways to speed up imaging, increase spatial resolution, increase SNR or achieve challenging TEs selections.

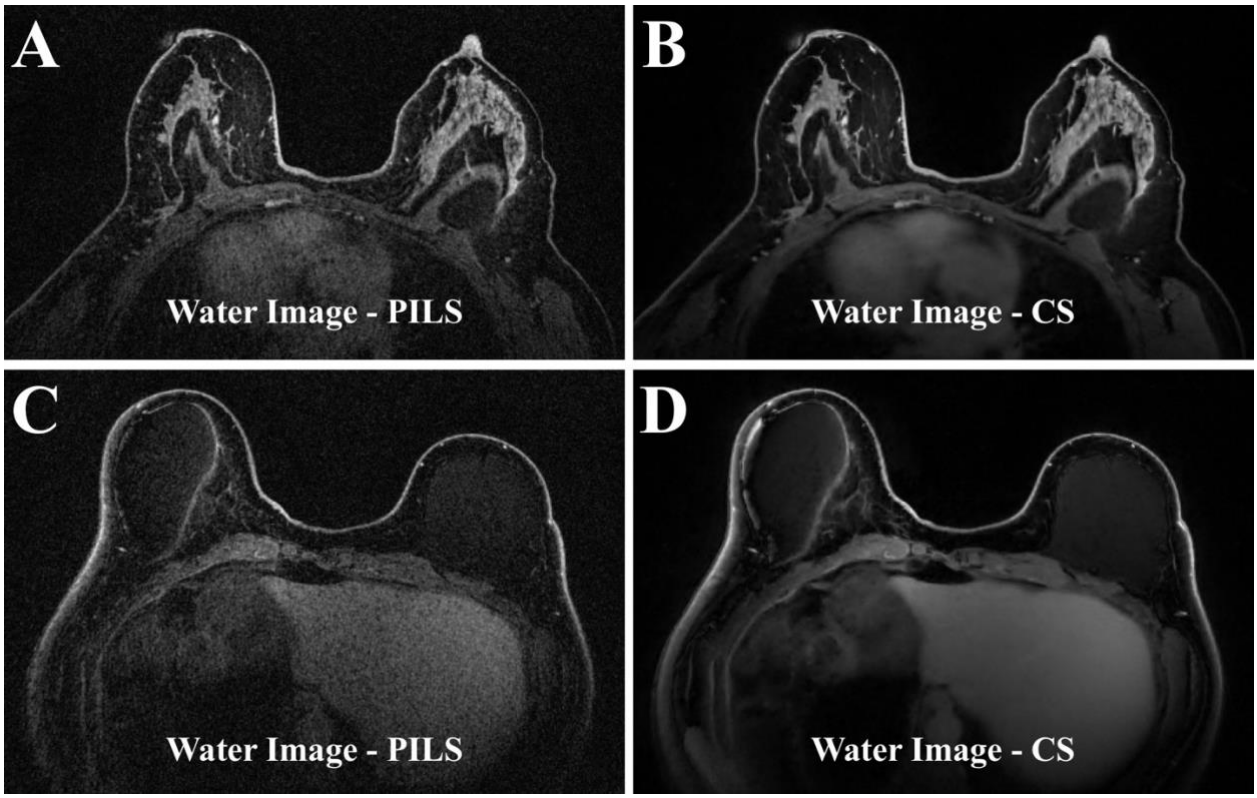

Figure 1.16 *Reconstruction comparsion between parallel imaging (A,C) and compressed sensing (B,D). Two single slices water images from the same volunteer with implants are shown. CS allows for improved image quality by reducing the noise while allowing for resolution of small features within the breast. Despite breast augmentation implants, IDEAL fat/water separation is able to suppress the fat in the the water channel without fat/water "swaps".*

Chapter II DEVELOPMENT

2 FEASIBILITY OF HIGH SPATIOTEMPORAL RESOLUTION FOR AN ABBREVIATED 3D RADIAL BREAST MRI PROTOCOL

This work has been previously published in Resonance in Medicine (MRM). Additional details can be found at: Jimenez, et al. *Magn. Reson. Med*. 2018 Feb 14. PMID: 29446125 DOI: 10.1002/mrm.27137

2.1 Abstract

Purpose: To develop a volumetric imaging technique with 0.8-mm isotropic resolution and 10 s/volume rate to detect and analyze breast lesions in a bilateral, dynamic, contrast-enhanced MRI (DCE-MRI) exam.

Methods: A local low-rank (LLR) temporal reconstruction approach that also utilizes parallel imaging and spatial compressed sensing (CS) was designed to create rapid volumetric frame rates during a contrast-enhanced breast exam—SVIPR STELLR. The dynamic enhanced data is subtracted in k-space from static mask data to increase sparsity for the LLR approach to maximize temporal resolution. A T1-weighted 3D radial trajectory (VIPR IDEAL) was modified to meet the data acquisition requirements of the STELLR approach. Additionally, the unsubtracted enhanced data is reconstructed using CS and IDEAL to provide high resolution fat/water separation. The feasibility of the approach and the dual reconstruction methodology is demonstrated using a 16-channel breast coil and a 3T MR scanner in 6 patients.

Results: The STELLR temporal performance of subtracted data matched the expected temporal perfusion enhancement pattern in small and large vascular structures. Differential enhancement within heterogeneous lesions is demonstrated with corroboration from a basic reconstruction using a strict 10-sec temporal footprint. Rapid acquisition, reliable fat suppression, and high spatiotemporal resolution are presented despite significant data undersampling.

Conclusion: The STELLR reconstruction approach of 3D radial sampling with mask subtraction provides a high-performance imaging technique for characterizing enhancing structures within the breast. It is capable of maintaining temporal fidelity while visualizing breast lesions with high detail over a large field of view to include both breasts.

2.2 INTRODUCTION

Dynamic contrast enhanced (DCE) MRI is a highly sensitive imaging technique for detecting breast cancer[2,24,25]. However, breast DCE MRI is primarily performed for screening patients at high risk for breast cancer or in patients already diagnosed with breast cancer[26,27]. As a result, relatively few women benefit from this powerful imaging modality. The information obtained from the DCE MRI exam is capable of identifying 14.7 additional cancers per 1,000 exams beyond the 11.4 detected by mammography and ultrasound in patients at high risk for breast cancer[6]. In contrast, large scale efforts to supplement mammography with ultrasound screening has netted only an additional 4.2 cancers per 1,000 exams[28]. Clearly, there is a tremendous opportunity to improve breast cancer screening with MRI, but a significant cost differential contributes to directing screening methods towards ultrasound and other less sensitive technologies. Reducing the length and increasing the simplicity of MRI would provide a path to reduce the cost of breast MRI, thus improving patient access to this powerful imaging tool for the detection of breast cancer.

Current clinical strategies to evaluate lesion perfusion with MRI require long scanning sessions. These clinical strategies rely on two methods. The first approach attempts to qualitatively evaluate the change in MRI signal due to the wash-in and wash-out of a contrast agent over a long post-contrast acquisition phase (5-9 minutes or longer), and to use the shape of the signal intensity time curve to improve specificity for breast cancer[16]. This approach has high sensitivity and thus has been widely used in clinical practice since the technical demands are limited and it can be achieved in routine practice. The second primary approach is pharmacokinetic (Pk) modeling of gadolinium contrast dynamics, which is technically demanding in the breast imaging environment and subject to multiple sources of bias and variance even when using the exact same raw input data[17]. Although some studies of Pk modeling have been promising for the quantitative evaluation of tumor response, biology assessment and prediction of

prognosis and survival, it has not been widely adopted in clinical practice, and is unlikely to add further contributions in the breast cancer screening setting where a high negative rate is expected.

An abbreviated MR breast protocol that focuses on the initial enhancement phase holds promise for reducing the duration of screening breast MR exams[29]. For instance, a prospective observational reader study of 443 women-maintained sensitivity to cancer detection by subtraction of a single pre-enhancement volume from a post-enhancement volume, showing the potential to reduce acquisition time from 17 to 3 minutes with less than a minute average reading time by a radiologist[7]. Additionally, promising work has been presented showing the value of determining whether a lesion enhances faster than the rest of the fibroglandular tissue and the lesion's early contrast uptake rate[30]. Moreover, another study that visualized breast perfusion used seven second frame rates to demonstrate the value of higher temporal resolution during initial enhancement phase by obtaining statistically significant differences between benign and malignant lesions[8,9]. However, the high temporal performance in this study required a substantial reduction of spatial resolution. Both of these studies suggest that "loss" of the delayed dynamic contrast enhancement pattern through abbreviating the full protocol could potentially be balanced by detailed evaluation of the initial enhancement phase. However, the studies suggest two quite varying approaches: the former suggests a very low temporal resolution (90 sec) with modest spatial resolution while the latter suggests a very high temporal resolution (7 sec) with very poor spatial resolution.

Breast DCE MRI would ideally provide high temporal resolution to depict lesion enhancement over time while maintaining high spatial resolution to characterize anatomic detail[31]. Numerous approaches have been proposed to provide the high temporal and spatial resolution, in combination with high spatial resolution over the large field-of-view (FOV) required for breast imaging. Unfortunately, most available techniques are able to only partially improve temporal resolution at the cost of spatial resolution, which is unacceptable to radiologists given the clinical importance of high spatial resolution

to characterize lesion morphology. Thus, most clinical MRI exams have prioritized spatial resolution over temporal resolution, as morphologic features have been shown to have greater specificity for breast cancer[32-34]. Clinical breast DCE MR exams have temporal resolutions on the order of 60-180 seconds[14,15]. Currently, most successful MRI efforts have increased temporal resolution using nonconventional acquisition trajectories that range from Cartesian pseudorandom k-space sampling to non-Cartesian trajectories such as spirals[35] and radial stack of stars[36]. Many proposed techniques use a spatially invariant, view-sharing methodology (i.e., TRICKS[37], TWIST[38], KWIC[39], DISCO[40]) for reconstruction with a linear interpolation of adjacent frames to represent the temporal behavior of enhancing structures. However, aggressive view sharing leads to artifacts that misrepresent enhancement of small or heterogeneous features and thus the achievable acceleration while accurately modeling the temporal behavior is modest[41].

More recently, parallel imaging in combination with non-linear regularization methods has been utilized to provide higher temporal and spatial performance. The radial XD-GRASP[42] method has recently been extended to provide frame rates of less than 7 seconds during free breathing, but examples of enhancing breast lesions were provided at 40 seconds intervals or greater with spatial resolution at or over 1 mm[43]. Often compressed sensing (CS) studies in the breast have demonstrated acceleration by taking a fully sampled data set, artificially removing a fraction of the data, and showing that a similar imaging output was obtained[44-49]. Unfortunately, these methods can be affected by significant partial voluming, thus eliminating the capability to visualize key features of differential enhancement in other planes.

We hypothesize that constrained, iterative reconstruction methodologies could provide a platform for simultaneously providing high spatial and temporal information of the early enhancement phase. Such a capability would allow breast researchers to extract all the diagnostic and lesion characterization data possible out of the early enhancement phase when larger trials of abbreviated breast

DCE-MRI screening are likely to be carried out. Such trials could also answer whether the proposed abbreviated protocol is able to maintain or improve specificity. Thus, the purpose of this work was to develop and demonstrate the feasibility of a bilateral DCE breast MRI technique that provides at least two strategic components. Primarily, a dynamic reconstruction with 10s volumetric temporal resolution for evaluation of early tumor perfusion over the first 180 seconds while maintaining sub-millimeter isotropic spatial resolution for lesion morphologic assessment. We exploit the sparsity provided by a 3D radial mask-subtracted set (SVIPR) through a **S**patial CS with **Te**mporal **L**ocal **L**ow-**R**ank assistances (STELLR) reconstruction. The local low-rank (LLR) component of the approach allows the algorithm to alter the temporal behavior in a spatially variant pattern, effectively allowing the temporal footprint to narrow in heterogeneous areas and widen in more static regions. Secondly, the method provides a static reconstruction with fat-water separation (VIPR CS+IDEAL) to show the contrast-enhanced breast architecture. Both reconstructions require a total of six minutes of acquisition time, significantly less than the standard clinical imaging time. To the best of our knowledge, this is the first implementation of a locally spatial variant temporal constraint in a bilateral DCE breast exam. The results provide a framework for detailed analysis of the information content that can be derived during an abbreviated breast exam.

2.3 METHODS

There are three key elements that describe the dynamic component of the abbreviated breast protocol—SVIPR STELLR: 1) A high-performance 3D radial sampling acquisition pattern that meets the requirement for CS, 2) an LLR constraint to exploit temporal data redundancy, and 3) a method that concentrates ONLY on the early phase enhancement. The versatility of our acquisition trajectory allows for a static reconstruction to provide multi-peak four-point fat/water separation within the same data set used to produce the dynamic reconstruction. Thus, the advancement in our proposed methodology relies on integrating an acquisition strategy and two reconstruction approaches whose capabilities complement each other.

2.3.1 Data Acquisition

The modified 3D radial sampling Vastly undersampled Isotropic Projection (VIPR)[50] trajectory is based on a previously published 3D radial dual half-echo trajectory (VIPR IDEAL)[51] in T2-weighted volumetric imaging. This trajectory is well suited for constrained reconstruction algorithms because it combines variable density sampling and pseudorandom undersampling of the periphery of k-space in all directions, extending upon the 2D radial benefits obtained through "stack of stars" approaches. Thus, the aliasing artifact due to undersampling is not constructive or structured but rather incoherent[52]. Moreover, radial trajectories start sampling right after excitation, which makes the technique rapid and efficient. Consequently, the sampling pattern is very appropriate for a dynamic reconstruction.

Data are collected with a T1-W spoiled gradient echo sequence with a bipolar 3D radial trajectory[53]. A spiral-based algorithm is used to distribute at equidistance all radial spokes for the four unique echoes through the surface of the sample sphere in k-space (Fig. 2.1A). Four interleaved echo times distributed into two TRs, as shown in Fig. 2.1B, are acquired with echo times suitable for fat/water decomposition with an Iterative Decomposition with Echo Asymmetry and Least squares estimation (IDEAL)[22]. A bit-reversal permutation of a sequential sampling of the exterior of the sphere was added to pseudo-randomize the order of each group of four unique spokes for a dynamic, sub-sampled

reconstruction. The set of all radial spokes is considered a composite sample set or pass (Fig. 2.1C). The radial sampling pattern allows for a unique set of radial lines to be acquired in each echo (as opposed to the same lines acquired in Cartesian sampling), which, when combined with the efficient out and back trajectory and radial undersampling, leads to a 2x improvement in sampling efficiency[23]. In this work, we used two identical sample sets to demonstrate the technique. The first sample set or pass before the contrast injection is used as a mask and the second pass starts as the contrast agent is administered.

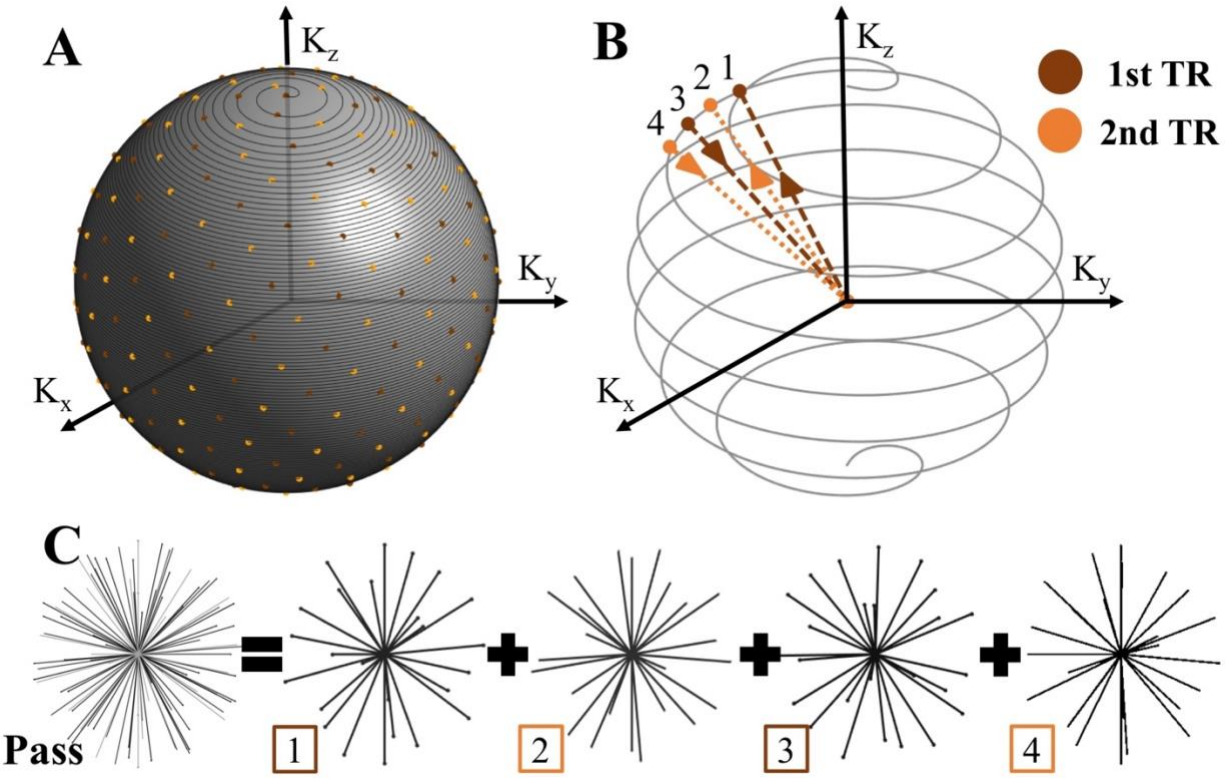

Figure 2.1 *T1-weighted VIPR IDEAL sampling pattern. A) Equidistant distribution of radial spokes in k-space. B) Order of sampling echoes within the two TRs. C) A full composite set or pass of radial spokes formed by four unique echo data sets.*

The VIPR IDEAL acquisition allows us to achieve comparable TEs for a theoretical optimal combination of echoes for a three-point method ($-\pi/6$, $\pi/2$, $7\pi/6$)[54] plus an additional echo to increase the effective number of signal averages (NSA). Our IDEAL implementation uses six resonant peaks to model fat and accounts for the additional phase accumulated by off-resonant spins at each point in the k-space acquisition trajectory[55]. Due to the short interval over which data are acquired (TEs: 0.18, 1.032,

1.624, 2.32 ms), the longest TE is expected to have a minimal reduction in contrast-enhanced signal intensity due to the signal decay[56]. Moreover, it is unlikely that enough concentration of gadolinium will accumulate in the breast over the first three minutes of post-contrast to generate T2* shortening effects[57]. Therefore, no R2* correction was calculated in favor of maximizing SNR. Cramér-Rao bounds[58] were used to identify optimal TEs that produced the highest estimated number of signals averaged (NSA) for our four-point method, while maintaining a relatively small TR of 4.3 ms.

2.3.2 Dynamic Reconstruction

Low rank has been successfully used in various non-breast MRI applications by assuming that all temporal behaviors in the image volume can be represented by a limited number of temporal basis functions[59-61]. The idea of breaking up the kernel into considerably smaller local blocks rather than one global block promotes higher data redundancy, which significantly reduces the rank of the vector space of temporal signals needed to represent the local temporal behavior[62-65]. Algorithms enforcing local low rank benefit from the additional sparsity added by k-space subtraction. A local temporal constraint is imposed by subdividing time-gated volumes into small blocks. Subsequently, all pixels within a block across all time-gated volumes are reorganized into a Casorati matrix with all the pixels as columns and their temporal behavior as rows[66]. Singular value decomposition (SVD) is performed to provide the principal components by which the image information can be represented or decomposed followed by singular value thresholding (SVT). The assumption is that there are a few large eigenvalues in the SVD, allowing for data representation using fewer components with negligible data, i.e. low rank. In other words, SVD provides the reconstruction algorithm the capability of learning a data-specific domain in which the information can be represented with fewer components[67]. The location of this block is moved across until the entire volume is covered with four overlapping patterns. Consequently, this approach allows us to provide high temporal resolution without compromising spatial resolution.

The dynamic reconstruction, or SVIPR STELLR, was designed based on a Projection Over Convex Sets (POCS)-type algorithm to produce a dual constrained reconstruction[19]. The reconstruction is separated into three steps: 1) data consistency, 2) spatial constraint and 3) local temporal constraint (Fig. 2.2C). Such steps are described by the three terms inside the summation of the following optimization problem:

$$\min_{\mathbf{x}} \ \|\mathbf{D}_t\mathbf{F}\mathbf{S}\mathbf{x} - \mathbf{d}_t\|_2 + \boldsymbol{\lambda}_{CS}\|\boldsymbol{\Psi}\mathbf{x}\|_1 + \boldsymbol{\lambda}_{LLR}\sum_{\mathbf{b}=1}^{\mathbf{N_b}}\|\mathbf{C_b}\mathbf{x}\|_* \quad (1)$$

where x is the combined image from all coils from the complete subtracted pass (SVIPR), D_t is a subsample operator at temporal volume t, F is Fourier encoding, S represents the coil sensitivities and d_t is the measured k-space data at temporal volume t. The total number of temporally gated volumes in the DCE acquisition for this study was 18 over 180 seconds. The first part of the equation refers to the data consistency portion of the reconstruction in which the benefits of parallel imaging are exploited through a SENSitivity Encoding (SENSE)[68] signal model. The second term describes the global spatial constraint using the L1-norm ($\|x\|_1$) of spatially wavelet transformed (Ψ) images. Lastly, the third term defines the local temporal constraint part, where C_b refers to an operator that selects image block of size b (4x4x4 pixels for this study) throughout all T temporal volumes. The number of blocks by which the volume is sub-divided is N_b, and $\|x\|_*$ is the nuclear norm of a matrix A[20]. This cost function was minimized iteratively using alternating data consistent gradient descent, iterative soft thresholding (IST), and SVD corresponding to each of the three components. Variables $\boldsymbol{\lambda}_{CS}$ and $\boldsymbol{\lambda}_{LLR}$ are regularization parameters to weigh the relative importance of spatial and temporal constraint respectively. For the SVIPR STELLR reconstruction $\boldsymbol{\lambda}_{CS}$ was empirically set to 0.01 and $\boldsymbol{\lambda}_{LLR}$ to 0.05.

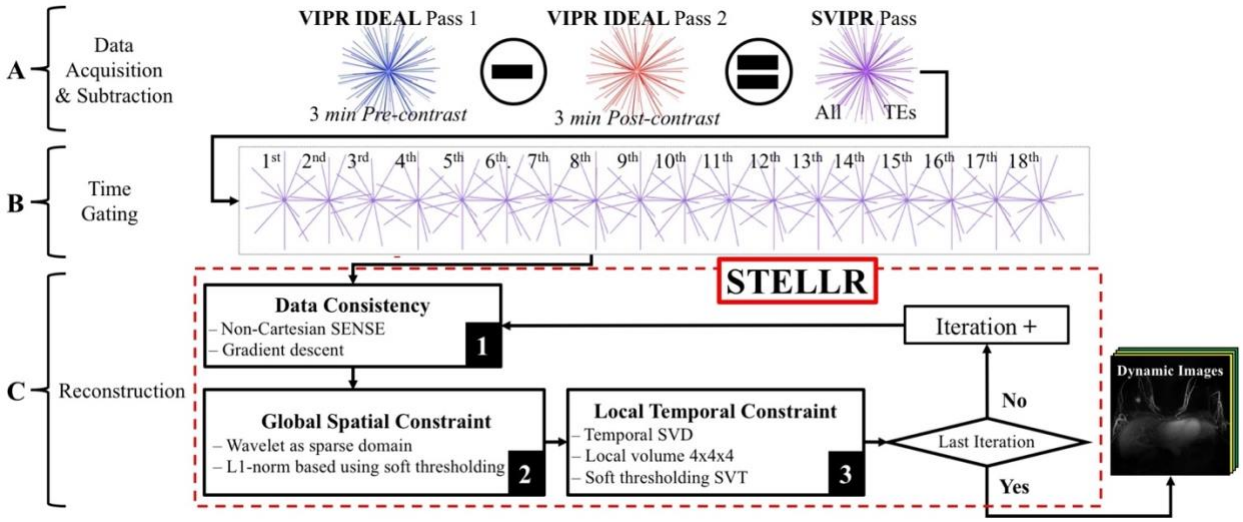

Figure 2.2 *Dynamic reconstruction flow digram showing A) data acquisition of VIPR IDEAL trajectory, mask subtraction in k-space and echo combination to create a subtracted VIPR pass (SVIPR), B) time gating as a preprocessing step and C) STELLR reconstruction algorithm containing three steps: 1) data consistency, 2) global spatial thresholding and 3) local temporal thresholding.*

A graphical representation of the algorithm is shown in Figure 2.2. The dynamic reconstruction quadruples the data sampling performance of VIPR IDEAL by adding all the echoes in a single data set and increasing sparsity within the image by subtracting the pre-contrast pass from the post-contrast pass (Fig. 2.2A). The new subtracted VIPR set (SVIPR) is rearranged into sets of 10 second temporal windows. As a result, 18 unique volumes are obtained with dynamic information (Fig. 2.2B). These volumes are then fed into a STELLR algorithm as described by Figure 2C. First, these volumes alternate between radial and Cartesians grids every iteration as a pre- and post-step for a non-Cartesian SENSE algorithm. Gradient descent (GD) is used for optimization by finding the minimum difference between the acquired data and the constrained solution in the SENSE model. Second, a L1-norm minimization of a wavelet transform, in the spatial domain, is used to regularize the data as part of CS. Third, a small local varying window for thresholding is applied—LLR. These three consecutive steps are performed for a total of 30 iterations.

2.3.3 Static Reconstruction

The optimization problem and signal model for the static reconstruction or VIPR CS+IDEAL[69] lacks the temporal constraint of the dynamic model. Therefore, our approach becomes a more traditional CS algorithm. The mathematical expression for this optimization problem can be expressed as:

$$\min_{\mathbf{x}} \quad \|\mathbf{D}_e\mathbf{F}\mathbf{S}\mathbf{x} - \mathbf{d}_e\|_2 + \lambda\|\Psi\mathbf{x}\|_1 \tag{2}$$

the first term or data consistency portion is similar to equation 1, where x is the all coil combined image from a complete pass (VIPR), D_e is a subsample operator pertaining to echo e, F is a Fourier encoding matrix corresponding to the k-space sampling trajectory, S represents the coil sensitivities and d_e is the measured k-space data from echo e. Similarly, a wavelet transform is utilized as a sparsifying transform Ψ in the second term to enforce a global spatial constraint. IST is also used to solve for the L1-norm of the system defined as $\|x\|_1$. The reconstruction regularization parameter $\boldsymbol{\lambda}$ was empirically set to threshold 10% of the coefficients per iteration.

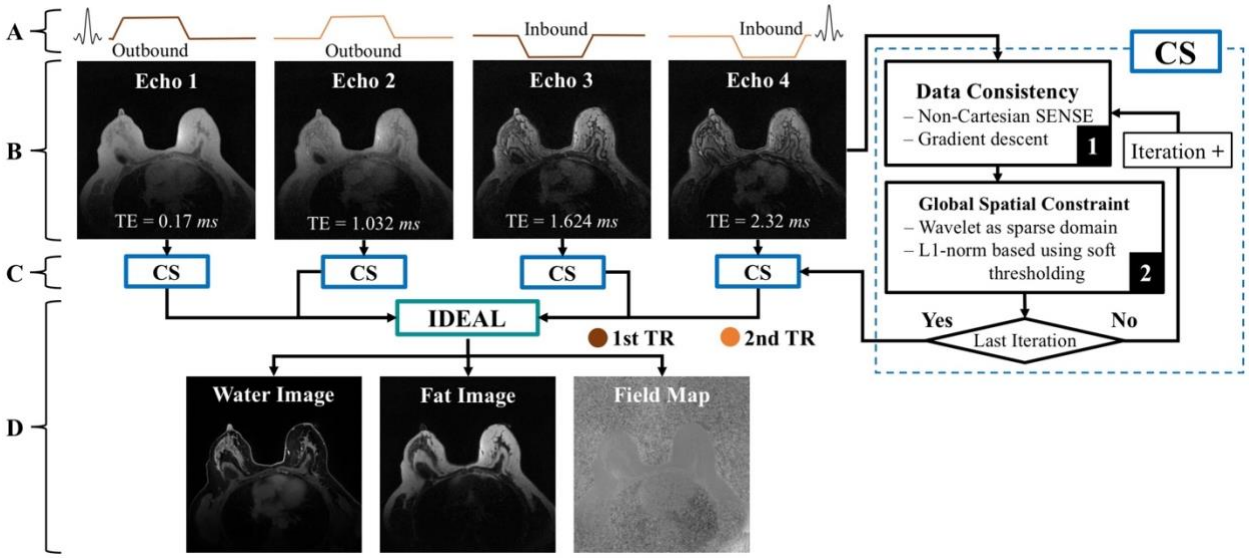

Figure 2.3 *Static reconstruction diagram demonstrating: A) the collection of four half echoes by the alternating TRs, B) two half echoes are acquired in two readouts offset by a 0.85 ms delay to produce four gradient echoes that sample four unique radial lines. C) Each echo is separately processed with a compressed sensing approach followed by D) a modified IDEAL algorithm.*

The static reconstruction uses all the data from the second pass without temporal gating (Fig. 2.3A-B). The reconstruction processes each unique k-space volume collected at each echo time

separately using a CS algorithm (Fig. 2.3C). The static reconstruction also takes advantage of parallel imaging during the GD SENSE step[70]. The reconstructed radial echo images are fed into a modified IDEAL fat/water decomposition algorithm to provide the final set of water and fat image volumes (Fig. 2.3D).

2.3.4 Evaluation

Six patient volunteers with a previous clinical breast MRI performed for a standard clinical indication and containing an area of breast enhancement which could be well depicted with time-resolved breast MRI were recruited to participate in this IRB-approved, HIPAA-compliant study. Imaging was performed on a 3T system (Discovery 750, GE Healthcare) with a 16-channel breast coil (Sentinelle, Invivo, Gainsville, FL) using the following three pre-contrast scans: an investigational version of a commercially-available quantitative chemical shift encoded MR sequence with six echoes, referred to as Cartesian IDEAL (IDEAL IQ, GE Healthcare, Milwaukee WI), T1-W FSPGR with two echo times and two-point Dixon reconstruction (VIBRANT FLEX, GE Healthcare) and the 3D radial VIPR IDEAL sequence described above. Table 1 demonstrates the image acquisition parameters for each of the three sequences. The static reconstruction, or VIPR CS+IDEAL, was compared to the two other acquired sequences, Cartesian IDEAL and T1-W FSPGR two-point Dixon, to demonstrate its ability to decompose fat/water.

Table 2	Scan Time	TR	Echoes	Resolution	Voxel Vol.	Matrix Size	FOV
Cartesian IDEAL	4:40 min	7.7 ms	6	1x1x3 mm	3.0 mm^3	320x320x66	32 cm
T1-W FSPGR Two-point Dixon	1:10 min	4.2 ms	2	1x1x1.4 mm	1.4 mm^3	320x320x138	32 cm
VIPR IDEAL	3:00 min	4.3 ms	4	0.8x0.8x0.8 mm	0.5 mm^3	384x384x384	32 cm

Table 2.1 *Scan parameters for volumetric fat/water breast imaging methods prior to contrast administration. The VIPR IDEAL k-space trajectory was repeated as contrast was injected and utilized for the dynamic study though the VIPR IDEAL scan time is 2.5x longer*

For the DCE portion, a second three-minute VIPR IDEAL trajectory pass was initiated concurrently with the start of the intravenous contrast injection. The proposed dynamic, mask-subtracted reconstruction was compared to a mask-subtracted, CS reconstruction with a strict, 10s temporal

footprint. Comparison of the two reconstructions allowed assessment of the value of the STELLR approach in improving SNR against a method with strict temporal fidelity. Though the 10s-strict temporal fidelity is inherently low in SNR, it provides an easy method to assess the actual ordering of dynamic enhancement within the lesion and elsewhere in the breast. Additionally, our method was compared to a more conventional method using Parallel Imaging reconstruction (PILS)[71] and view sharing through a tornado filter that expands its temporal footprint from 30s at the k-space center to 90s at the k-space edge (Tornado+PILS)[53]. Furthermore, a static reconstruction of all combined post-contrast echoes with mask subtraction of the pre-contrast pass (SVIPR CS) was performed to produce a post-contrast volume similar to those provided in conventional DCE-MRI studies today. Quantitative image comparison between methods was performed using structural similarity index (SSIM)[72].

Image reconstruction was performed using an AMD-Opteron CPU computer node with 32-cores and 120 GB RAM. Reconstruction time for the dynamic SVIPR STELLR reconstruction dataset (16 channels, 384 slices, 18 frames, 2333 spokes) was 22:48 hrs. The static VIPR IDEAL+CS reconstruction time (16 channels, 384 slices, 4 echoes, 10500 spokes) was 8:52 hrs. The static SVIPR CS reconstruction time (16 channels, 384 slices, 42000 spokes) was 2:32 hrs.

2.4 RESULTS

2.4.1 Dynamic Reconstruction

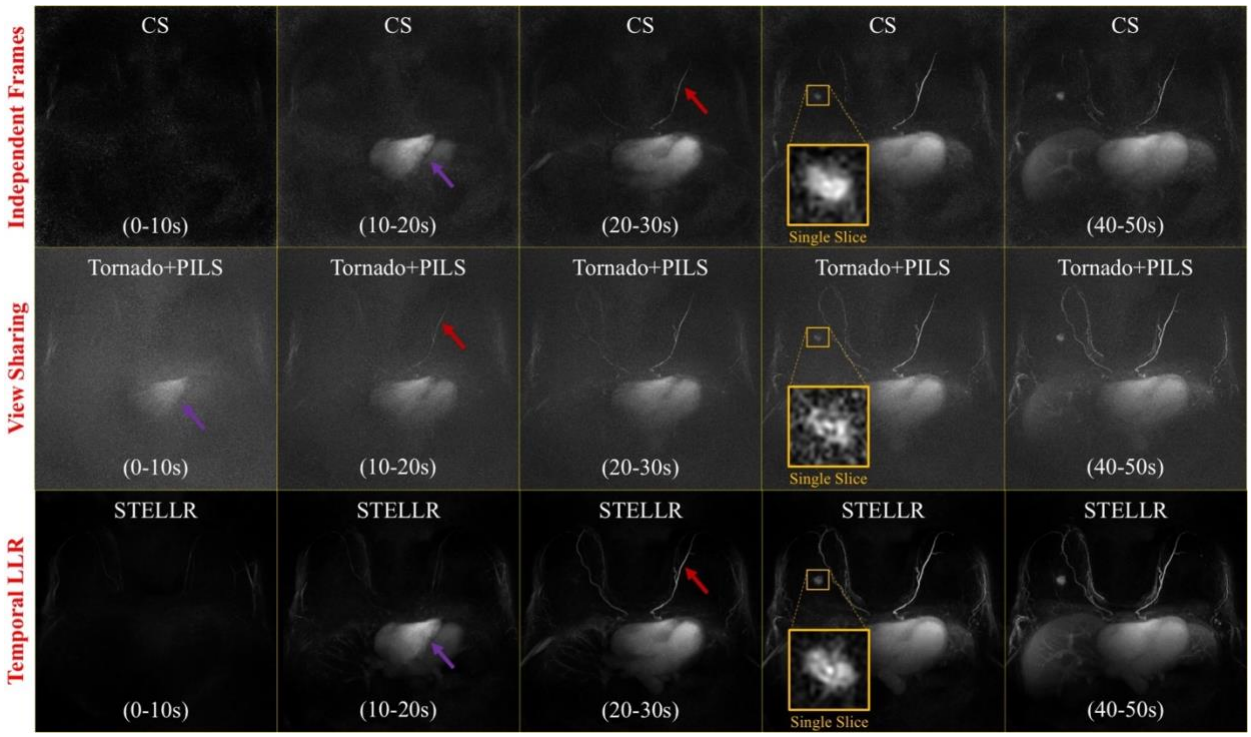

Figure 2.4 *An SVIPR data set reconstructed using three different methods, CS with strict 10s temporal footprint (top), Tornado+PILS reconstruction (middle), and the proposed dynamic reconstruction using STELLR (bottom). Targeted MIPs of each 10s-volumetric frames frames are shown for the first 5 frames. The heart is indicated in the first frame in which it is visibly enhanced by a purple arrow while the mammary artery is indicated in the first frame using a red arrow. The tornado filter, with its 30 second base footprint, incorrectly shows the heart enhancing and left mammary artery enhancing in the first and second 10s time frames respectively due to its larger temporal footprint. STELLR is able to provide consistent perfusion with CS and more lesion detail. Magnification of the lesion over a single slice (30-40s) is shown for each method (yellow box) and demonstrates the improved spatial resolution with the STELLR approach.*

Dynamic Reconstruction: For the evaluation of the dynamic, mask-subtracted study of contrast passage (SVIPR STELLR), maximum intensity projections (MIP)s of each 10s-volumetric frame were generated for each method (Fig. 2.4). The strict 10 s temporal footprint of CS provides a reference to visualize perfusion within the breast. STELLR's ability to effectively deliver high temporal bandwidth is shown by its ability to capture the enhancement of both large (heart) and small (mammary arteries) structures in the proper time frame as compared to the CS reconstruction (Fig. 2.4). Due to its wide temporal footprint, the Tornado+PILS reconstruction shows premature visualization of the mammary

arteries and heart (Fig. 2.4). Furthermore, STELLR provides higher contrast between the mammary arteries and background. Single slice visualization of the lesion demonstrates the ability of the high spatial resolution (0.8 mm isotropic) provided by the dynamic reconstruction to visualize fine features as compared to the Tornado+PILS and CS reconstruction despite 45x data undersampling. STELLR was able to capture the lesion morphologic features, including spiculated margins and an irregular shape while matching perfusion visualization with the 10s-strict footprint. These qualitative findings are corroborated by the SSIM values in Figures 2.5-6.

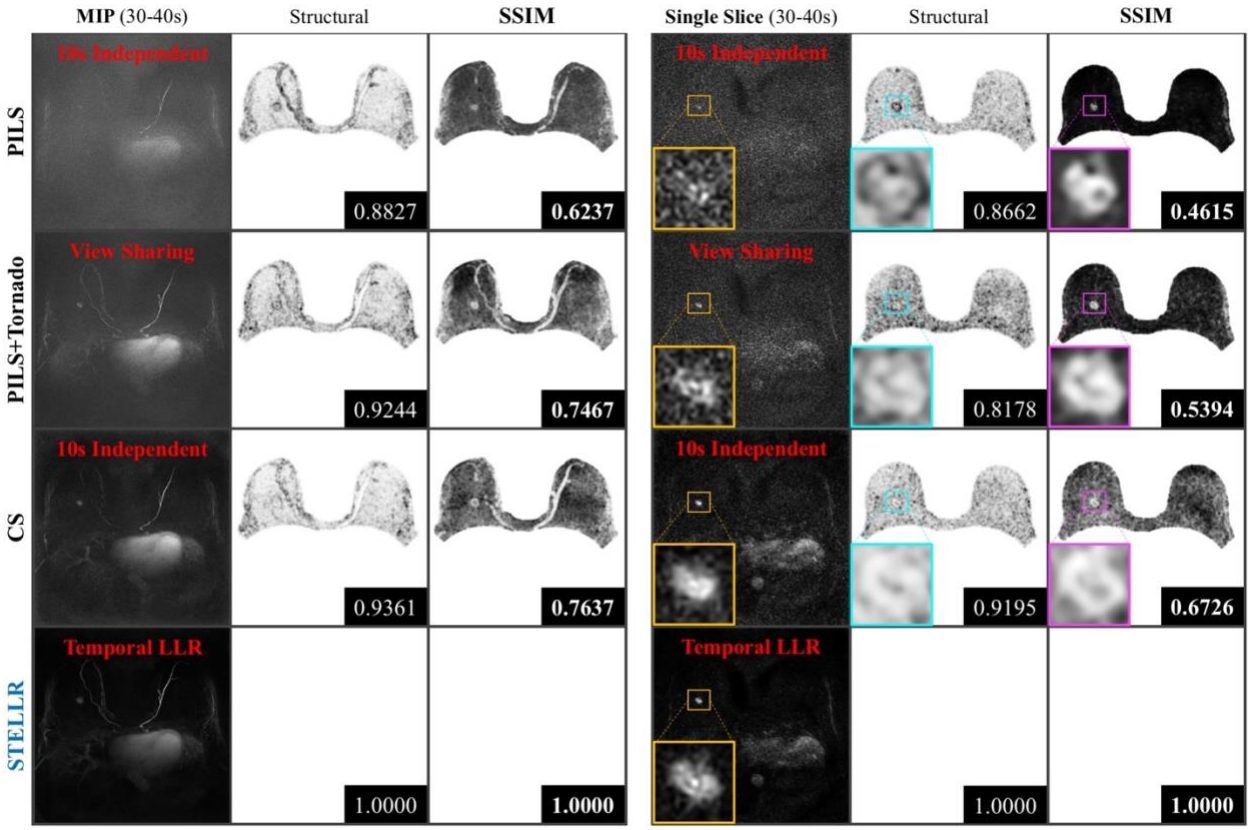

Figure 2.5 *SSIM analysis of a single time interval (30-40s) over only the breast tissue provides a measure of similarity between four methods and STELLR reconstruction. Columns 1 and 4 show MIPs and single slice renderings of each reconstruction respectively. Columns 2 and 5 contain SSIM maps of the structural coefficient and its decomposed SSIM index number. Columns 3 and 5 provide a complete SSIM measurement of all three components (luminance, contrast and structure) and its combined maps. The highest SSIM similarity scores were obtained when comparing STELLR against CS which is the reference method for temporal resolution. Both methods scored even higher when computing only the structural index.*

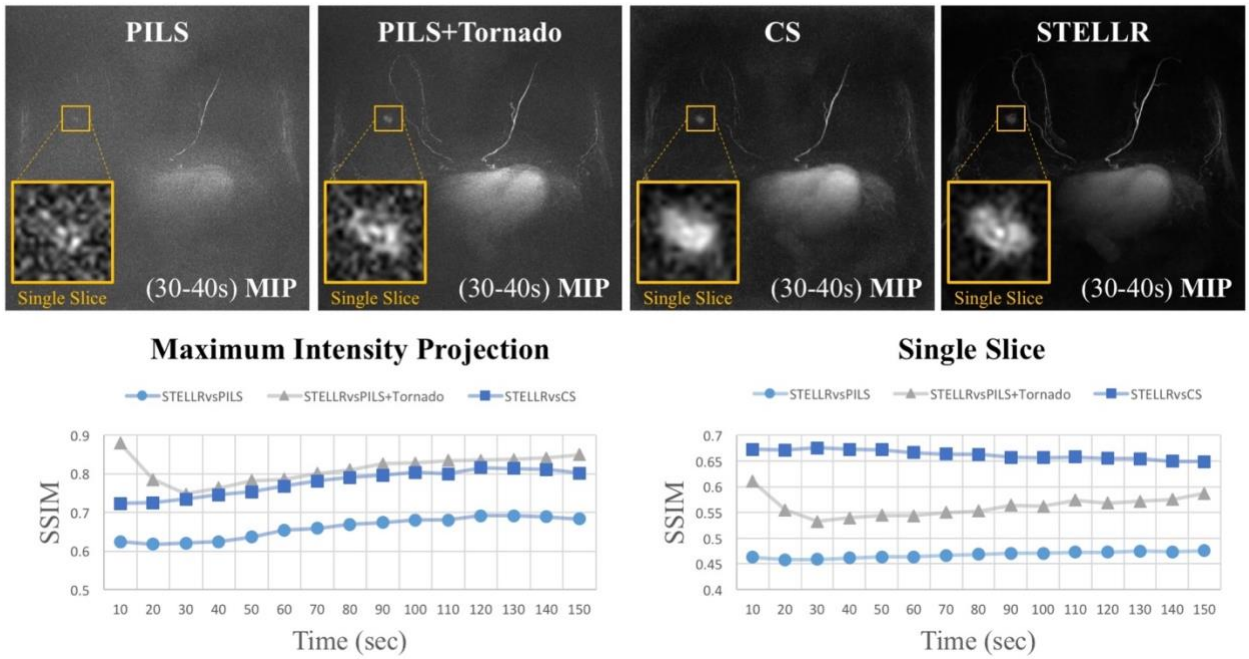

Figure 2.6 Top: *visual comparison of 4 methods over a single time interval (30-40s).* ***Bottom:*** *SSIM index plot of each method using STELLR as reference over the first 15 time points. Consistent SSIM similarity scores can be seen over time at the MIP and single slice level. Qualitative observations match quantitative measurements. CS obtains the highest similarity measure while PILS the lowest. PILS+Tornado performance fluctuates at the beginning due to the temporal filter but stabilizes as it moves forward. SSIM indexes of MIP measurements obtained higher similarity overall than single slice since MIPs are less affected by pseudo-noise caused by undersampling.*

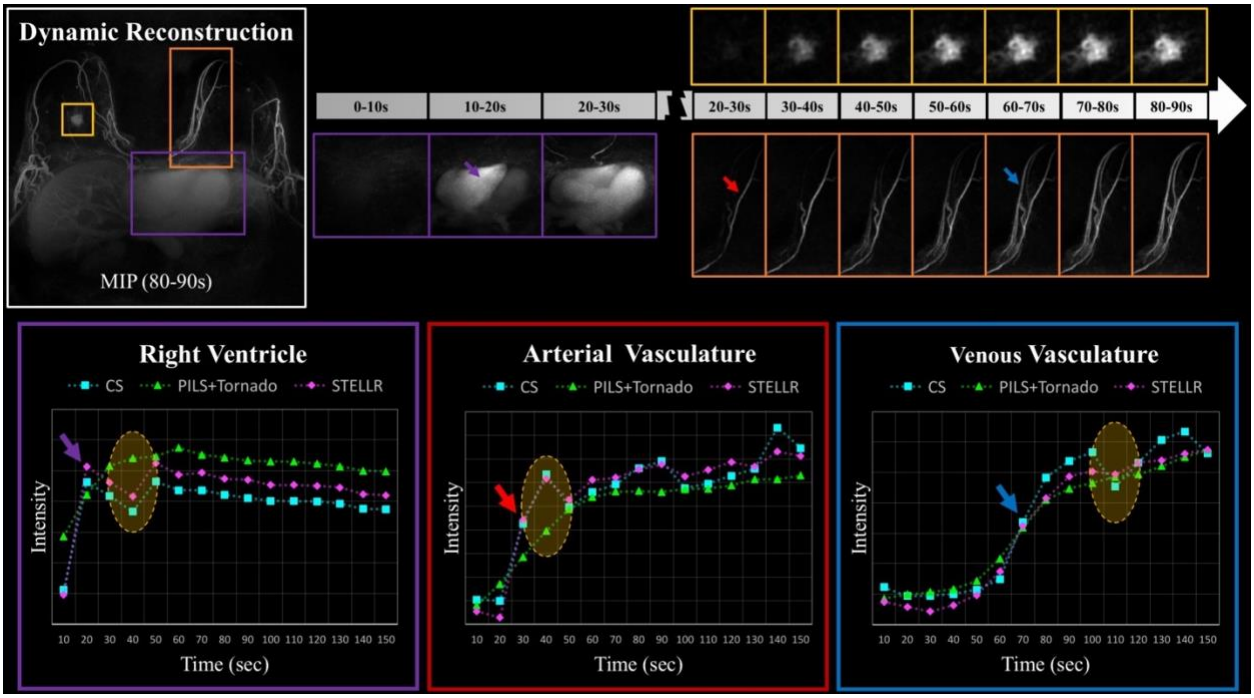

Figure 2.7 Top: *Demonstration of the dynamic image reconstruction capabilities using the SVIPR STELLR method evaluated over three regions, demarcated on the left (purple heart chambers, orange mammary artery and vein, and yellow lesion). Middle MIP over the purple ROI shows ability to rapidly*

capture chamber filling with 10 s frame rate. MIP over the orange ROI displays rapid transit of arterial (red arrow) blood in mammary artery to nearby venous vasculature (blue arrow). The yellow ROI shows temporal enhancement of complex lesion. ***Bottom:*** *signal intensity measurements from three ROIs: right ventricle (purple), artery (red) and vein (blue). In all three signal intensity measurements, STELLR (magenta) has a similar profile to CS (cyan), which is the only reconstruction with strict 10s temporal resolution. On the other hand, PILS+Tornado has the smallest intensity range and low dynamic variation whereas STELLR and CS show a richer change in signal (yellow ellipse).*

Visualization of the expected physiology is demonstrated by the proposed dynamic reconstruction of the SVIPR set through inspection of axial sequential frames generated at 10 s intervals (Fig. 2.7). The MIPs demonstrate temporal fidelity throughout the volume in the three regions of interest (ROIs). Heart perfusion matches expected physiology (purple box, Fig. 2.7), with the right ventricle enhancing after 10 s of contrast administration. Lesion temporal heterogeneity is captured while preserving morphologic features (yellow box, Fig. 2.7). Expected temporal enhancement of the breast arterial-venous vasculature is shown (orange box, Fig. 2.7) despite significant data undersampling and small diameter of the vessels. The temporal performance of SVIPR STELLR with a 10s-volumetric frame rate demonstrated proper visualization of expected physiology, with expected sequential filling of the right ventricle, left ventricle, mammary arteries and mammary veins. Signal intensity measurements support SVIPR STELLR temporal fidelity when compared against CS.

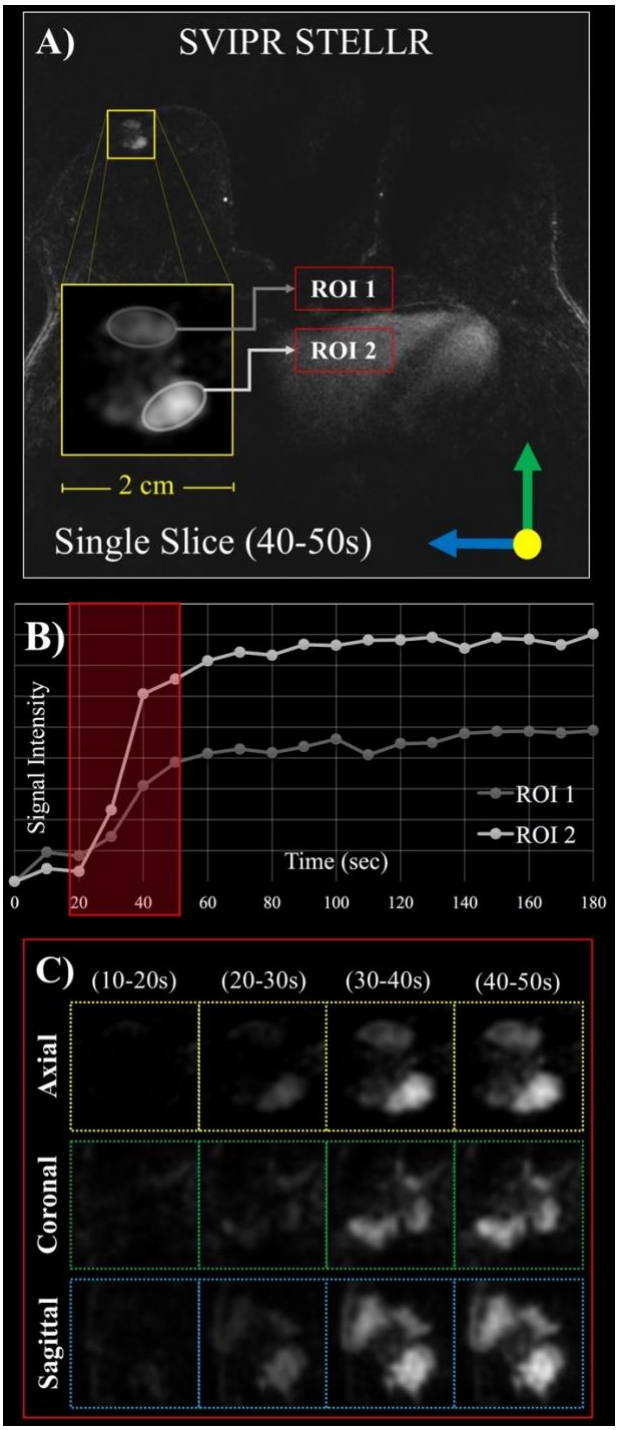

Figure 2.8 *SVIPR STELLR reconstruction of a volunteer patient with a 1.6-cm diameter malignant tumor. A) Axial single slice of the subject 50 seconds after contrast injection shows 2 areas of contrast enhancement (actual in small yellow box and magnified in larger yellow box). B) Signal intensity average for two regions of interest within the tumor during the first 180 seconds of perfusion at 10 sec intervals shows more rapid enhancement in the more posterior aspect of the tumor (ROI 2). C) Single*

slice (0.8 mm) visualization of the entire tumor enhancement pattern through four sequential 10 s frames in three orthogonal axes shows complex spatial and temporal behavior.

Figure 2.8 demonstrates the capabilities of the proposed dynamic reconstruction. In figure 2.8A, a single slice from a volumetric frame is offered as a point of reference. Two ROIs from within the lesion are chosen to measure signal intensities as a function of time. In Figure 2.8B, comparison of the enhancement curves of the anterior portion (ROI 1) and posterior portion (ROI 2) of the lesion at 10 second intervals demonstrates that the posterior portion enhances more rapidly and more intensely. In Figure 2.8C, the irregular shape and varied onset of contrast enhancement within the tumor can be appreciated using three orthogonal planes.

2.4.2 Static Reconstruction

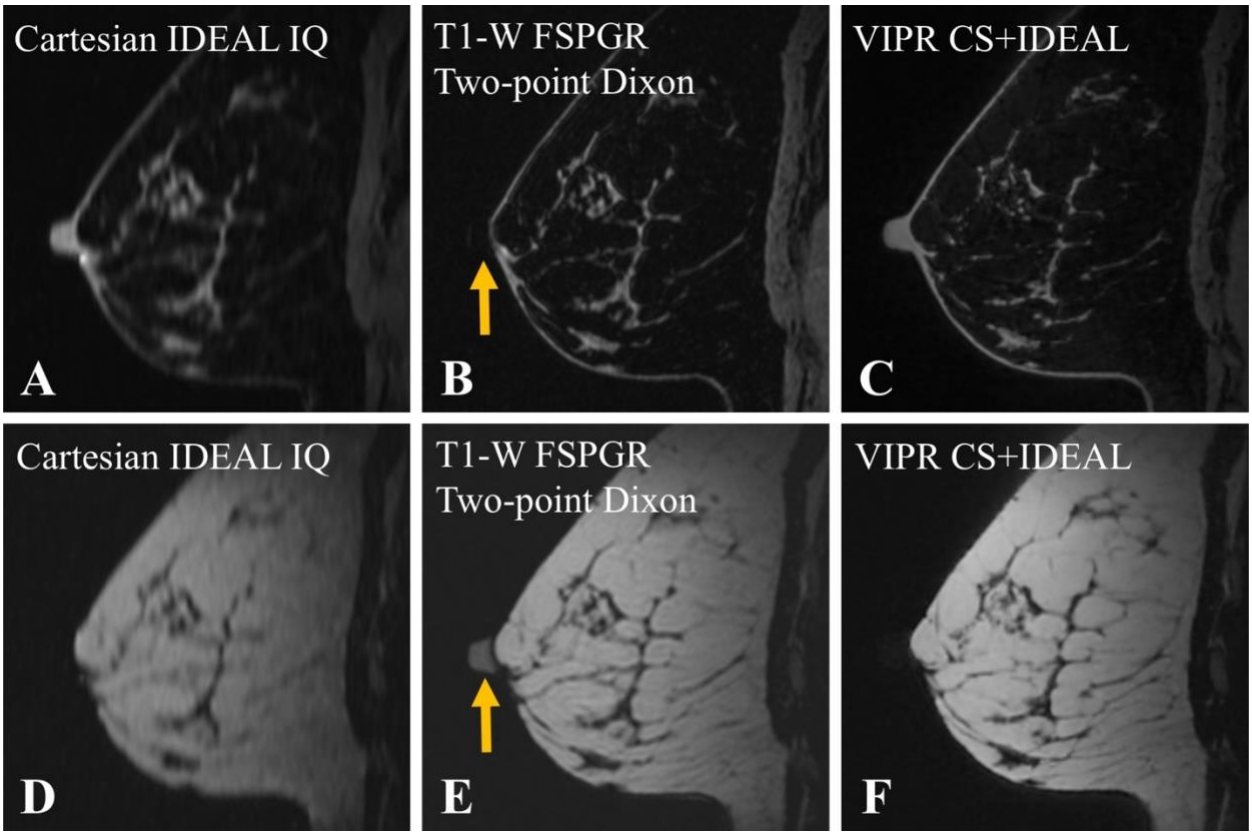

Figure 2.9 *Reformatted sagittal views of three fat/water decomposition methods sampled before contrast injection was applied with water volumes shown on top and fat on the bottom. Cartesian IDEAL (A and D) has limited resolution. The two-point approach in T1-W FSPGR (B and E) fails to keep the nipple in*

the water channel (yellow arrows). VIPR CS+IDEAL (C and F) maintains high resolution while robustly decoupling fat and water.

Static Reconstruction of pass 1: In the fat/water decomposition, all three sequences (Table 1.1) prescribed in the axial plane were reformatted into sagittal views. Cartesian IDEAL provides reliable fat/water separation but redundant acquisition of the same k-space lines at all three echo times, forcing the slice thickness to be three times the in-plane resolution. Consequently, image blurring is clearly visible in the sagittal reformat (Fig 2.9D). For the two-point Dixon T1-w FSPGR method, the two echo times and reconstruction kernel size fail to assign the nipple to the water channel (Fig. 2.9B) and instead placed it in the fat channel (Fig. 2.9E). In comparison, VIPR CS+IDEAL correctly decomposed water in the nipple, demonstrating its ability to provide the needed inputs for a robust multi-peak fat model while estimating and correcting for B0 inhomogeneities in a challenging location. Furthermore, the 0.8-mm isotropic resolution better depicts fibroglandular detail when reconstructed into orthogonal planes, as shown when comparing Fig. 2.9D-F.

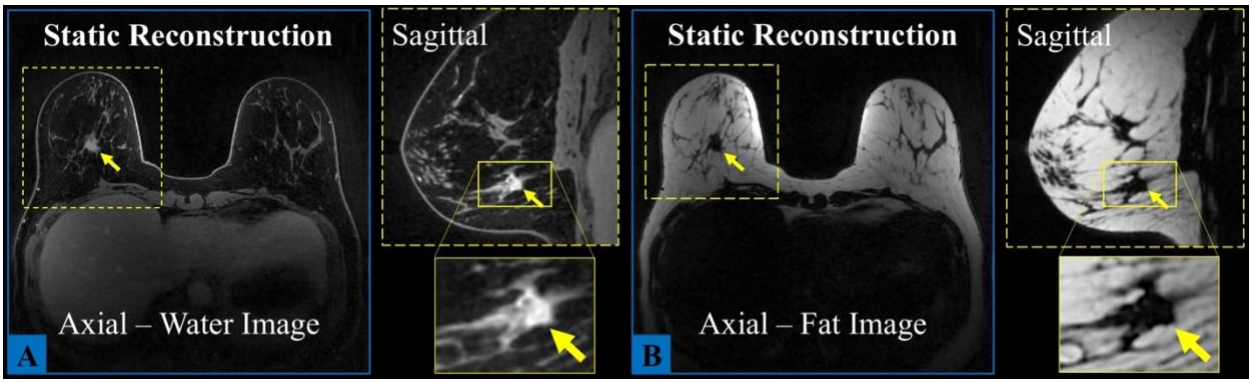

Figure 2.10 *Demonstration of static reconstruction in the prescribed axial plane and the reformatted sagittal plane using the post-contrast pass (0-180s). In both water (A) and fat (B) images, the spiculated margins of a malignant lesion, identified by yellow yellow arrows, are shown with the proposed method.*

Static Reconstruction of pass 2: As previously described, the entire pass of the enhanced VIPR CS+IDEAL can be reconstructed without mask subtraction to depict the post-contrast pass (Fig. 2.10). Water images depict high level of morphologic detail in both planes of a known breast cancer, including spiculated margin and irregular shape, as a result of the 0.8-mm isotropic resolution. Fat images provide

a negative contrast reference of the architecture of the breast. The implemented trajectory phase correction diminished the blurring effect due to fat off-resonance at 3T.

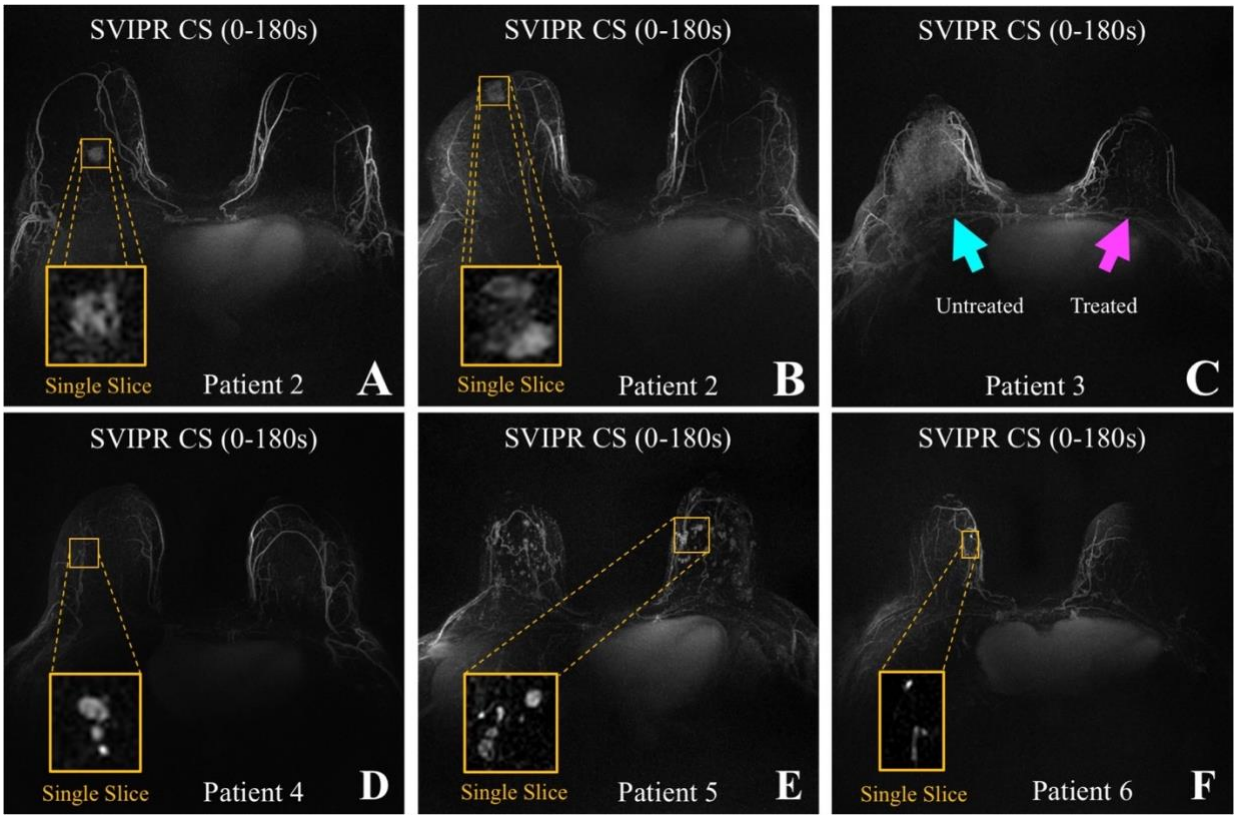

Figure 2.11 *MIPs of the complete SVIPR pass using a CS reconstruction in six patient volunteers. Breast lesions are enlarged and displayed as single slice (yellow boxes).* ***Top:*** *volunteers with known malignant cancer (A-C). Minimal background parenchymal enhancement (expected post-radiation therapy, as in this patient) is indicated in the third patient (magenta arrow) compared to the untreated breast with moderate benign background parenchymal enhancement (C).* ***Bottom:*** *Three volunteers with known benign enhancing lesions (D-F).*

CS Reconstruction of SVIPR pass: MIPs of the entire post-contrast pass (180 sec) with mask subtraction (Fig. 2.11) provide a rapid overview of the regions of increased permeability, akin to the capability shown in Kuhl's rapid screening technique[7]. In the case of the first two subjects, the abnormalities (known malignancies) in the breasts can easily be detected, as shown by the yellow boxes in Fig. 2.11A-B. Single-slice magnification shows morphologic features such as shape, size and structure. Subject 3 (Fig. 2.11C) whose left breast had undergone radiation treatment, does not show any parenchymal enhancement in the radiated breast, consistent with the expected treatment effect.

2.5 DISCUSSION

Over the past 15 years, the clinical breast MR imaging community has become increasingly accustomed to examining the entire dynamic passage of an intravenous contrast injection with submillimeter resolution in at least two spatial dimensions. However, this is achieved in routine clinical practice at the expense of temporal resolution. We present the results of a novel, constrained, iterative reconstruction methodology to provide a platform for simultaneously providing high spatial and temporal information of the early enhancement phase for an abbreviated MRI screening exam. Our technique maintains the submillimeter spatial resolution important clinically for morphologic assessment of lesions, while providing a platform to shorten the total exam time to improve patient comfort, throughput, and patient access.

Our results show preliminary experience with an ultra-fast volumetric bilateral breast MRI exam with sub-millimeter isotropic resolution, surpassing the clinical standard while providing temporal resolutions six-to-eighteen-fold faster than typical clinical protocols. Although a judicious combination of CS and view-sharing (VS) can produce high spatiotemporal resolution in various DCE MRI applications[73], the imaging performance of these methods is object dependent[74]. The local spatially variant temporal constraint is able to further exploit data redundancy by learning and modeling temporal behavior rather than the assumption of consistency over a period of time[75,76]. The method relies on the assumption that there is more data redundancy with a local sub-volume compared to the entire volume. The innovation in our proposed method is derived from interleaving echoes from a 3D radial acquisition and then exploiting mutually compatible technologies: parallel imaging, compressed sensing that exploits image space sparsity (generated with mask subtraction), and a temporal constraint (LLR). In addition, our approach allows for volumetric, unsubtracted fat/water separated structural volumes using an iterative algorithm (VIPR CS+IDEAL) in a challenging B0 environment.

Undersampling artifacts and low SNR are two of the most prominent challenges while dealing with very small temporal windows in a reconstruction. 3D radial sampling assists in reducing these problems, but it is especially beneficial in breast imaging where large volumes need to be acquired and the temporal behavior of small or heterogeneous features with varying dynamic enhancement patterns needs to be resolved. The VIPR IDEAL trajectory with the use of other technologies, such as high-count channel receiver coils and iterative reconstruction, provides an effective alternative to overcome these two problems and accomplish high spatiotemporal resolution in a bilateral breast DCE exam.

The dynamic reconstruction approach learns spatially varying models of temporal behaviors through an LLR constraint that effectively permits the temporal footprint to widen in regions of low temporal bandwidth while narrowing in regions where signal intensity is changing rapidly. Widening the temporal footprint in temporally-sparse regions provides the SNR for high temporal performance in regions of dynamic signal changes. However, if the spatial and/or temporal bandwidth of the dataset was sufficiently low, a very simple VS or temporal interpolation strategy would have worked just as well. Equivalent approaches have validated their specified temporal resolution through displaying a series of non-continuous frames with large lesions that cover up to half the breast and ROI measurements through time[43]. Due to the lack of a gold standard for high temporal resolution dynamic reconstructions, definitive validation is challenging. As one cannot determine the spatial and/or temporal bandwidth of lesions in each patient prior to examination and often even after examination, assessing the clinical capabilities of the VIPR IDEAL acquisition and STELLR reconstruction methodologies is difficult. The utilization of a digital phantom would allow for quantitative measurements to find the limits of our acquisition and reconstruction technique and validate them.

Our validation image set, with an example shown earlier in the top row of Figure 2.4, was restricted to a strict 10 s temporal footprint method (VIPR CS) that shared no data between volumetric frames. Though low in SNR, the order of enhancement can be discerned easily for many structures and

thus provided a ground truth for enhancement patterns. The proposed method (SVIPR STELLR) created temporal frames whose enhancement order agreed with the strict 10 s frames while producing better SNR. Tornado+PILS could not produce the same effect.

The static reconstruction in volumetric T1-W imaging demonstrated robust fat/water separation, which becomes an additional exam component at no additional scan time. VIPR CS+IDEAL is able to provide comparable fat/water separation to Cartesian IDEAL with six times smaller voxel size and a similar imaging performance compared to the T1-W FSPGR two-point Dixon technique. T1-W FSPGR two-point Dixon technique allowed for thinner slices in comparison with Cartesian IDEAL, but the two-point method is still constrained to in-phase and out-phase echo times. Both reconstructions described in this work exploit the 3D radial trajectory to achieve 0.8-mm isotropic spatial resolution and fulfill regularization requirements while taking full advantage of a 16-channel breast coil. In our experience, the 16-channel system was essential to creating the performance shown here relative to an 8-channel coil[77]. We have successfully demonstrated the benefits of adding the sampling characteristics of VIPR in conjunction with IDEAL to obtain high spatial resolution and flexible echo selection at 3T with T1-W contrast.

The versatile characteristics of the VIPR IDEAL trajectory enable image reconstruction in various arrangements, increasing the amount of information that can be derived from a single scan. For instance, the mask-subtracted, SVIPR CS reconstruction of the post-contrast pass as a single volume can be used as a screening tool to establish the absence of breast cancer. In case of breast abnormality findings, the same data can be reformatted and reconstructed to provide the dynamic imaging volumes depicting enhancement at 10 s frame rates (SVIPR STELLR). Moreover, additional k-space passes can be acquired to study the late perfusion in the breast if desired. The static reconstruction of the pre-contrast or post-contrast pass (VIPR CS+IDEAL) provides a volumetric, T1-weighted map of the breast at the cost of additional computing time.

The presented work creates a foundation for a robust ultra-fast imaging technique with the possibility of expansion to multiple applications outside the realm of screening. In other words, this new technology could be expanded to study the heterogeneity of tumor response during therapy, assess tumor biology, and ultimately predict prognosis and survival. However, we first plan to evaluate it for abbreviated breast screening applications, where we believe it can most quickly benefit the greatest number of women. There are additional limitations to our results. The B0 field maps obtained from IDEAL have the potential to be incorporated into the dynamic model to further correct B0 field inhomogeneity but were not used due to random-access memory (RAM) limitations and to reduce computing time. Nevertheless, reconstruction times can be dramatically reduced by computing the non-uniform FFT on a GPU[78]. Lastly, further validation to demonstrate the feasibility of our high-performance sequence for an abbreviated breast MRI is required.

2.6 CONCLUSION

We demonstrated a 3D radial breast MRI data acquisition with a dual (dynamic and static) reconstruction methodology to provide 1) 10-s volumetric frame rate with 0.8-mm isotropic spatial resolution and 2) a static, post-contrast, fat/water separated breast architecture map over a FOV large enough to image both breasts simultaneously (32 cm). Together, this dual-reconstruction approach combines capabilities for high performance acquisition, consistent fat suppression, and overcomes significant data undersampling. This combination allows assessment of lesion morphology and early-phase perfusion in a total scan time of only six minutes. It is the joint implementation of a high-performance data sampling and two constrained reconstructions that makes this capability possible. Upon further validation, this new methodology may translate to high performance, rapid breast cancer screening with MRI.

Chapter III VALIDATION

3 IN SILICO EVALUATION OF CONSTRAINED RECONSTRUCTION IN DCE-MRI FOR AN ABBREVIATED 3D RADIAL BREAST PROTOCOL

This chapter is currently being prepared for submission as a full manuscript to Magnetic Resonance in Medicine (MRM). Portions of this chapter are scheduled to be presented at the 26th annual meeting for the International Society for Magnetic Resonance in Medicine (ISMRM) on June 19th, 2018 in Paris, France.

3.1 Abstract

Purpose: To validate the effectiveness of the SVIPR data acquisition with a STELLR reconstruction in creating high temporal fidelity in a digital breast MRI phantom.

Methods: A 3D radial mask-subtracted data set (SVIPR) is reconstructed with a local low-rank (LLR) constraint to exploit the temporal data redundancy with the help of a CS algorithm in the spatial domain (STELLR). The dynamic data set is simulated with a digital phantom that is able to reproduce realistic tissues and lesions. A single dynamic data set is reconstructed using the proposed methodology and three other reconstruction schemes: Parallel imaging (PILS), PILS with view-sharing and CS. The four reconstructions are compared against the known truth from the digital phantom to validate the spatial and temporal resolution of STELLR. Signal-to-noise (SNR) measurements, mean squared error (MSE) calculations, Structural Similarity Index Measurements (SSIM), signal intensity (SI) plots and perfusion maps were used to quantitatively validate the spatiotemporal performance of STELLR.

Results: The STELLR temporal performance of subtracted data is able overcome the R=45 undersampled rate at the edge of k-space by exploiting the temporal redundancy with an LLR constraint. The STELLR reconstruction delivers 0.8-mm isotropic resolution and 10-s temporal resolution. STELLR scores on average above 0.9 on SSIM across all lesion types at all time points.

Conclusion: An in-silico simulation is able to provide a platform to assess and validate methods using image quality reference metrics. The SVIPR STELLR methodology approach maintains high temporal and spatial fidelity regardless of lesion type or size in a bilateral breast exam. The proposed methodology is a suitable technique for characterizing enhancing structures within the breast during the early enhancement phase.

3.2 INTRODUCTION

The Dynamic Contrast Enhanced (DCE) portion of the breast MRI exam is the primary tool for lesion diagnosis and patient management due to its high sensitivity[79,80]. In an effort to make this technology more widely available and cost effective in terms of MRI equipment usage time and exam interpretation time, great interest has been shown in the development of abbreviated breast protocols for screening[81,82]. Most protocols examined for use in abbreviated breast MRI consist of a subset of the sequences used in a standard clinical exam, typically a pre-contrast T1 weighted series, a single post contrast T1 weighted series, subtraction images and an MIP. Like standard clinical exams, these protocols emphasize spatial information over temporal information and rely on standard methods of reducing scan time including parallel imaging[7,83-85]. Consequently, little to no kinetic information is captured. Encouragingly, the diagnostic accuracy of these methods is not significantly different from the full protocols in a screening setting[3]. However, being able to provide perfusion information with a short protocol is expected to improve specificity and interpretation confidence[4].

Time resolved techniques such as view-sharing with the aid of parallel imaging have been widely used in clinical practice to improve temporal performance. Nevertheless, since the introduction of compressed sensing (CS) by Lusting et al. in 2007[18], constrained reconstructions, a branch of sparse techniques, have taken an important role in the advancements of dynamic imaging. This is possible due to the fact that constrained reconstructions provide greater benefits in data sets with higher dimensionality (such as 4D dynamic datasets) since information redundancy can be exploited in the additional dimensions, allowing greater acceleration. In addition, constrained reconstruction can be combined with parallel imaging and time-resolved strategies to further increase imaging performance[86].

Although new reconstructions schemes allow for greater MRI performance, little has changed since CS was introduced when it comes to validation strategies for these techniques. Furthermore, in some cases its diverged methodology from traditional methods makes comparison more challenging. A

common validation approach is to synthetically undersampled a data set and show that the reconstruction is able to provide the same information from the original fully data sampled set[44-49]. In recent years, numerous sparse reconstruction techniques have been proposed. Some of them have been able to provide temporal resolution of 10 seconds or less. Such methods are considered as Ultrafast schemes[87]. Despite these great strides in reconstruction technologies, there has been a dramatic mismatch between published efforts of the technical development of sparse reconstructions and the clinical evaluation of the technology. A current challenge with dynamic reconstruction is the ability to provide reproducible and repeatable non-invasive measurements that can serve as tools to answer the clinical questions.

Due to the lack of a gold standard for high temporal resolution dynamic reconstructions in MR imaging, definitive validation is challenging. One criteria that will be required for the widespread adoption of an accelerated dynamic clinical imaging protocol is robustness despite differences in patient size, breast tissue composition, background enhancement characteristics as well as different lesion size, morphology, heterogeneity and enhancement characteristics. Current high temporal resolution techniques have shown promising results at the cost of robustness. In other words, their performance is lesion-based since their models or assumptions do not account for lesion size or heterogeneity. In contrast, promising solutions have been proposed to characterize, evaluate and optimize performance of other medical image processing methods[88-90]. Three are three main types of assessment approaches: in vivo measurements, measurements using physical phantoms and simulation with digital phantoms. Reconstruction validation of in vivo studies are difficult to employ in accelerated MR imaging due to differences in temporal resolution between newly developed and standard protocols and lack of a known ground truth, which limits the analysis to no-reference quality metrics. Realistic anatomical phantoms are also difficult to construct or expensive which make adoption and deployment difficult. Therefore, an in silico validation can provide a reasonable compromise.

Work by previous groups has shown the value of basic numerical phantoms for validation purposes[91-93]. However, to ensure robustness of all the relevant dynamic breast imaging features

described above, a dynamic digital phantom for use in validating new accelerated MR techniques needs to provide realistic and biologically relevant digital imaging features and kinetic behavior[94]. A more advanced digital breast phantom has been developed[95-97]. It is able to simulate realistic in vivo physiology of the breast and thus provide a more rigorous validation platform. Moreover, the platform allows for a more suitable environment to compare different techniques using a similar underlying ground truth. Ultimately, validation with a realistic digital phantom is a reasonable step prior to undergoing the expense and efforts of clinical trials.

We have previously proposed an ultrafast DCE MRI reconstruction for an abbreviated breast imaging protocol[98]. Although a feasibility study with in vivo measurements has already been conducted with promising results, the goal of this work is to further validate the technique and promote the utilization of realistic digital phantoms to validate the increasing number of new reconstruction techniques. Thus, the purpose of this work is to utilize the already mentioned digital breast phantom and validate our previously published **S**patial CS with **Te**mporal **L**ocal **L**ow-**R**ank assistances (STELLR) reconstruction[98]. We provide image quality reference metrics to validate the effectiveness of the method in creating high temporal resolution time images to depict lesion enhancement over time while maintaining high spatial resolution required to characterize anatomic detail over a field-of-view (FOV) large enough to accommodate both breasts. We also compare our method with other commonly used strategies in the development of accelerated MR imaging techniques to provide a better understanding of the capabilities of our reconstruction.

3.3 METHODS

The innovation in our proposed reconstruction methodology relies on the integration of an acquisition strategy and a reconstruction approach whose characteristics complement each other[98]. Nonetheless, given all the attention that has already been given to the pulse sequence[99-101], in this work we only focus on the validation of the reconstruction scheme. Thereby, we simplify the number of dependencies in this project. The key element that describes the STELLR reconstruction is a local-low

rank (LLR) constraint to exploit the temporal data redundancy with the help of a CS algorithm in the spatial domain. This dual constrained approach takes advantage of the additional sparsity created by subtraction of the prost-contrast data from the pre-contrast mask.

3.3.1 Simulation

The base image data for the simulation was acquired using the VIPR IDEAL[98] sequence and consisted of an isotropic 3D breast volume with decomposed fat and water images. Regions defining the air, skin and breast tissue were integrated into the simulation. A graphical representation of the simulation algorithm is shown in Figure 3.1. Lesions with the desired morphology were digitally created and inserted into the baseline breast images. The desired enhancement curves were selected and assigned to appropriate breast and lesion tissues (Figure 3.1A and 3.1C). For the purposes of this simulation, four lesions with different shapes and sizes were included: 1) A lesion with spiculated morphology displaying rim enhancement (3 mm in width) and length of 20 mm in the greatest dimension, 2) a lesion with irregular morphology also displaying rim enhancement (3 mm in width) and a length of 20mm in the greatest dimension, 3) a lesion with a round morphology displaying homogeneous enhancement and a length of 12.5 mm, 4) a lesion with lobulated morphology displaying heterogeneous enhancement and a major axis of 20 mm and a minor axis of 10 mm. Simulated background parenchymal enhancement (BPE) and non-enhancing fat tissue were also included.

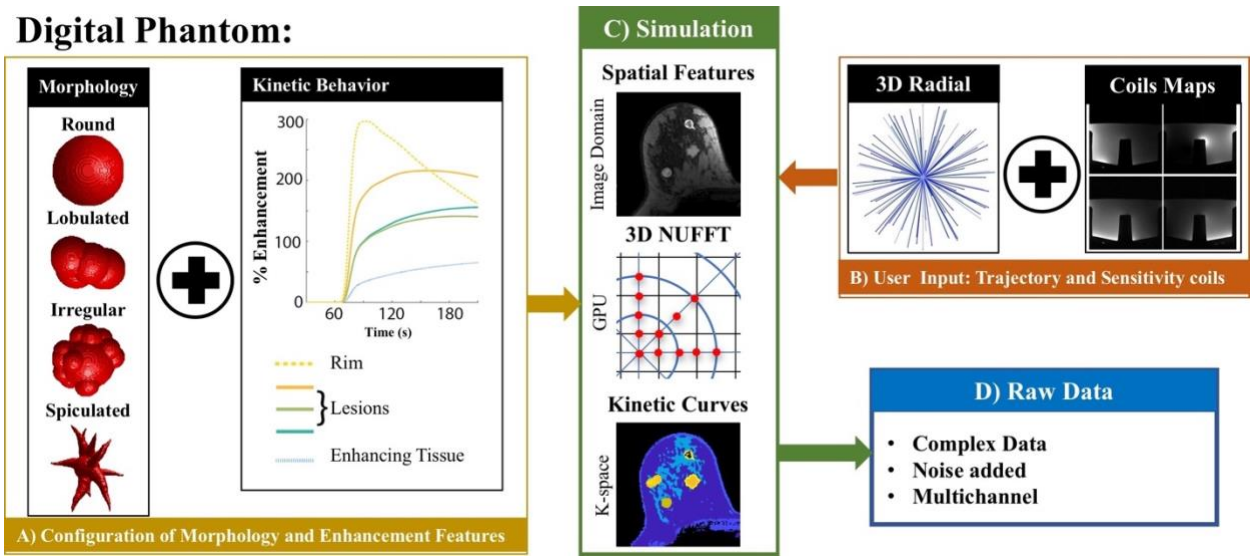

Figure 3.1 *Flow diagram illustrating the operation of the digital phantom. A) Simulated lesions with user selected morphology (representative of actual biological features), location, and kinetic behavior are generated and placed into the base breast tissue images. B) The sample locations and timing information for the desired k-space sampling pattern is defined and incorporated into the main simulation function in conjunction with sensitivity maps for each channel of the coil of interest. C) Simulaion of image domain charcateristics such as coil sensitivity maps are performed first followed by a 3D non-uniform Fourier transform (NUFFT) and simulation of dynamic behaviour such as enhancement are performed in k-space. D) The returned output consists of complex raw data consistent with the desired trajectory and coil geometry. White gaussian noise was added as a final step.*

A visualization of the simulated data set is shown in figure 3.2. Lesions were located in the central slice of the simulation for ease of visualization. Figure 3.2B shows an enhancement map of the features included in the simulation. The location of each was strategically chosen to place the lesion in a region of existing fibroglandular tissue, allowing the lesion to blend in with the fribroglandular tissue. A small percentage of BPE was added to the right breast to increase the complexity of the lesion's environment.

A k-space trajectory identical in pattern, order, location and timing from the prior in-vivo STELLR acquisition was defined for the simulation (Fig. 3.1B). Settings were selected to match the current capabilities of the clinical hardware at our institution (3T Discovery 750 system, GE Healthcare). The simulated trajectory information was designed to sample the entire k-space volume twice in a 6-minute period, producing a 3-minute pre-contrast dataset and a 3-minute post-contrast dataset (Figure 3.2C-D). This allows for a subtraction operation in k-space to increase the sparsity of the simulated dynamic raw data (Figure 3.2E). Coil sensitivity maps corresponding to a commercially-available 8-channel breast array (GE Healthcare, Waukesha WI) were obtained by scanning a water phantom designed to fit the coil. A 3D fully sampled data set was obtained and reconstructed using a low pass filter to create smooth sensitivity maps for each coil element. Both of the aforementioned inputs were used to produce a simulated, complex data set matching the 3D radial STELLR acquisition pattern and containing realistic breast anatomical information, simulated breast BPE and simulated enhancing lesions. Gaussian noise was added at a level that matched in vivo dynamic measurement from previous studies.

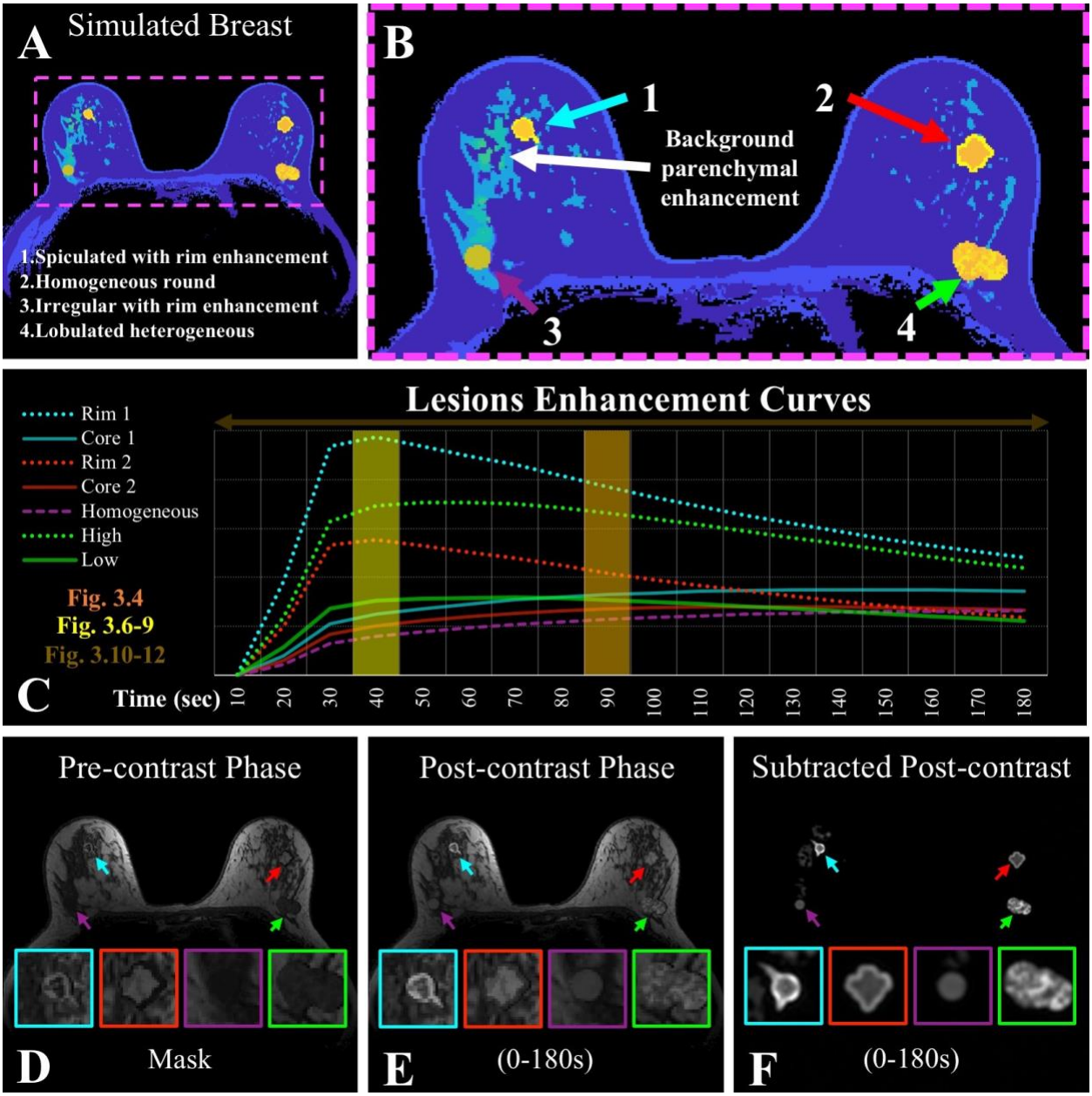

Figure 3.2 *Overview of the simulation set up. A) Central slice of the simulated breast. The various colors represent features with different enhancement parameters. B) Magnification over the breast tissue where all four lesions are indicated with arrows: 1. Spiculated lesion with rim enhancement (cyan arrow), 2. irregular lesion with rim enhancement (red arrow), homogeneously enhancing round lesion (purple arrow), 3. lobulated lesion with heterogeneous enhancement (green arrow). Regions of normal fibroglandular tissue displaying BPE are indicaited by the white arrow. C) Temporal enhancement curves for each lesion matching color scheme described in B. D) pre-contrast phase simulation. E) post-contrast phase simulation. F) mask-subtracted data set. Magnifications of all four lesions are located at the bottom of each simulation phase image (D-F).*

The reference ground truth was created using a second simulation. In this case, the acquisition parameters were intentionally changed to exceed the current hardware performance capabilities in order to produce a fully sampled 3D volume every 10 seconds. Subtraction was applied in a similar manner to

the test case to produce subtracted post contrast images. Subsequently, each fully sampled volume with 10s worth of temporal information was reconstructed using a density compensation and a Nonuniform Fast Fourier Transform NUFFT function. No noise was added to the final data. The simulation was performed with an intel-i7 desktop CPU with 6 cores and 32 GB RAM. The NUFFT portion of the simulation was performed using a NVIDIA GTX 1080 Ti GPU and the gpuNUFFT library[102].

3.3.2 Reconstruction

The mask-subtracted test data (SVIPR) set was rearranged into sets of 10 second temporal windows. As a result, 18 unique volumes were obtained with dynamic information to be reconstructed using four techniques. First, a conventional method using Parallel Imaging reconstruction (PILS)[71] to simulate standard clinical performance. Second, the same PILS reconstruction with view sharing through a tornado filter that expands its temporal footprint from 30s at the k-space center to 90s at the k-space edge (PILS+Tornado)[53] to illustrate the limitations of a linear interpolation between neighboring frames. Third, a CS reconstruction with a strict, 10s temporal footprint to show the impact of not taking advantage of temporal redundancy. Fourth, using the STELLR algorithm. Each reconstruction was normalized to eliminate the inconsistent signal gain experienced by each reconstruction.

3.3.3 Evaluation

Previous in vivo data sets were used as a reference to create realistic SNR and lesion signal intensities. A comparison between in vivo and simulated is provided to verify quality of the simulation and the importance of subtraction to achieve 10s temporal resolution. The STELLR reconstruction was compared to the other three computed reconstructions using the digital ground truth as the reference standard. A range of image quality reference metrics were used to compare and validate the effectiveness of the proposed methodology. First, image difference was calculated between each reconstruction and the digital truth. Signal-to-noise (SNR) calculation and mean squared error (MSE) were also calculated from each reconstructed image. Second, Structural Similarity Index Measurements (SSIM) were used to compare the ability of each method to reproduce each simulated feature[72,103,104]. Third, the signal

intensity (SI) time curve produced by a single pixel was compared between the known truth and each reconstruction. Finally, perfusion maps of each lesion were calculated using a commercially-available software package (NordicICE) to measure the temporal robustness of each reconstruction approach.

3.4 RESULTS

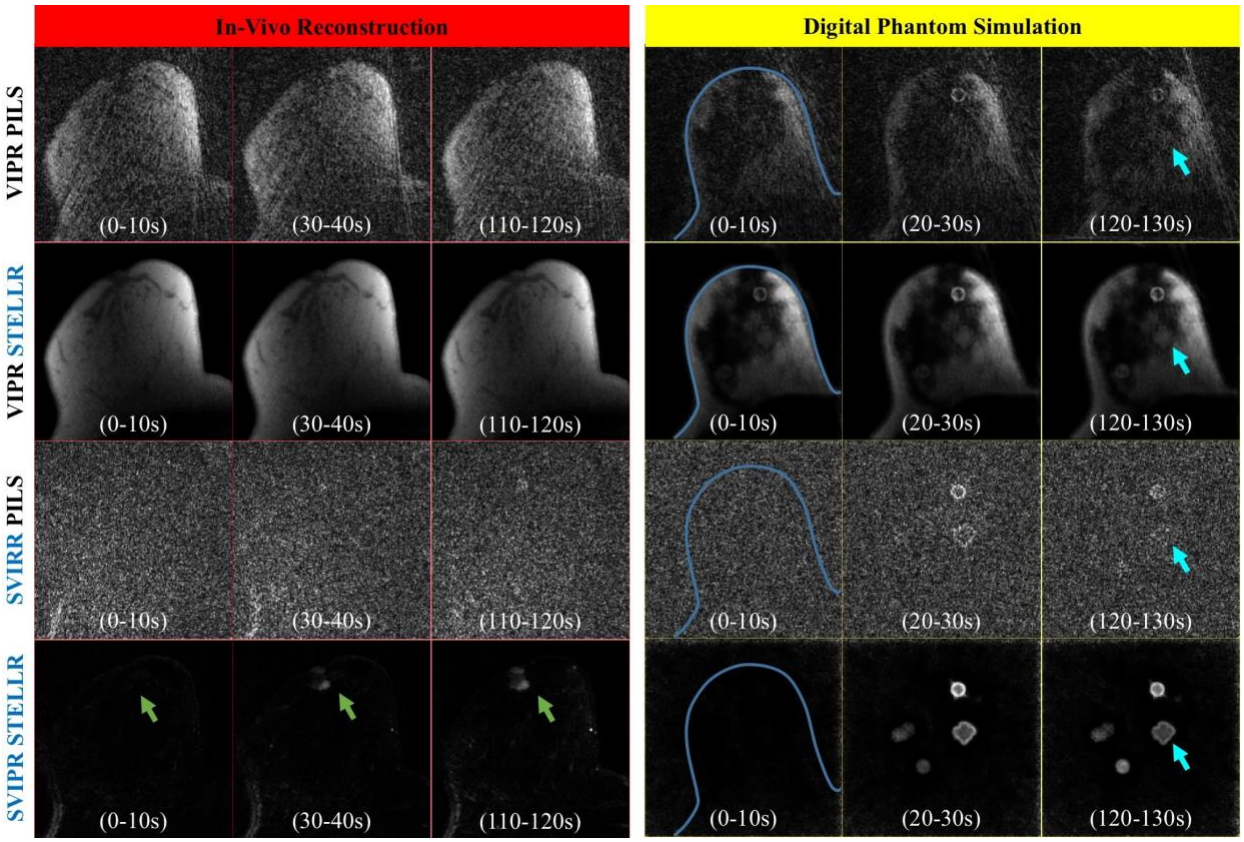

Figure 3.3 *Visual comparison between in vivo data (left) and simulated data (right). Both data sets were reconstructed using four approches. Top row: each individual 10 second volumetric frame of the post-contrast phase (VIPR) was reconstructed using parallel imaging (PILS). Second row: The same data set (VIPR) was reconstructed using our proposed STELLR reconstruction. Third row: mask subtracted post-contrast phase (SVIPR) is reconstructed using PILS. Bottom row: SVIPR data set is reconstructed using STELLR. The noise level from the in-vivo measurments was matched during the simulation.*

Comparison between in vivo and simulated reconstructions is shown in Fig. 3.3. The digital is able to simulate realistic dynamic data that matched the in vivo observations. Although STELLR is able to reduce the undersampling noise-like artifacts, subtraction is required to increase sparsity in order to resolve the lesions (green and cyan arrows). The simulation used to test reconstructions (8 channels, 384 slices, 18 frames, 2333 spokes) took 45 minutes. Simulation of the fully sampled data set used as a reference for the validation (1 channel, 384 slices, 18 frames, 42000 spokes) took 1:05 hours. Image reconstruction was performed on an AMD-Opteron CPU computer node with 32-cores and 120 GB RAM. Reconstruction time for the dynamic STELLR reconstruction dataset (8 channels, 384 slices, 18 frames, 2333 spokes) was 10:50 hrs.

3.4.1 Absolute Difference Images

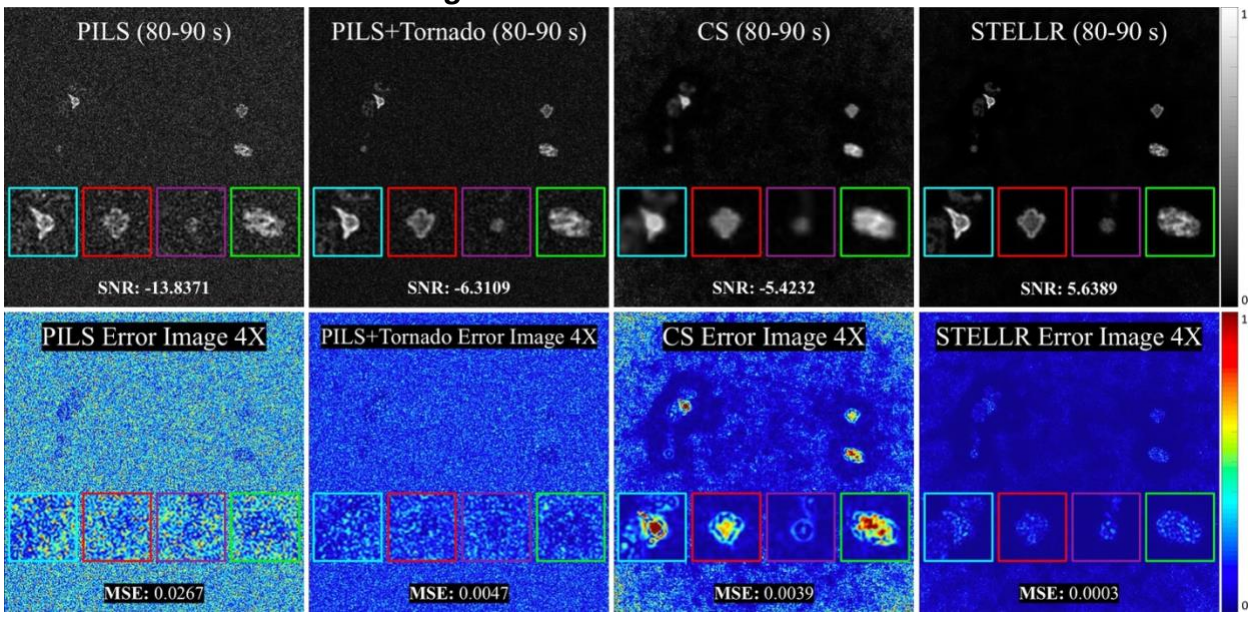

Figure 3.4 *Comparison of reconstruction techniques displayed in the same central slice as shown in Figure 2B.* ***Top:*** *A 10-second volumetric frame from the mask-subtracted enhanced data set (SVIPR) is reconstructed using four techniques: PILS, PILS with a tornado filter, CS and STELLR. SNR measurements from each technique are also shown.* ***Bottom:*** *an absolute difference image is shown between the digital reference and each reconstruction approach. PILS shows high noise levels that make lesion visualization more difficult. PILS+Tornado is able to decrease the noise levels. CS is not able to reduce the apperance of the noise at the expense of increased image blurring. STELLR provides an improved spatial resolution with the smallest error from the known truth.*

Figure 3.4 displays a 10-second, subtracted time frame for STELLR and the other reconstruction methods as well as absolute difference images. SNR measurements are performed on the subtracted time frames while MSE measurements are performed on the difference images. Negative SNR measurements, given in decibels (dB), from PILS, PILS+Tornado and CS are the result of the high background noise due to the noise like undersampling artifact produced by 3D radial reconstruction methods. STELLR, with a positive SNR of 5.6 dB, is able to overcome the 45X undersampling rate at the edge of k-space. STELLR is able to capture the lesion morphologic features, including spiculated margins and an irregular shape while matching image contrast from an 80-90s volumetric reference time point. These qualitative findings are corroborated by absolute difference images between STELLR and the digital truth shown in Figure 3.4. In addition, STELLR measures the highest PSNR (35.2) and the smallest MSE (0.0003), which is one order of magnitude smaller than the next best performing method. The wider temporal

footprint from the tornado filter is able to reduce the noise level in half while CS takes advantage of the contrast between lesion and background to reduce noise in the regions adjacent to lesions.

3.4.2 Spatial Comparison

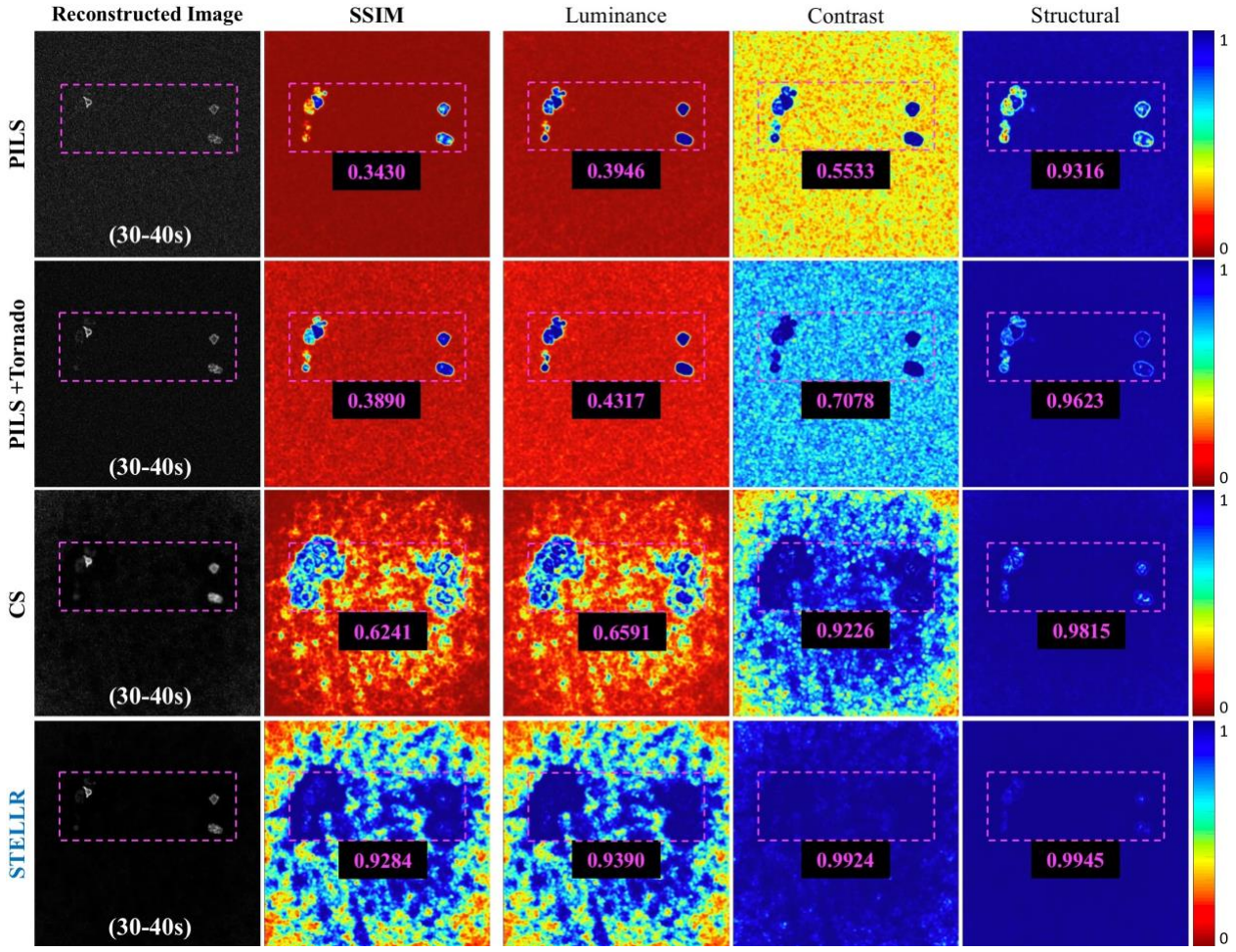

Figure 3.5 *Similarity between digital reference and each test reconstruction using SSIM. A single slice from the fourth temporal volume containing kinetic information from 30 to 40 seconds post-contrast is displayed in the first column. A SSIM map for each reconstruction is shown in the second column. The SSIM is decomposed into its three components: Luminance, contrast and structure (columns three to five). Pink numbers show the average score within the pink ROI where most of the breast tissue is located. All reconstructions show high scores in the structural component. Only STELLR is able to score high in the contrast portion. Luminance is the component in which every method scores the lowest.*

SSIM measurements not only provide an index to quantitatively compare two methods but also provide maps to visually compare their similarity. From a normalized scale where 1 is the highest score (blue color in the maps), STELLR obtains the highest indexes in all three SSIM components (luminance, contrast and structure) resulting in an above 0.92 mean SSIM index. The red areas in the STELLR

luminance map at the periphery of the image are a result of noise present outside the breast tissue. CS is able to score high (above 0.9) on two components while PILS and PILS+Tornado only on one. In contrast to consistent red background from PILS and PILS+Tornado, the non-uniform performance over the background seen in CS and STELLR as wide range in colors is the result of the addition of structure to the noise.

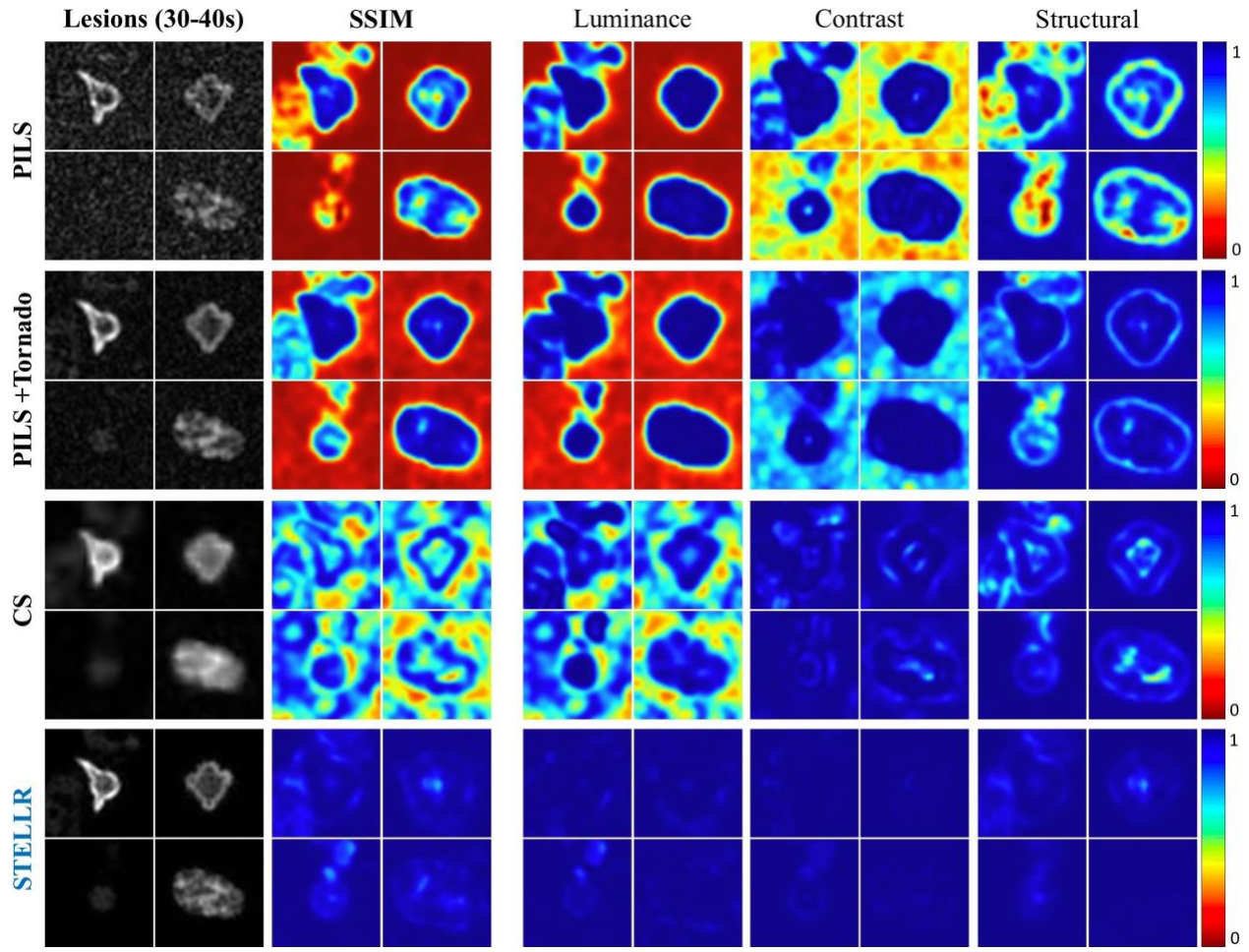

Figure 3.6 *Magnification of all four lesions across all reconstructions (column 1). Magnification of SSIM maps and their breakdown components are also displayed in columns 2-5. The two more challenging lesions to resolve for PILS, PILS+Tornado and CS are the spiculated heterogeneous lesion with rim enhancement or lesion 1 and the round homogeneous lesion or lesion 3. STELLR scored the highest SSIM for all lesions.*

A magnification of all lesions and their SSIM maps are shown in Figure 3.6. Due to the unique shape, enhancement pattern and size, each lesion represents a unique challenge for all reconstruction approaches. Lesion 1, spiculated lesion, is particularly challenging due to its high signal range between the enhancing rim and the core. The addition of BPE that surrounds the lesion just increases its difficulty.

PILS and PILS+Tornado with their relatively high noise (red color luminance column) are not able to resolve most of the BPE structure. Lesion 3, circular lesion, although homogeneous its low enhancement pattern makes it hard to resolve. CS is able to dramatically reduce noise but suffers from overgeneralization errors that appear as blurring. Consequently, lighter blue areas as seen on the structure map compare to PILS+Tornado although the opposite is seen in the contrast maps. STELLR renders each lesion with smaller errors than any of the other reconstructions.

3.4.3 3D Spatial Performance

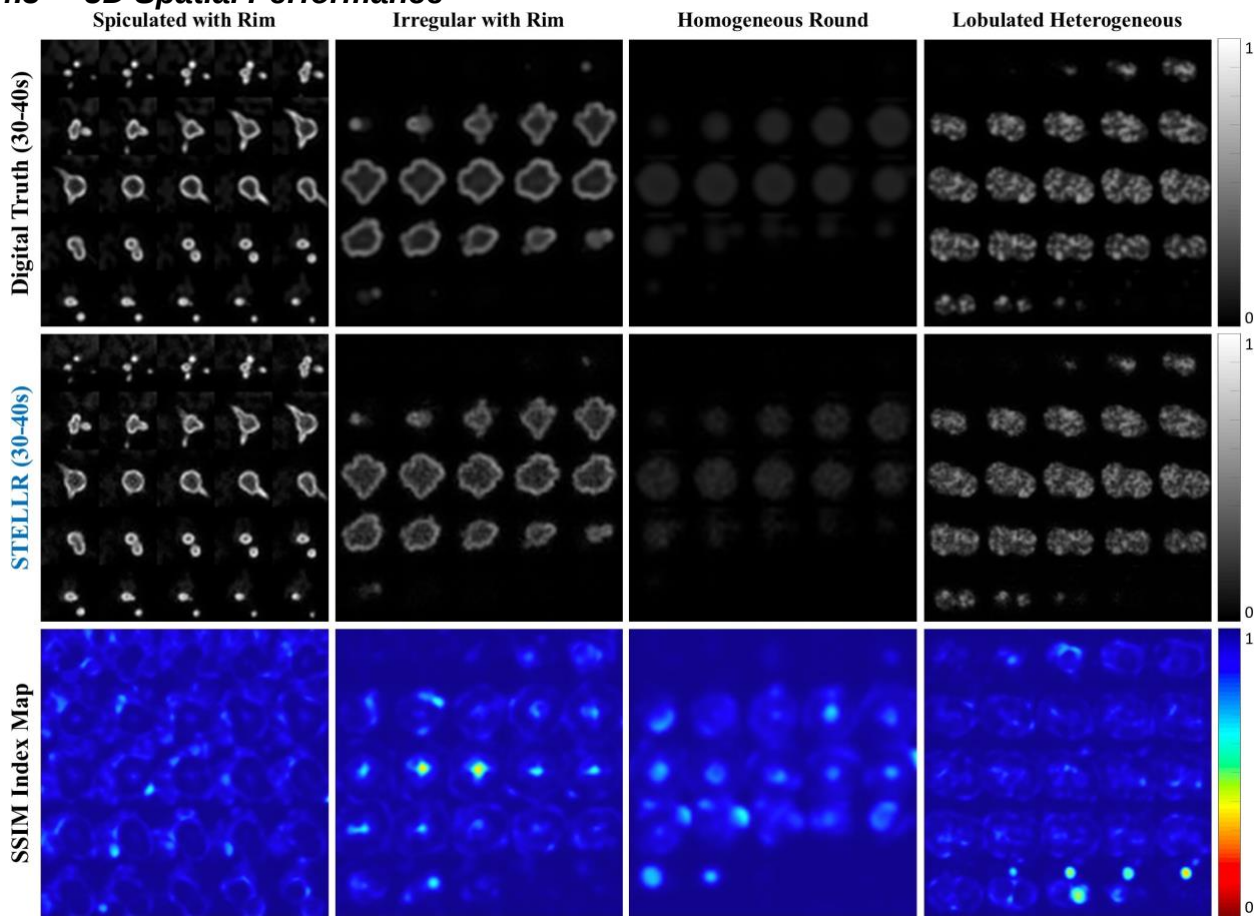

Figure 3.7 *ROIs capturing each lesion over 25 slices from the 30-40s volumetric frame. Top row shows the digital truth, middle row STELLR reconstruction and bottom row the SSIM index map for each lesion. STELLR scores high (above .9) in most areas, except for the core of lesion 2 and edges of lesion 4.*

Figure 3.7 provides a visualization of all slices that cover each lesion. STELLR scores an average SSIM index value of 0.94 across each lesion volume. There is a small performance drop, light blue areas, at the edge of the lesion when morphologic features are reduced to a couple of pixels. Additionally, a

small performance decline is also present at the core of the lesions. Nevertheless, most of the morphologic features such as shape, size and structure can be seen with detail throughout the volume of each lesion. The reduced background noise increases SNR and image contrast. The complex heterogeneity enhancement of lesion 4 can be appreciated and the small spicules from lesion 1 as well. Lastly, STELLR is able to reduce the floor noise without overgeneralization problems.

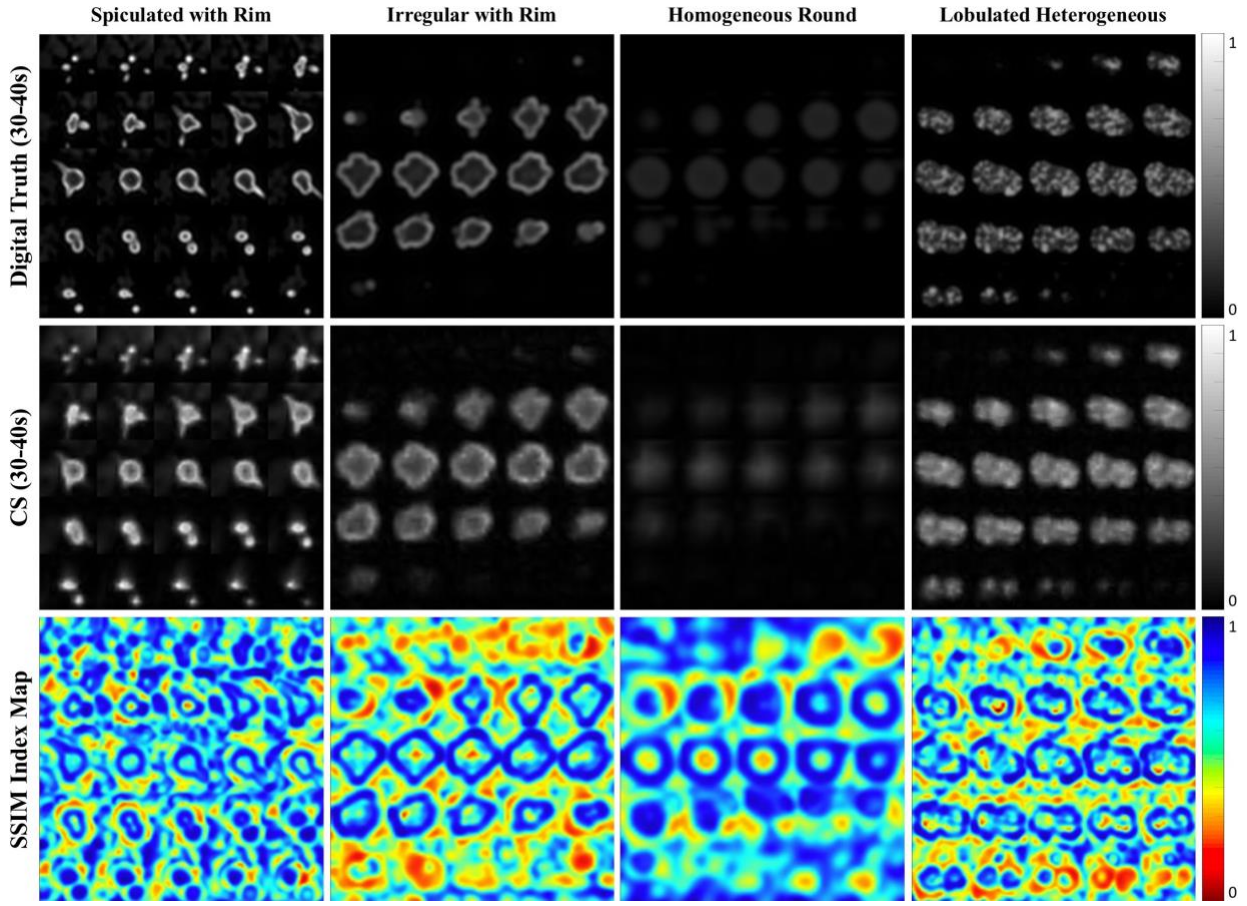

Figure 3.8 *ROIs capturing each lesion over 25 slices from the 30-40s volumetric frame. Top row shows the digital truth, middle row CS reconstruction and bottom row the SSIM index map for each lesion.*

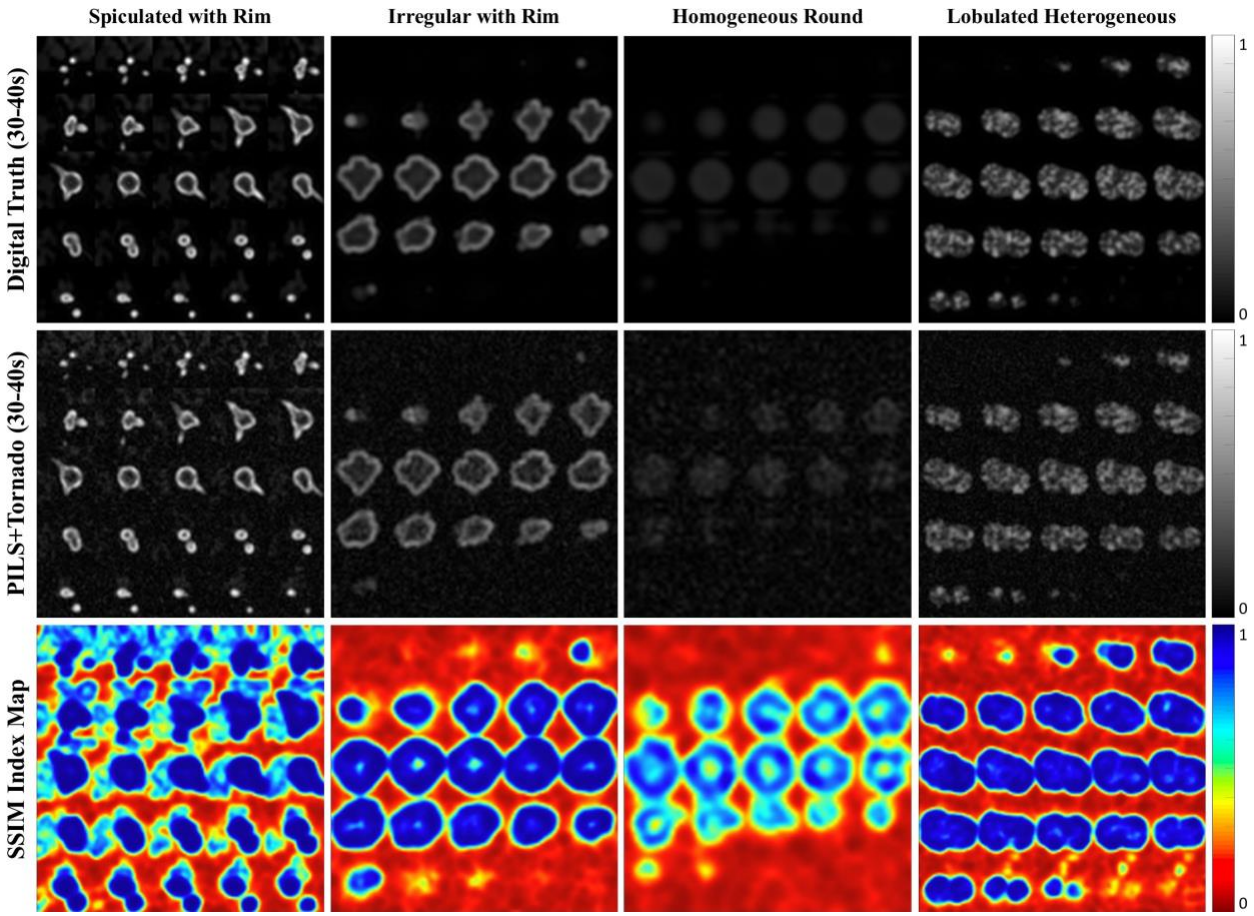

Figure 3.9 *ROIs capturing each lesion over 25 slices from the 30-40s volumetric frame. Top row shows the digital truth, middle row PILS+Tornado reconstruction and bottom row the SSIM index map for each lesion.*

3.4.4 Temporal Performance

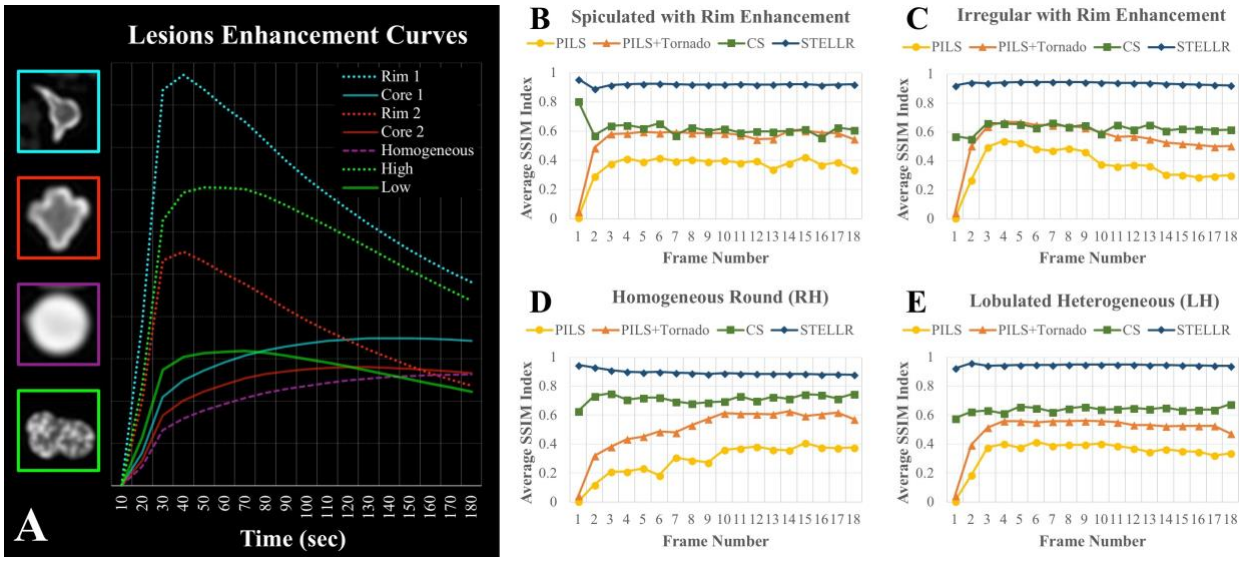

Figure 3.10 *Digitally-generated dynamic patterns for each lesion are shown on the left side (A). The average SSIM for each lesion is displayed through time for all reconstructions methods (B-E). PILS and PILS+Tornado score inadequately during the first three temporal measurements while CS and STELLR are able to maintain consistant scoring for all lesions. STELLR maintains a high SSIM scoring regardless of lesion type, dynamic pattern or size.*

The average SSIM measurements for each lesion over each time point are shown in Figure 3.10. The fastest dynamic changes occurred within the first 40 seconds (Fig. 3.10A). PILS and PILS+Tornado fail to correctly produce the first three time points and gain stability once peak enhancement is reached in all lesions. Additionally, small drops in performance are visible in lesion 1, 3 and 4, due to the tornado filter (Fig. 3.10B and 3.10D-E). STELLR not only obtains the highest average SSIM index in all lesions, but also shows the most stable performance which translates into robustness. STELLR scores at each time frame above 0.9 whereas CS with its strict 10s temporal footprint around 0.7. PILS and PILS+Tornado is lesion dependent with an average SSIM index of 0.4 and 0.6, respectively.

3.4.5 Dynamic measurements

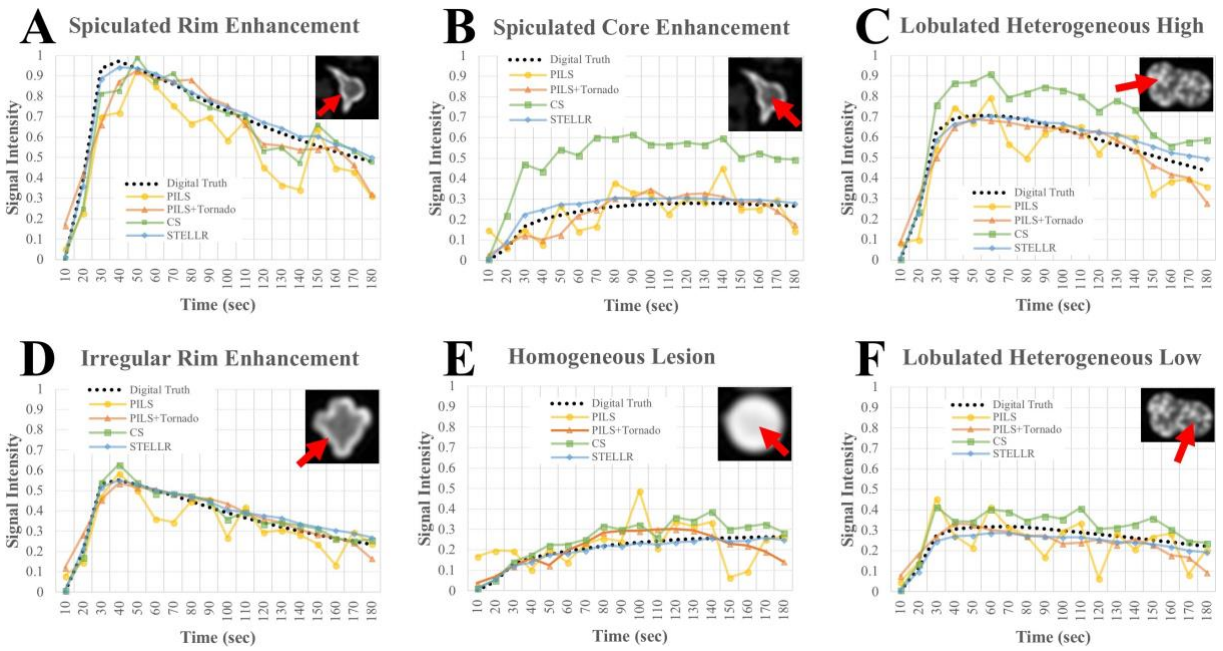

Figure 3.11 *Six single-pixel measurements are plotted across time. Each location measures the signal intensity of a particular kinetic feature within the lesions. A) The rim enhancement pattern of the spiculated lesion. B) The core of the same lesion. C) A high area within the lobulated heterogeneous lesion. D) The rim enhancement of the irregular lesion. E) the center of the circular homogeneous lesion. F) An enhancing area with low intensity profile in the lobulated lesion. Kinetic curves for all four reconstructions and digital truth are included in all ROIs (A-F).*

Kinetic curves from each method are compared against the digital truth (Figure 3.11). The curves from PILS are unstable as a direct result of the noise. The 30 second base temporal footprint from PILS+Tornado results in a temporal rounding of the signal, resulting in a delay to capture the fast-moving enhancing rim of the spiculated lesion (Fig. 3.11A). The fluctuations seen in the PILS measurements and the average error, particularly at the end points of the curves, from PILS+Tornado would compromise accuracy in any quantitative or semi-quantitative analysis. CS is able to represent the correct shape, but in areas with low contrast the high regularization weights used to reduce noise creates an incorrect signal gain which results in scaling issues (Fig. 3.11B-C). Across all measurements, STELLR is the closest to the truth in every instance, showing the correct scaling and shape.

3.4.6 Perfusion Maps

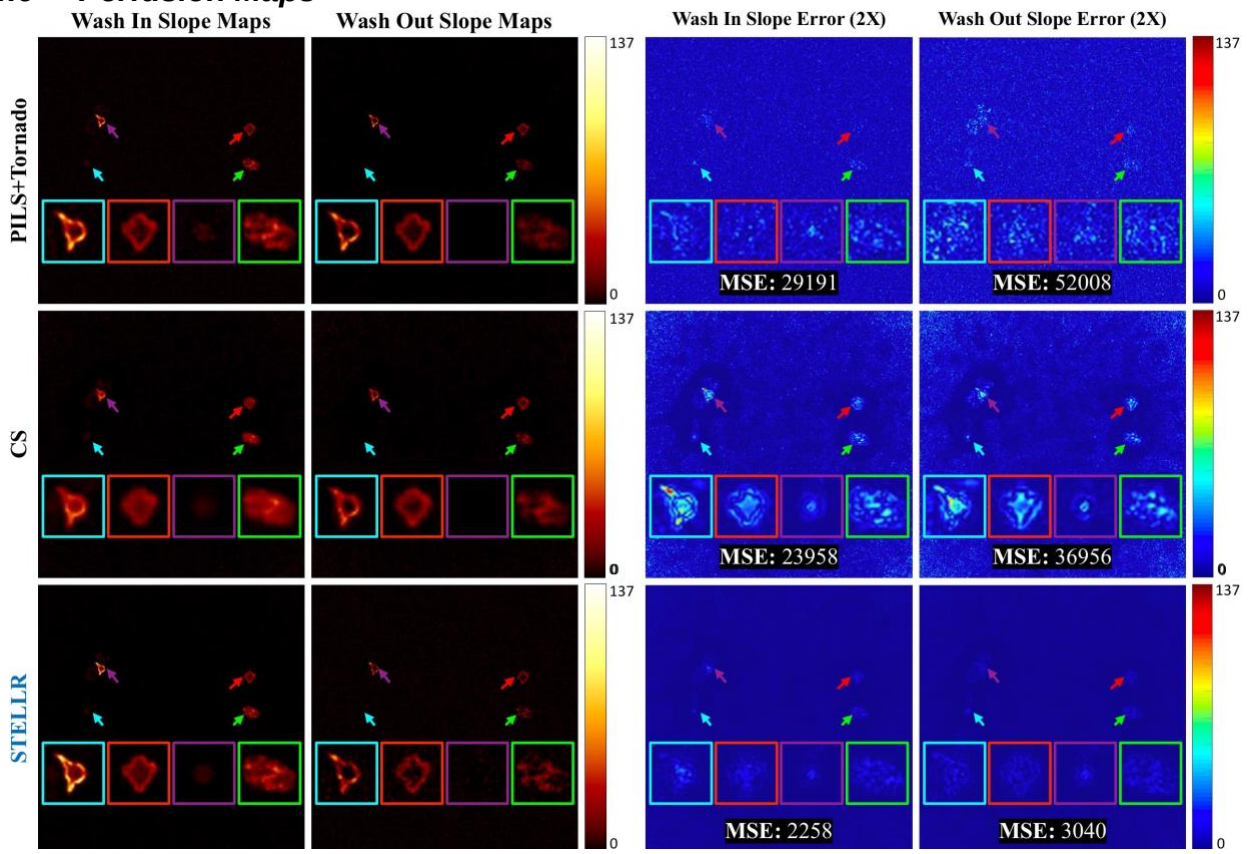

Figure 3.12 *Two perfusion maps, wash in slope and wash out slope, are displayed for each reconstruction (left columns). The first four temporal volumes were used to calculate the wash in slope while volume 5-18 were used for the wash out slope. Absolute value image difference between perfusion maps and digital truth are displayed on the right. Magnification of all lesions and their location is shown throughout using the same color scheme.*

Wash in and out slope maps for PILS+Tornado, CS and STELLR are shown in Figure 3.12. PILS was omitted due to its high noise levels. All displayed reconstructions are able to render the pixels with high intensity enhancement across time. CS shows structural discrepancies between the known truth in both perfusion maps across all lesions. Surprisingly, PILS+Tornado is able to provide a better perfusion map than CS despite the higher noise. STELLR is the reconstruction with overall less error in each lesion. Consequently, higher perfusion details are observed in both perfusion map renderings. Thus, darker blue regions are clearly visible in both STELLR perfusion error maps. The mean square measurements are an order of magnitude smaller in STELLR in comparison with the other two reconstructions.

3.5 DISCUSSION

Though numerous accelerated methods have been proposed, very little validation of the information they derive has been generated due to the complexity of testing reconstruction methods and lesion-dependent imaging performance without a reference standard for comparison. An in silico simulation is able to provide a platform to assess and validate methods using image quality reference metrics. We present validation results for a new, constrained, iterative reconstruction in its ability to provide high spatiotemporal resolution for an abbreviated screening exam. The STELLR reconstruction is able to provide 10 seconds volumetric frame rate to model the perfusion in the breast while maintain 0.8-mm isotropic resolution. Such performance capabilities provide the means for 6 minutes single scan that simultaneously provides morphologic and kinetic information.

Our simulation results show that STELLR is able to surpass clinical temporal performance by six-to-eighteen-fold faster compared to the typical 60-180s temporal resolution[14,15]. Although, the benefits from a higher channel breast coil are expected to improve temporal performance for most reconstruction through parallel imaging, it is not enough to compensate required undersampled rates to achieve 10-second temporal resolution in a bilateral breast exam. The addition of view-sharing schemes is able to reduce noise-like artefacts due to undersampling at the cost of some temporal averaging over fast enhancing lesions. However, due to the relatively slow enhancing pattern of most lesions, view-sharing approaches are expected to misrepresent a small percentage of lesions or features. Furthermore, CS reconstruction studies have been used to successfully denoise undersampled images. Nevertheless, three spatial dimensions do not provide the necessary dimensional redundancy to overcome the presented undersampled rates. Even though combination of view-sharing and CS has shown some success[73] where CS takes advantage of the artifact reduction due to undersampling (noise-like) and reduces or even eliminates the overgeneralization error (blurring) seen in our results, the averaging mismatches due to the sharing of temporal information will not disappear. STELLR, a spatial CS reconstruction with a

temporal LLR constraint shows to be a more robust alternative to explain the redundancy of a dynamic data set.

The LLR portion of the reconstruction allows the algorithm to adjust the temporal behavior in a spatially variant pattern, effectively permitting the temporal footprint to contract in heterogeneous areas and expand in more static regions. This non-linear approach provides better performance over high spatial and/or temporal bandwidth in comparison to approaches where neighboring frames and a linear interpolation are used to estimate dynamic changes. Essentially, STELLR is able to further exploit data redundancy by learning and modeling the temporal behavior rather than assuming consistency over a period of time[75,76]. Though, a judicious selection of weighting between spatial and temporal constraints is necessary to prevent the overgeneralization errors shown with the CS reconstruction.

The quantitative metrics shown in Figure 3.4 (SNR, PSNR, MSE) provide a more realistic measure of the methods performance when compared to a known truth. Moreover, the SSIM measurements are able to deliver a quantitative and visual comparison between techniques. Decomposing the SSIM index into multiple components facilitates the understanding of the effect of image processing of each reconstruction (Fig. 3.5-7). STELLR delivers consistent high spatial resolution regardless of lesion type, size or shape. The SSIM measurements from every time point also demonstrate STELLRs robustness at providing high spatiotemporal resolution (Fig. 3.10). Kinetic results (Fig. 3.11-12) encourage the use of STELLR in semi-quantitative analysis. The wash in slope map, a per pixel calculation, allows us to see the effectiveness of STELLR at predicting the enhancement peak. Malignant lesions are expected to have a higher slope. Similarly, the wash out slope is used to characterize findings. Benign cancer lesions tend to reach a plateau pattern while malignant lesions have a high slope. Although, a large in vivo sample group will be required to definitively validate and assess the clinical impact of the STELLR reconstruction, the high scoring among multiple metrics provides a confirming argument towards its validation.

Finally, though STELLR was originally developed to work with VIPR IDEAL trajectory for an abbreviated breast MRI protocol, it can be expanded to multiple applications. For instance, at the cost of losing the four unique echoes to decompose fat/water images, the 3D radial trajectory can be modified to double its sampling performance, which is expected to increase STELLR temporal resolution. Concurrently, there are some limitations to our results. The simulation omitted the use of multiple percentages of BPE to reduce the number of variables in our analysis. Also, no venous perfusion was simulated to minimize the time dedicated to the base data set for the digital phantom. Lastly, a GPU-compatible STELLR reconstruction has not been developed. Our current hardware set up performs the non-uniform FFT in 120 seconds on average while the same step up using the GPU in the digital phantom simulation takes around 1.8 seconds. The dramatic difference is reflected in the reported computing times.

3.6 CONCLUSION

A digital phantom provides a means of simulating a realistic DCE breast MR imaging environment and allows analysis results to be compared to a known ‘truth’. We demonstrated a high temporal resolution STELLR reconstruction that is able to provide detailed visualization of lesion morphology regardless of their size or heterogeneity. STELLR is able to produce 10s volumetric time rate with its 0.8-mm isotropic resolution over a FOV of 32 cm to fulfill the minimum clinical requirements. A 3D radial trajectory and subtraction of the dynamic data is essential to achieve high spatial and high temporal resolution. Upon further clinical validation, this new methodology may translate to high performance dynamic reconstruction for breast MR imaging in clinical practice.

Chapter IV CLINICAL STUDY

4 A PILOT STUDY FOR AN ABBREVIATED 3D RADIAL BREAST MRI PROTOCOL

This chapter is currently being prepared for submission as a full manuscript to the Journal of Magnetic Resonance Imaging (JMRI).

4.1 Abstract

Purpose: To compare the feasibility of a single acquisition 3D radial abbreviated MR protocol versus an abbreviated breast MR protocol using standard-of-care sequences.

Methods: Three MR imaging series from a full diagnostic, standard-of-care Cartesian MR protocol are used to retrospectively recreate an abbreviated breast MR protocol on 11 patients. The same 11 patients were invited for an IRB-approved, HIPAA compliant experimental study using an abbreviated 3D radial acquisition (VIPR protocol) on a different day. The single acquired data set is reconstructed three times to provide unique components: A single phase reconstruction (SVIPR CS), a dynamic reconstruction (SVIPR STELLR) and a fat/water decomposition reconstruction (VIPR CS+IDEAL). A comparison between both protocol outputs is presented to demonstrate the capabilities and potential benefits of the VIPR protocol.

Results: The VIPR protocol is able to deliver visually comparable morphologic detail and additional perfusion information when compared to the Cartesian protocol. The 10s temporal resolution using the SVIPR STELLR reconstruction captures the early enhancement phase of breast lesions. The 0.8 mm isotropic spatial resolution of the VIPR protocol allows for clear visualization of anatomy in three planes. The fat/water decomposition reconstruction achieves a more uniform fat suppression than the clinical protocol while offering additional fat images for screening interpretation.

Conclusion: Abbreviated breast MR protocols reduce costs and increase throughput, but must preserve diagnostic accuracy. The additional perfusion information from the abbreviated VIPR protocol, in comparison to the abbreviated Cartesian protocol, has the potential to increase interpretation confidence and sensitivity during a breast cancer screening setting.

4.2 INTRODUCTION

Clinical breast MRI studies often have lengthy protocols that make them inherently expensive and time-consuming. Dynamic Contrast Enhanced (DCE) T1-weighted breast MR imaging is the most import component of breast MRI protocols due to its high sensitivity[82] for the detection of breast cancer. Gadolinium-based contrast agents are used in MRI to detect abnormal tumor vascularity (neoangiogenesis) during the perfusion phase by enhancing the contrast between normal and pathologic tissues[105]. The morphological details in conjunction with perfusion information are the primary tools used clinically to characterize breast lesions. To accurately characterize lesion morphology, higher spatial resolution has become the norm through the use of modest temporal resolution, improved coil arrays, 3T imaging, and new MR acquisition methods. The information obtained from these dynamic contrast enhanced (DCE) exams has made MR the most sensitive imaging technique for detecting breast cancer[31]. However, shortening MR breast protocols is a key requirement to reduce cost and improve patient access to this powerful imaging tool for the detection of breast cancer.

In an effort to achieve this goal, abbreviated protocols have emerged in recent years[81]. Recent findings by two independent groups using abbreviated MR breast protocols that focus on the initial enhancement phase with modest spatial resolution have received significant interest. First, Kuhl et al. maintained sensitivity to cancer detection with subtraction of a single pre-enhancement volume from a post-enhancement volume[7]. Second, studies of 7 second snapshots of the initial enhancement phase, albeit at a clinically significant loss of spatial resolution, demonstrated the value of higher temporal resolution during initial enhancement by obtaining statistically significant differences between benign and malignant lesions[8,9]. Although both methods compromise either spatial or temporal resolution, they suggest that an abbreviated protocol with only a shortened DCE scan is able to provide the diagnostic accuracy comparable to that of the conventional full MRI protocol with an extended DCE acquisition.

Another advantage of abbreviated protocols over full diagnostic protocols is interpretation time. In some cases, interpretation time for the abbreviated protocols was faster than screening digital

mammography, which take 2-4 minutes on average[106,107]. Studies using abbreviated breast MRI protocols for screening have reported interpreting times from 3-120 seconds with an average of 57 seconds[7,83-85]. Furthermore, diagnostic accuracy was not significantly compromised when compared with the full diagnostic protocols in any of these studies. The already mentioned abbreviated protocols for MRI screening shorten the acquisition time but only provide morphologic information about enhancing lesions. The protocols lack the kinetic information obtained with the full diagnostic protocol because the additional sequences required to generate temporal enhancement time points are not included. A much faster imaging technique is required to provide temporal information of the initial enhancement phase in addition to high spatial resolution imaging within the same, abbreviated scan time. Thus, an ideal breast MRI protocol would have a fast acquisition time, as the abbreviated protocol does, but also allow extraction of kinetic information.

Providing simultaneous high spatial (submillimeter) and high temporal (10 s or less) resolution is technologically challenging in MRI. The use of view sharing techniques and parallel imaging have been the main means by which clinical MRI performance has been increased[108]. However, Cartesian techniques and current hardware capabilities make this task difficult. Most clinical breast DCE MR exams have submillimeter resolution in only two planes and temporal resolutions on the order of 60-180 seconds[14,15]. More successful methods have introduced non-Cartesian sampling trajectories and constrained reconstructions [35-40]. However, all these ultrafast DCE-MRI protocols maintain the same long DCE scan methodology in order to either use semi-quantitative measurements or pharmacokinetic analysis to evaluate perfusion. The assumption is that the adoption of an ultrafast abbreviated DCE-MRI method will be able to increase specificity while reducing overall acquisition time[109]. As a result, four studies have been able to dramatically increase imaging performance with 10 seconds or less temporal resolution[110-113]. Though, due to the competing nature between spatial and temporal resolution, such performance comes at a cost of spatial resolution. These studies increase slice thickness and/or are not

able to achieve submillimeter spatial resolution. Moreover, most of these methods rely on view sharing to increase temporal resolution which can lead to artifacts when executed aggressively and misrepresentation of small or heterogeneous features[41].

We recently presented a framework for an ultrafast DCE-MRI protocol that is able to provide high spatiotemporal resolution for an abbreviated breast exam[98]. We proposed an ultra-fast (10 s) volumetric bilateral breast MR imaging exam with 0.8-mm isotropic resolution, surpassing the current standard clinical resolution while providing temporal resolutions six-to-eighteen-fold faster. We described a single 6-minute scan that is able to provide morphology and perfusion information within the first 3 minutes of post-contrast enhancement. Rather than trying to recreate clinical data sets, we show the value of our technique by demonstrating additional kinetic and morphologic information that standard sequences are not able to display by intra-individual comparison. Thus, the purpose of this work was to compare our method with the current clinical capabilities of standard abbreviated exam in a pilot study to demonstrate the potential benefits of a non-Cartesian trajectory and iterative reconstructions in clinical practice.

4.3 METHODS

Our method relies on an efficient trajectory that combines different techniques to produce three different reconstructions from the same base dataset, each providing a unique set of information. First, a single phase, high spatial resolution reconstruction, referred as SVIPR CS, is used to produce a post-contrast, subtracted maximum intensity projection (MIP) that can be used to determine the presence or absence of lesions and evaluate their morphology. Second, a dynamic reconstruction, referred as SVIPR STELLR, with 10-second temporal resolution and submillimeter isotropic spatial resolution is used to capture perfusion within the breast using a local low-rank (LLR) implementation during the early phase enhancement. Third, a fat/water reconstruction (VIPR CS+IDEAL) produces post-contrast, fat and water separated anatomical images of the breast.

4.3.1 Data Acquisition

We use a modified version of the 3D radial sampling trajectory known as Vastly undersampled Isotropic Projection or VIPR[50] with four unique sampling patterns for each echo, which was previously introduced as VIPR IDEAL[51]. The incoherent aliasing artifacts due to undersampling produced by this trajectory meet the requirements for constrained reconstruction algorithms[52]. The efficient acquisition pattern starts sampling immediately after excitation and creates variable density towards the periphery of k-space. Bit-reverse is used to generate a pseudorandom order of each projection.

In this work, we used one T1-weighted, radiofrequency (RF) spoiled gradient echo sequence with a bipolar 3D radial trajectory that acquires two identical sample sets or passes. Each sample set requires three minutes of scan time. The first sample set (Pass 1) is the precontrast mask and the second set (Pass 2) starts as the contrast agent is administered (Figure 4.1).

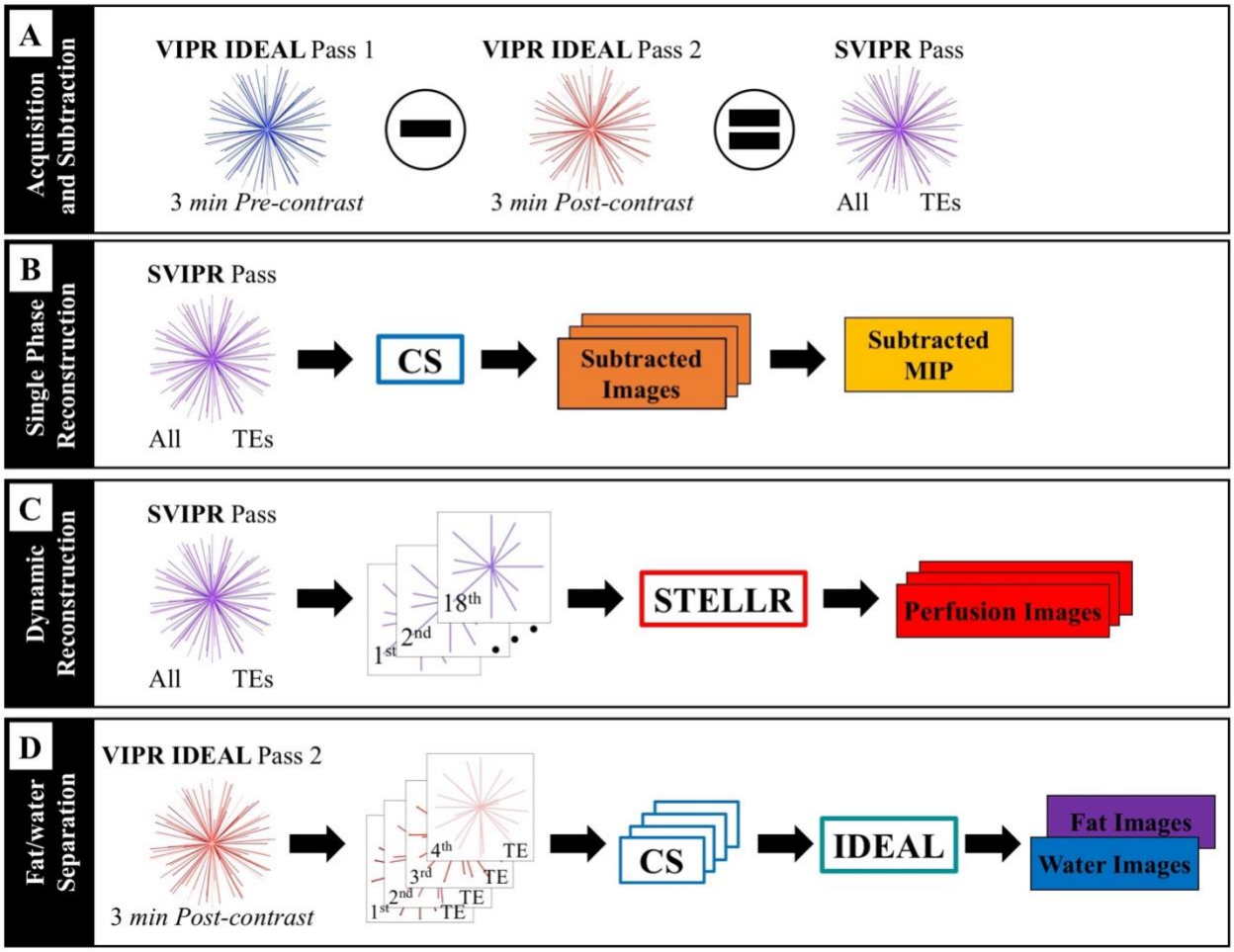

Figure 4.1 *Diagram work flow showing the data acqusition and each of the reconstruction techniques. A) data acquisition of VIPR IDEAL Pass 1 and 2 followed by mask subtraction in k-space to create a subtracted VIPR pass (SVIPR). B) Single phase reconstruction (SVIPR CS): The subtracted VIPR pass data is reconstructed using a compressed sensing (CS) algorithm to produce single slice images and a maximum intensity projection of the subtracted post-contrast phase. C) Dynamic reconstruction (SVIPR STELLR): The subtracted VIPR pass data is time-gated as a preprocessing step for a STELLR reconstruction algorithm, which produces a dynamic time series. D) Fat/water reconstruction (VIPR CS+IDEAL): The second, post-contrast pass of the scan, VIPR IDEAL Pass 2, is divided into individual echoes and reconstructed using a CS algorithm which is then fed into a chemical shift encoded fat/water decomposition algorithm (IDEAL) to generate fat and water images of the post-contrast phase.*

4.3.2 Reconstructions

The VIPR IDEAL trajectory increases the quantity of information that can be derived from a single scan due to its versatile characteristics that enable image reconstruction in multiple arrangements. All three reconstructions are designed based on a Projection Over Convex Sets (POCS)-type algorithm to produce constraints in the reconstructions[19]. Each constraint aims to exploit a particular feature within the acquired data. Additionally, each constraint was weighted differently to achieve its purpose without

the loss of image information due to overfitting or overregularization errors. The 3D radial mask subtracted data set (SVIPR) obtained from the pre and post-contrast passes was the primary input for the first two reconstructions (Figure 4.1B-C). The unsubtracted 3D radial data set (VIPR IDEAL Pass 2) was used for the fat/water separation reconstructions (Figure 4.1D).

4.3.3 Single Phase Reconstruction

The SVIPR CS reconstruction utilizes the mask subtracted data from the second pass. The additional sparsity obtained by subtraction is exploited by a compressed sensing (CS) algorithm that includes two steps: 1) data consistency and 2) global thresholding in the spatial domain. A MIP of the entire subtracted volume with temporal information is expected to be used as a tool to quickly visualize the enhancing areas within the breast to determine the absence or potential presence of cancer. The single-slice images with 0.8-mm isotropic resolution are intended to provide morphologic detail for lesion characterization.

4.3.4 Dynamic Reconstruction

The SVIPR STELLR reconstruction, similar to the single-phase reconstruction, uses the mask subtracted post-contrast data. However, before reconstruction, all the half projections, or spokes, are ordered by acquisition time to create 18 volumes, each with 10 seconds of data. The k-space data corresponding to a five-dimensional array (384^3 voxels per spatial volume, 18 time points and 16 coils) is then fed into a **S**patial CS with **Te**mporal **L**ocal **L**ow-**R**ank assistance (STELLR) reconstruction. The dynamic reconstruction algorithm contains three steps: 1) data consistency, 2) global spatial thresholding and 3) local temporal thresholding. In the event of a potentially suspicious finding, the 10 s volumetric temporal resolution allows for perfusion visualization of the entire breast as well as the identified lesion.

4.3.5 Fat/water Reconstruction

The VIPR CS+IDEAL reconstruction uses all the data from the second pass without temporal gating. Each unique k-space volume collected at each echo time is individually reconstructed using a CS algorithm (TEs: 0.18, 1.032, 1.624, 2.32 ms). In this step, just like the single phase reconstruction, CS

takes advantage of the high channel count from the breast coil. A trajectory phase correction is implemented to diminish the blurring effect due to fat off-resonance at 3T[55]. The reconstructed complex images from the four echoes are fed into a modified fat/water decomposition with an Iterative Decomposition with Echo Asymmetry and Least squares estimation (IDEAL)[22] to provide the final set of water and fat image volumes (Fig. 1D). The water images serve as an anatomical map of the breast while the fat images are useful for margin delineation and evaluation of potentially fat containing findings, such as lymph nodes or fat necrosis.

4.3.6 Implementation

Eleven patient volunteers with a previous clinical breast MRI performed for a standard clinical indication and containing an area of breast enhancement which could be well depicted with time-resolved breast MRI gave informed written consent to participate in this IRB-approved, HIPAA compliant study. Imaging was performed on a 3T system (Discovery 750, GE Healthcare, Waukesha, WI) with a 16-channel breast coil (Sentinelle, Invivo, Gainsville, FL) using a 3D radial VIPR IDEAL sequence described above. Clinical images from the standard clinical exam were used to retrospectively generate an abbreviated protocol by eliminating the diffusion weighted images (DWI), T2-weighted images and all post contrast phases following the first post contrast frame, while keeping the T1-weighted (T1-W) fast spoiled gradient echo (FSPGR) without fat-saturation prior to DCE scan and the first two phases of the DCE scan (pre-contrast mask and first post-contrast phase) for use in the abbreviated protocol. Table 4.1 demonstrates the image acquisition parameters for the two sequences used to generate the abbreviated protocol using standard-of-care sequences and research sequence (VIPR IDEAL).

Table 1	Scan Time	TR	Echoes	Resolution	Voxel Vol.	Matrix Size	FOV
T1-W FSPGR w/o Fat Sat.	2:06 min	7.6 ms	1	0.7x0.7x1.4 mm	0.7 mm^3	320x320x142	32 cm
T1-W FSPGR w/ Fat Sat.	2:45 min	7.6 ms	1	0.7x0.7x1.4 mm	0.7 mm^3	320x320x142	32 cm
VIPR IDEAL	3:00 min	3.9 ms	4	0.8x0.8x0.8 mm	0.5 mm^3	384x384x384	32 cm

Table 4.1 *Select imaging parameters used for the standard of care imaging sequences and the VIPR IDEAL acqusition for the abbreviated MR breast protocol comparison. The retrospecticly created abbreviated Cartesian protocol consisted of two sequences: 1) T1-W FSPGR without fat suppression (2:06 mins) and 2) pre and a post-contrast images using a T1-W FSPGR with fat supression (5:30 mins; 7:36 mins total exam time). The VIPR protocol 3) used a single sequence (VIPR IDEAL) with two 3:00 min phases, pre and post-constrast, giving a total scan timeof 6:00 mins.*

Image reconstruction was performed on an AMD-Opteron CPU computer node with 32-cores and 120 GB RAM. The SVIPR CS reconstruction time (16 channels, 384 slices, 42000 spokes) was 2:32 hrs. The VIPR IDEAL+CS reconstruction time (16 channels, 384 slices, 4 echoes, 10500 spokes) was 8:52 hrs. Reconstruction time for the dynamic SVIPR STELLR reconstruction dataset (16 channels, 384 slices, 18 frames, 2333 spokes per frame) was 22:48 hrs.

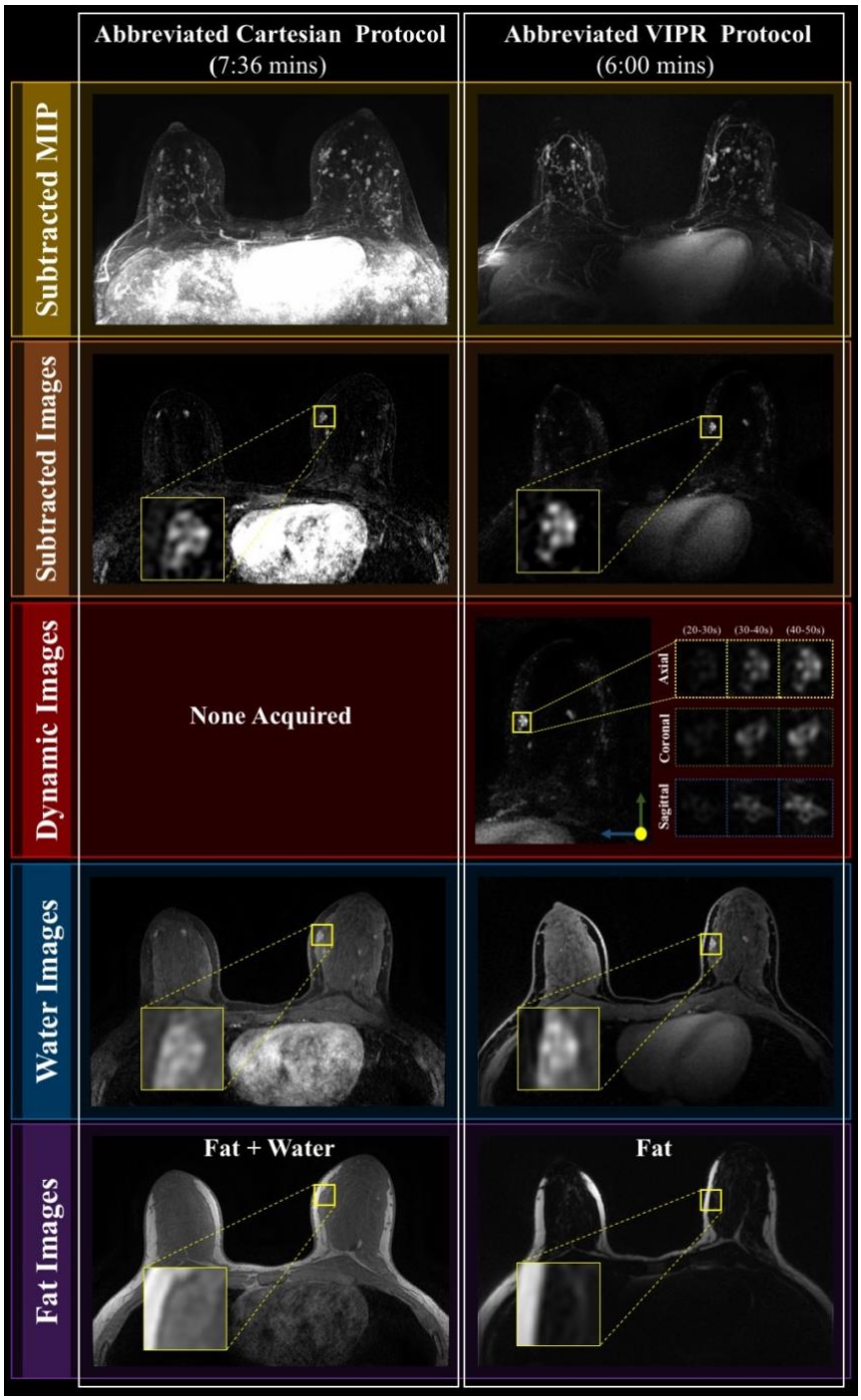

Figure 4.2 *Graphical comparison between the clinical abbreviated protocol (left column) and the VIPR protocol (right column). Starting from the top all possible outputs are included: subtracted MIP, single phase subtracted images, time resolved perfusion images, water images, and fat images. No dynamic imaging is performed as part of the abbreviated Cartesian protocol.*

4.4 RESULTS

4.4.1 Single Phase Reconstruction

A visual comparison between the clinical standard and VIPR protocol MIPs is shown in Figure 3. The three region-of-interest (ROI) magnifications show comparable spatial resolution between morphologic features such as shape, size and structure. Most importantly, potential abnormalities in the breasts can easily be detected by both methods, as shown by the magenta arrows. In addition, the 3D subtraction MIP from the SVIPR CS reconstruction is able to demonstrate enhancement of the heart and some morphology of the liver.

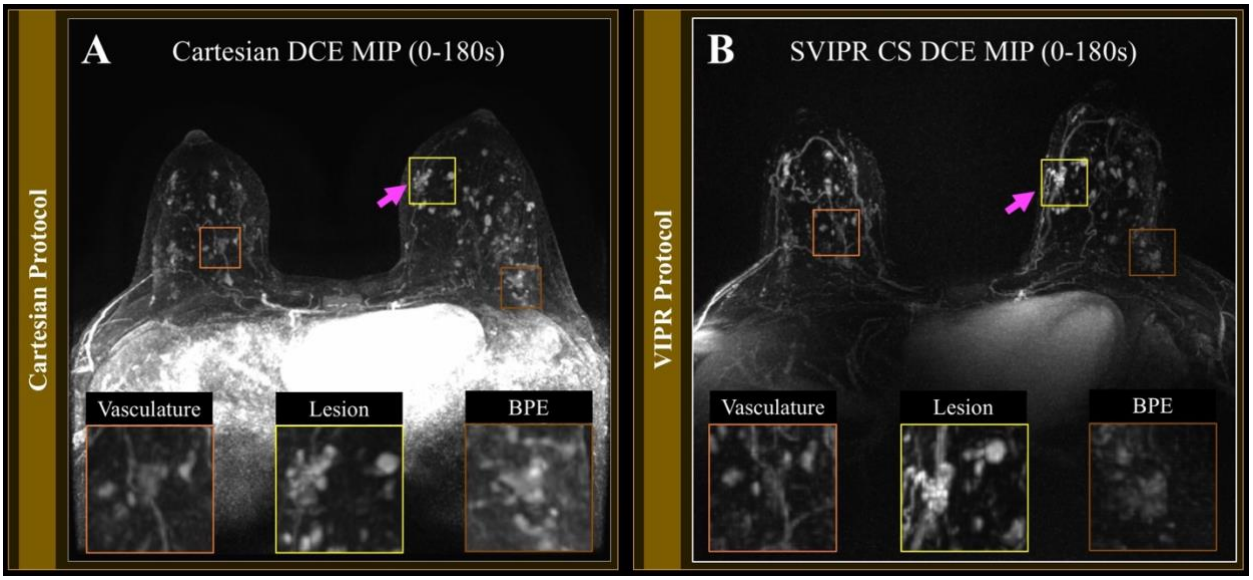

Figure 4.3 *Comparison between MIPs from a clinical protocol (left) and the one obtained from the proposed VIPR protocol. Magnification of three ROIs (orange, yellow and brown) are shown at the bottom of each image. An enhancing feature is indicated by the magenta arrows and yellow ROI.*

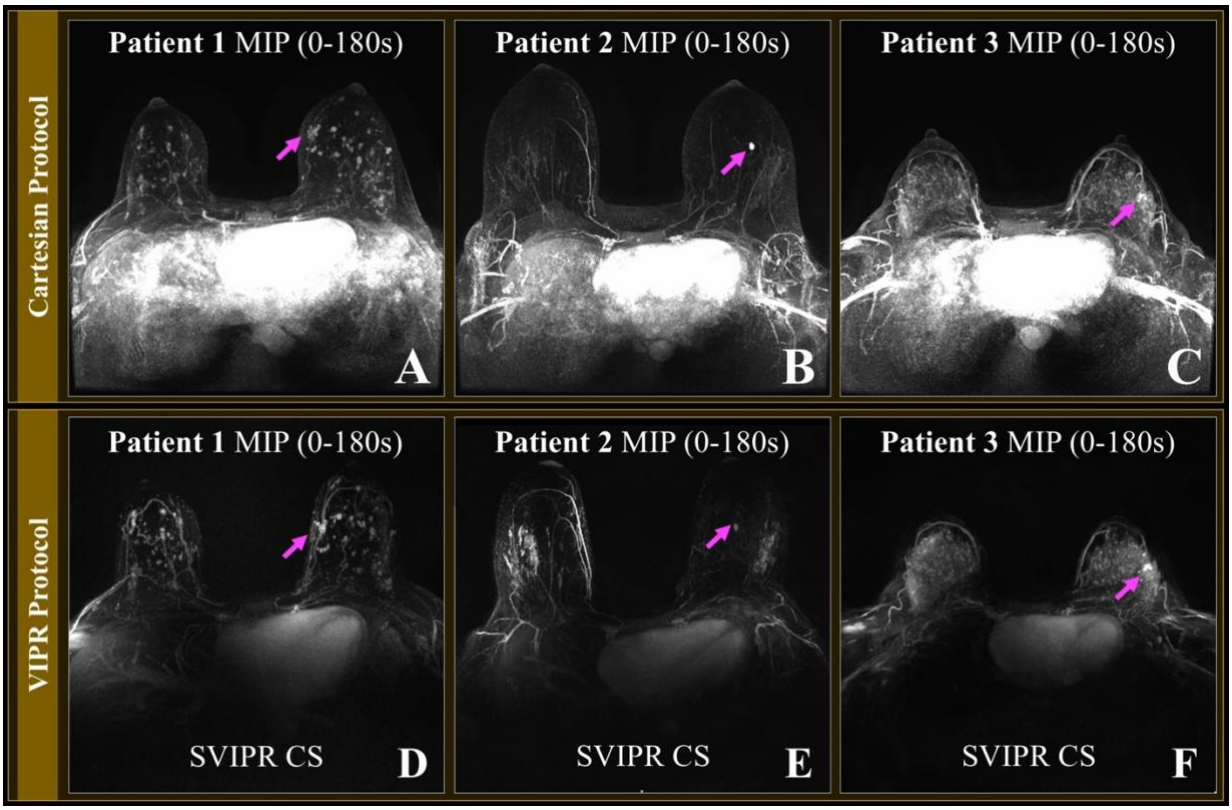

Figure 4.4 *Three subjects with different types of background parenchymal enhancement (BPE): minimal (A, D), mild, (B, E) and marked (C, F) are shown to visualize subtraction reliability at different levels of BPE.* ***Top:*** *MIPs from the first DCE phase obtained from the clinical diagnostic protocols.* ***Bottom:*** *Corresponding MIPs of the complete SVIPR pass using a CS reconstruction. Breast abnormalities are indicated by magenta arrows.*

Protocol comparison between 3D-subtracted MIPs of three different subjects is shown in Figure 4. The SVIPR CS reconstruction is able to maintain high contrast across subjects and no visible artifacts are present due to motion. As a result, high signal can be observed from vasculature system, moderate signal from nipple and chest wall and no signal from skin. Although both protocols provide visualization of the enhancement of the breast vasculature and abnormalities, the MIP from the SVIPR CS reconstruction delivers higher contrast throughout the images. Thus, visualization of areas of abnormal enhancement can be achieved without oversaturation of the heart and posterior anatomy.

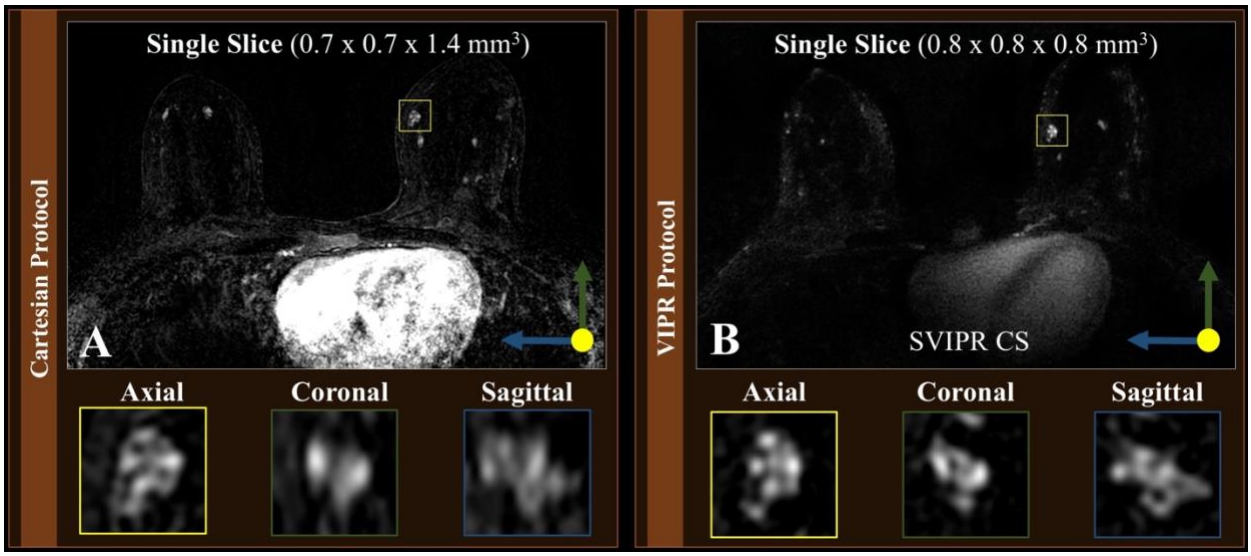

Figure 4.5 *Single slice comparison.* ***Left:*** *subtracted image obtained from first enhancing phase.* ***Right:*** *image from the mask subtracted data set using compressed sensing (SVIPR CS) over the entire 3 minutes pass. Magnification of enhancing feature in three ortogonal axis is shown at the bottom.*

Figure 4.5 displays a comparison between single slices of the clinical and VIPR protocol. Sagittal renderings from both techniques are able to display the complex pattern of the focal area of enhancement (yellow box). However, the higher isotropic spatial resolution delivered by the SVIPR CS reconstruction can be appreciated in the coronal and sagittal reconstructions. The nearly double increase in spatial resolution provides improved visualization of the irregular shape and the heterogeneous enhancement pattern. In addition, no blurring or partial voluming errors are present in sagittal or coronal views due to differences between in plane resolution and slice thickness.

4.4.2 Dynamic Reconstruction

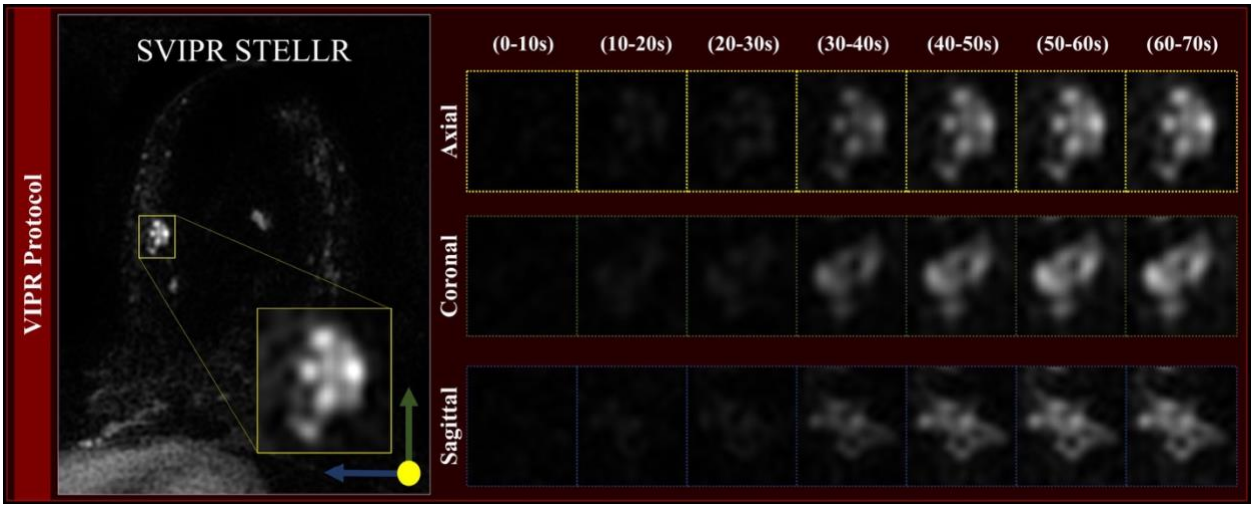

Figure 4.6 *Demonstration of the dynamic image reconstruction capabilities using the SVIPR STELLR approach over one ROI and displayed on the orthogonal axes. The 10-second temporal resolution allows for visualization of the uptake phase. The isotropic resolution delivers high spatial resolution and thus the opportunity to observe the lesion in any conventional axis without image distortion. Complex spatial and temporal behavior is observed within the first 60 seconds of enhancement.*

Visualization of the lesion perfusion is demonstrated by the proposed STELLR reconstruction of the SVIPR data set through inspection of sequential frames generated at 10 s intervals (Fig. 4.6). Lesion temporal heterogeneity is captured while preserving morphologic features (yellow box). Despite a significant data undersampling rate (R), R=45 at the edge of k-space, the temporal performance of SVIPR STELLR with a 10-s volumetric frame rate is demonstrated by the visualization of the irregular shape and varied onset of contrast enhancement within the lesion using three orthogonal planes.

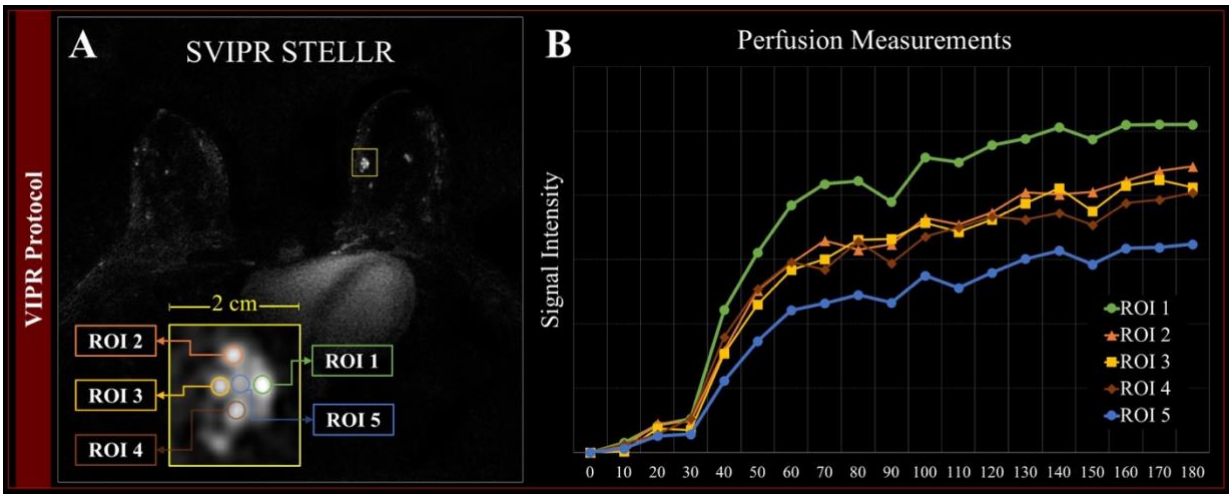

Figure 4.7 *SVIPR STELLR reconstruction of a volunteer patient with a 1.8-cm focal area of enhancement. B) Time curves of the average signal intensity for five regions of interest within the focal area of enhancement are shown during the first 180 seconds of perfusion at 10 sec intervals. More rapid enhancement is seen in the most lateral region of the feature (ROI 1) while the central region (ROI 5) displays a slower uptake rate.*

Figure 4.7 demonstrates the capabilities of the proposed dynamic reconstruction. In Figure 7A, a single slice from a volumetric frame is offered as a point of reference. Five ROIs from within the lesion are chosen to measure signal intensities as a function of time. In Figure 7B, comparison of the enhancement curves of the most lateral portion (ROI 1) and central area (ROI 5) of the lesion at 10 second intervals demonstrates that the lateral portion enhances more rapidly and more intensely.

4.4.3 Fat/water Reconstruction

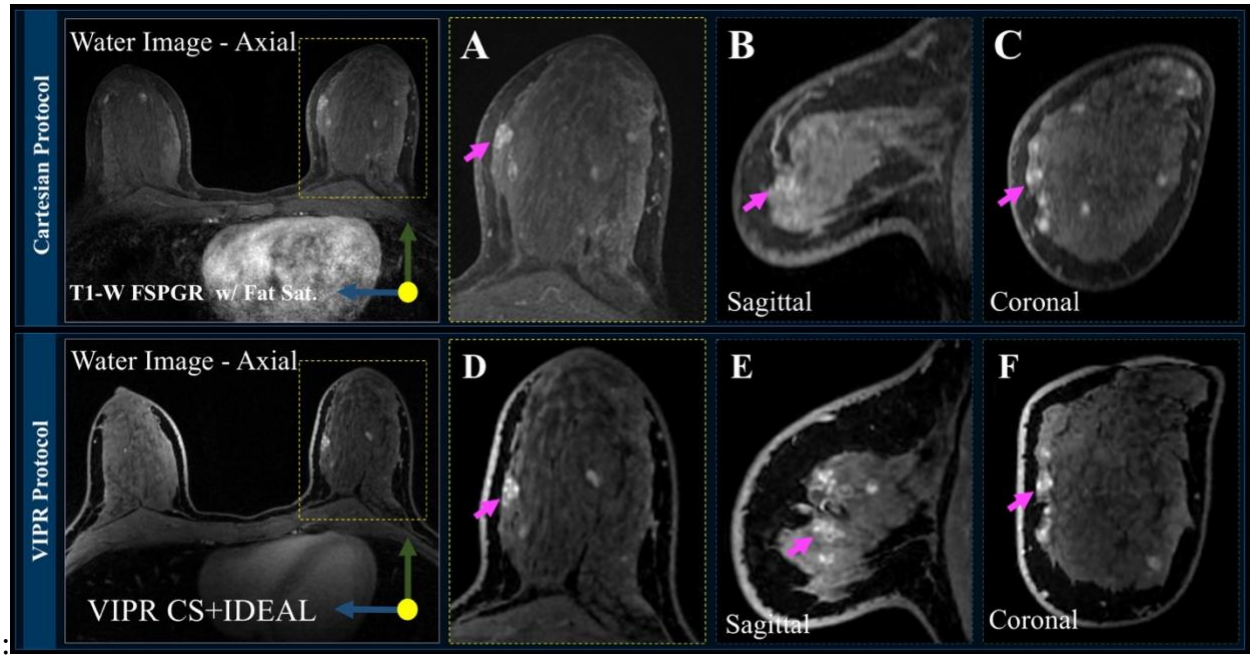

Figure 4.8 *Water image comparison between methods.* ***Top:*** *water images from the prost-contrast phase using a T1-W with intermitten chemical fat saturation pulse.* ***Bottom:*** *corresponding water images obtained from the prost-contrast pass (VIPR pass 2) in combination with compressed sensing and fat-water decomposition (VIPR CS+IDEAL). Renderings of sagittal (B, E) and coronal (C, F) views are also shown. The enhancing feature is indicated throughout (magenta arrows).*

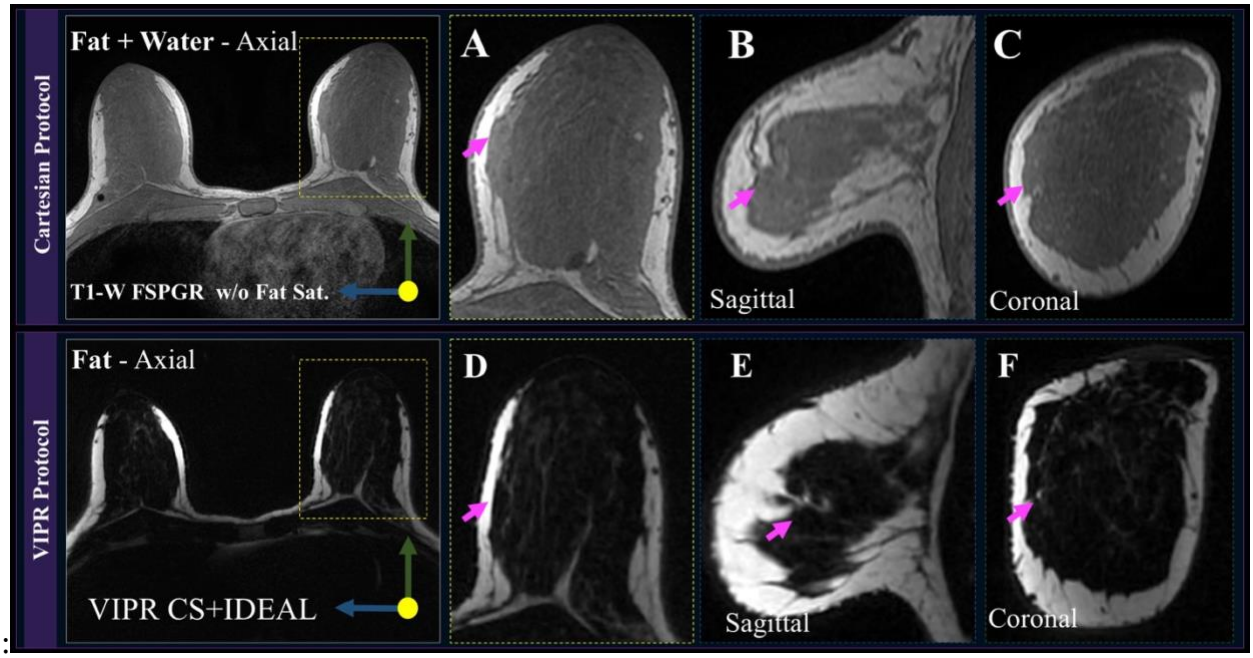

Figure 4.9 *Fat image comparison between methods.* ***Top:*** *T1 weighted images without fat suppression from the pre-contrast phase.* ***Bottom:*** *Corresponding fat images obtained from the post-contrast pass (VIPR pass 2) in combination with CS and IDEAL. Renderings of sagittal (B, E) and coronal (C, F)*

views are also shown. The expected location of the enhancing feature is indicated throughout (magenta arrows).

The post-contrast portion of the study, VIPR IDEAL pass 2 (Fig 4.8A), was reconstructed using CS+IDEAL to produce static water images that are comparable with the prost-contrast images from the clinical protocol (Fig. 4.8). Our proposed 4-point Dixon method (IDEAL) is able to suppress all fat, while the clinical images with intermittent fat saturation exhibit gray contrast in fatty areas. Multiple high contrast areas can be appreciated over the inner quadrants in the sagittal and coronal renderings. Figure 4.9 provides a comparison between fat only images and pre-contrast water images without fat-saturation.

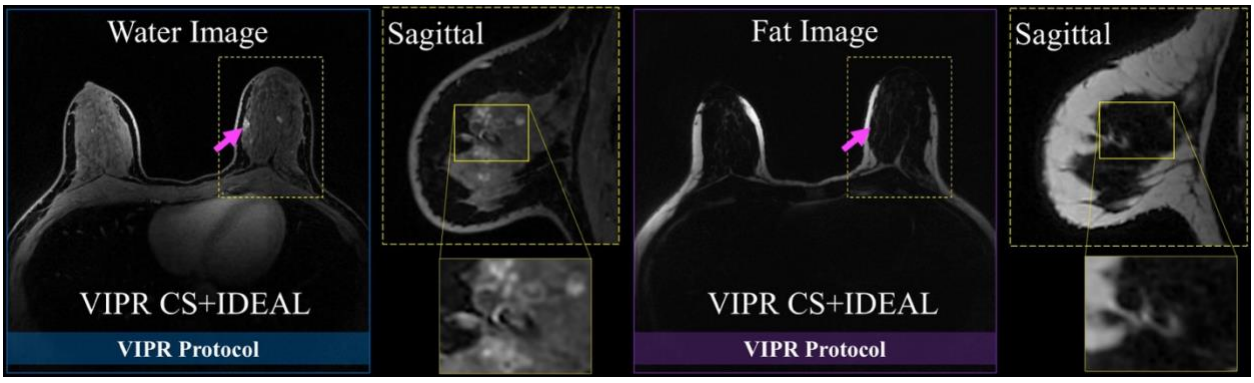

Figure 4.10 *Demonstration of fa/water reconstruction (VIPR CS+IDEAL) in the prescribed axial plane and the reformatted sagittal plane using the post-contrast pass (0-180s) in both water (left) and fat (right) images. Enhancing feature, identified by magenta arrows, are shown with the proposed method.*

As previously described, the entire pass of the enhanced VIPR CS+IDEAL can be reconstructed without mask subtraction to depict the post-contrast pass (Fig. 9). Water images depict high level of morphologic detail in both planes of a known breast cancer, including margin and irregular shape, as a result of the 0.8-mm isotropic resolution. Fat images provide a negative contrast reference of the architecture of the breast.

4.5 DISCUSSION

Over the last few years, abbreviated breast MRI protocols have received attention due to their potential to increase the value of MRI for breast cancer screening without compromising diagnostic accuracy by reducing scan time, reducing interpretation time, decreasing costs and increasing patient throughput. Additionally, shortening protocols may potentially increase the number of patients recommended to undergo breast MRI for screening. Standardizing requirements for these protocols is an active area of research. However, due to the clinical importance of spatial resolution given the clinical importance of lesion morphologic characterization, most of the current approaches allow for limited or no perfusion analysis. We have presented a method that uses a 3D radial acquisition and three constrained reconstruction schemes to provide morphologic and perfusion information from a single scan six-minute exam. The proposed abbreviated VIPR breast MRI protocol is able to preserve high spatial resolution imaging with a marked improvement in temporal resolution at a short overall scan time.

When comparing both protocols, Cartesian and VIPR, some additional advantages from our proposed method can be observed. First, radial trajectories are inherently less susceptible to motion artifacts[52]. Consequently, VIPR has the potential for improved subtraction with less potential for motion artifacts (Fig. 4). Second, the four-point Dixon method provides more uniform fat suppression than a frequency selective fat saturation scheme. Third, additional perfusion information obtained from the STELLR reconstruction can be used for early-phase enhancement evaluation, including semi-quantitative measurements like TTP or wash-in curves to determine what enhances first to increase diagnostic confidence. Ultimately, our methodology is able to provide a high throughput abbreviated protocol producing more information within a single scan than a Cartesian approach.

MIPs of the entire post-contrast data set (180 sec) with mask subtraction (Fig. 1A-B) offer a rapid overview of the regions of increased permeability, similar to the capability shown in Kuhl's rapid screening technique[7]. The MIP generated from the SVIPR CS reconstruction is expected to be utilized

as the primary tool to quickly establish the absence of cancer (Fig. 4.3-4.4). Furthermore, the single slice mask subtracted images (Fig. 4.5) with 0.8-mm isotropic resolution provide detailed morphologic information to aid during the interpretation process. In case of a finding, the perfusion information from the STELLR reconstruction (Fig. 4.6-4.7) can be used for simultaneous assessment of the extent of disease, locating satellite lesions and assisting with staging (multifocal, multicentric, and bilateral disease). In addition, the water images from the VIPR CS+IDEAL reconstruction (Fig. 4.8-4.9A) can be used to further characterize the pathology while the negative contrast from the fat images (Fig. 4.9B) provides an architectural map of the breast that can be used to delineate margins or even help distinguishing fat necrosis from necrotic tumor[114].

The proposed VIPR protocol is shown here to be a viable alternative to further understand the impact of abbreviated protocols in clinical practice. Nevertheless, a larger clinical trial is required to collect a statistically relevant pool of lesions to determine the diagnostic performance of the VIPR protocol and its image quality in the clinical practice. Such studies could potentially answer whether the proposed abbreviated protocol is able to maintain or improve sensitivity and specificity. Our study has some limitations. First, given the limited sample size, diagnostic accuracy was not compared between protocols and needs to be evaluated in the larger follow-up clinical trial. Second, currently no major MRI hardware vendor in the USA offers non-Cartesian MRI for the breast. Thus, clinical implementation of our technique would require the development of a workflow platform that is compatible with the current clinical standards, including the adoption of graphics processing units (GPUs) to reduce the long reconstruction periods.

4.6 CONCLUSION

We demonstrated a comparison between an abbreviated breast MRI protocol using the current standard clinical sequences and a single 6-minute protocol with 3D radial trajectory for a high throughput abbreviated breast MRI protocol. A three-reconstruction methodology is used to extract all the morphological and kinetic information within the first 180 seconds after a contrast injection. First, a single phase post-contrast reconstruction that serves as the primary tool for the screening. Second, a 10-s volumetric frame rate with 0.8-mm isotropic spatial resolution to characterize lesion morphology and perfusion pattern. Third, a fat/water reconstruction is used to characterize breast architecture. A larger clinical study is required to validate the clinical impact of this new methodology in the screening realm.

Chapter V FUTURE WORK

5 SUMMARY AND FUTURE WORK

5.1 Summary

This thesis represents technical advances and validation for a 3D radial MRI abbreviated protocol for cancer screening and a platform for ultra-fast imaging of the breast. The contributions of this dissertation can be summarized as follows:

5.1.1 3D VIPR Acquisition

I modified a 3D radial VIPR IDEAL trajectory to optimize its characteristics and make it equipped for a high throughput methodology. Furthermore, I chose four unique echo times that allow for robust fat/water separation in a FOV large enough to accommodate both breasts without additional sampling from the DCE exam. The adjustment to the acquisition pattern of the 3D radial sequence in combination with a pseudo-random ordering of the acquired spokes produced the required incoherent undersampling artifact for CS implementations. I took advantage of high count breast coil arrays (16 channels) and very high field magnetic strength, 3T, to improve acquisition performance. The achieved short TR, 4.2 ms, allows for frequent sampling at the center of k-space which makes the modified VIPR IDEAL trajectory a suitable alternative for a dynamic reconstruction.

5.1.2 Constrained Reconstructions

I designed three reconstructions that take full advantage of the VIPR IDEAL trajectory with the help of little to no pre-processing. First, the STELLR reconstruction, which is able to exploit the temporal redundancy through an LLR temporal constraint while a global CS spatial constraint takes advantage of the additional spatial sparsity obtained by mask-subtracted dynamic data (SVIPR). Second, a CS reconstruction with no temporal constraint (SVIPR CS) that uses all the mask subtracted data as a single time-point to deliver a rapid visualization of the morphology of the breast with a fraction of the computing time in comparison to the SVIPR STELLR methodology. Third, a fat/water separation

reconstruction (VIPR CS+IDEAL) that utilizes the unique spectral information of each reconstructed echo using a traditional CS reconstruction to produce robust fat and water images—an output that typically would require additional scanning time.

5.1.3 Abbreviated Breast Screening Protocol

I developed an abbreviated protocol that is able to dramatically reduce table time at the MRI system by up to a factor of five, from 30 minutes to 6 minutes, while providing comparable information from a full diagnostic protocol for a breast cancer screening task. Such advances were achieved by using the technology already mentioned above and by adopting an early enhancement DCE methodology. The SVIPR CS reconstruction can be utilized to determine the absence or potential presence of cancer through a MIP and morphology can be characterized using the single slice images. In case of a finding, SVIPR STELLR delivers high spatiotemporal resolution of the first 180 seconds after contrast injection to help stage the finding and/or increase interpretation confidence. Water images of the post-contrast phase are used to provide an anatomical map of the breast. Fat images can be used to delineate lesion margins, structure, differentiate fat necrosis and visualize breast notes.

5.1.4 Digital Phantom Validation

I adapted and employed an in-silico simulation with realistic features as a reasonable validation strategy. I showed that the coadjuvant combination between pulse sequence and reconstruction is required to deliver high spatiotemporal resolution. I presented evidence that STELLR is able to deliver 0.8-mm isotropic resolution and 10-second temporal resolution with a R=45 undersampled rate at the edge of each volumetric time point. In addition, I demonstrated how the LLR component is able to exploit the data redundancy across time points without compromising the temporal or spatial integrity of each lesion render. Consequently, STELLR shows to be a robust reconstruction despite lesion shape, size or enhancing pattern. Furthermore, during the digital phantom validation I illustrated the need of

fast imaging during the wash-in portion of the enhancement phase where the signal intensity is changing more rapidly.

5.1.5 Clinical Comparison

I compared the ability of a 3D radial abbreviated protocol to deliver the morphologic information of the breast with the addition of perfusion measurements within a single scan against an abbreviated breast protocol using standard of care sequences. The additional outputs, perfusion images and fat images, from the VIPR protocol in comparison to the Cartesian protocol do not require an increase in scanning time. The water images from the four-point Dixon reconstruction (VIPR CS+IDEAL) deliver a more uniform fat suppression than the Cartesian approach. The 0.8-mm isotropic resolution from all reconstructions allows for visualization of the morphology in any conventional axis without any spatial distortion or blurring. The developed abbreviated VIPR protocol is able to maximize the information that can be derived from an abbreviated protocol.

5.2 Future work

5.2.1 Abbreviated Breast Screening Protocol

Although the quantitative analysis using a digital phantom and in vivo experiments provides an insightful understanding of the spatial and temporal capabilities of the abbreviated VIPR protocol, further validation is required to understand its clinical performance. A large clinical trial with an adequate pool of lesion cases is required to minimize the risk of underestimating the variability and therefore obtaining an under-powered confirmation of our method's performance in clinical practice. A reader study with a statistically significant group of cases is crucial to understand how the imaging performance of our method could improve routine interpretation.

5.2.2 Non-Cartesian Fat/water separation

The VIPR IDEAL trajectory was bounded by the high acquisition performance demands of the STELLR reconstruction. However, an independent trajectory that is not intended to be used for a dynamic reconstruction can easily be modified to accommodate a better echo selection. Moreover, longer TEs can be used to add T2* into the model and generate R2* maps of the breast. Furthermore, a smaller tip angle can also be used during a static scan to reduce T_1 bias to improve fat fraction decomposition at a pixel level.

5.2.3 STELLR Dynamic reconstruction

The VIPR STELLR methodology provides a platform for high throughput imaging that can be adapted to applications outside of breast imaging detection. Similar to the VIPR CS+IDEAL reconstruction, if SVIPR STELLR is not constrained by meeting the requirements of the TEs for IDEAL, a more efficient sampling scheme can be developed with a single shorter TR that nearly doubles acquisition performance. Those gains would improve the temporal resolution of the STELLR reconstruction. Furthermore, the addition of more dynamic phases could potentially allow STELLR to provide an imaging alternative for pharmacokinetic studies. In any of these modifications, a digital phantom can be utilized to optimize the acquisition and/or reconstruction parameters.

6 REFERENCES

1. *Breast Cancer Facts and Figures 2017-2018.* Atlanta, GA: American Cancer Society; 2018 2018.
2. DeMartini W, Lehman C. A review of current evidence-based clinical applications for breast magnetic resonance imaging. *Top Magn Reson Imaging.* 2008;19(3):143-150.
3. Mehnati P, Tirtash MJ. Comparative Efficacy of Four Imaging Instruments for Breast Cancer Screening. *Asian Pac J Cancer Prev.* 2015;16(15):6177-6186.
4. Quinn EM, Coveney AP, Redmond HP. Use of magnetic resonance imaging in detection of breast cancer recurrence: a systematic review. *Ann Surg Oncol.* 2012;19(9):3035-3041.
5. Wang LC. MR Imaging: Future Imaging Techniques. *Radiol Clin North Am.* 2017;55(3):553-577.
6. Berg WA, Zhang Z, Lehrer D, et al. Detection of breast cancer with addition of annual screening ultrasound or a single screening MRI to mammography in women with elevated breast cancer risk. *JAMA.* 2012;307(13):1394-1404.
7. Kuhl CK, Schrading S, Strobel K, Schild HH, Hilgers RD, Bieling HB. Abbreviated breast magnetic resonance imaging (MRI): first postcontrast subtracted images and maximum-intensity projection-a novel approach to breast cancer screening with MRI. *J Clin Oncol.* 2014;32(22):2304-2310.
8. Abe H, Mori N, Tsuchiya K, et al. Kinetic Analysis of the Ultra Early Phase on Breast MRI: Comparison between Benign and Malignant Lesions using Ultrafast Dynamic Contrast Enhanced MRI. Paper presented at: Radiological Society of North America 2015 Scientific Assembly and Annual Meeting; November 29 - December 4, 2015; Chicago IL.
9. Pineda F, Tsuchiya K, Abe H, et al. Characterization of Breast Lesion Kinetics with Accelerated DCE-MRI Using Conventional Sampling Methods. Paper presented at: Radiological Society of North America 2015 Scientific Assembly and Annual Meeting; November 29 - December 4, 2015, 2015; Chicago IL.
10. Damadian R, Zaner K, Hor D, DiMaio T, Minkoff L, Goldsmith M. Nuclear magnetic resonance as a new tool in cancer research: human tumors by NMR. *Ann N Y Acad Sci.* 1973;222:1048-1076.
11. Heywang SH, Hahn D, Schmidt H, et al. MR imaging of the breast using gadolinium-DTPA. *J Comput Assist Tomogr.* 1986;10(2):199-204.
12. Stelling CB, Wang PC, Lieber A, Mattingly SS, Griffen WO, Powell DE. Prototype coil for magnetic resonance imaging of the female breast. Work in progress. *Radiology.* 1985;154(2):457-462.
13. Gold LS, Klein G, Carr L, Kessler L, Sullivan SD. The emergence of diagnostic imaging technologies in breast cancer: discovery, regulatory approval, reimbursement, and adoption in clinical guidelines. *Cancer Imaging.* 2012;12:13-24.
14. Morris EA, Comstock CE, Lee CH, et al. ACR BIRADS Magnetic Resonance Imaging. In: *ACR BIRADS Atlas, Breast Imaging Reporting and Data System.* Reston, VA: American College of Radiology; 2013.
15. Gutierrez RL, Strigel RM, Partridge SC, et al. Dynamic breast MRI: does lower temporal resolution negatively affect clinical kinetic analysis? *AJR American journal of roentgenology.* 2012;199(3):703-708.
16. Wang LC, DeMartini WB, Partridge SC, Peacock S, Lehman CD. MRI-detected suspicious breast lesions: predictive values of kinetic features measured by computer-aided evaluation. *AJR Am J Roentgenol.* 2009;193(3):826-831.
17. Huang W, Li X, Chen Y, et al. Variations of dynamic contrast-enhanced magnetic resonance imaging in evaluation of breast cancer therapy response: a multicenter data analysis challenge. *Transl Oncol.* 2014;7(1):153-166.
18. Lustig M, Donoho D, Pauly JM. Sparse MRI: The application of compressed sensing for rapid MR imaging. *Magn Reson Med.* 2007;58(6):1182-1195.
19. Jimenez JE, Johnson KM, Henze Bancroft LC, et al. 10 Second Temporal Resolution of Early Enhancement Visualization: Framework for Fast Breast MRI Screening. Paper presented at: ISMRM 20172017; Honolulu, USA.

20. Cai J-F, Candès EJ, Shen Z. A Singular Value Thresholding Algorithm for Matrix Completion. *SIAM Journal on Optimization.* 2010;20(4):1956-1982.
21. Dixon WT. Simple proton spectroscopic imaging. *Radiology.* 1984;153(1):189-194.
22. Reeder SB, Pineda AR, Wen Z, et al. Iterative decomposition of water and fat with echo asymmetry and least-squares estimation (IDEAL): application with fast spin-echo imaging. *Magn Reson Med.* 2005;54(3):636-644.
23. Moran CJ, Brodsky EK, Bancroft LH, et al. High-resolution 3D radial bSSFP with IDEAL. *Magn Reson Med.* 2014;71(1):95-104.
24. Kuhl C. The current status of breast MR imaging. Part I. Choice of technique, image interpretation, diagnostic accuracy, and transfer to clinical practice. *Radiology.* 2007;244(2):356-378.
25. Lehman CD, Isaacs C, Schnall MD, et al. Cancer yield of mammography, MR, and US in high-risk women: prospective multi-institution breast cancer screening study. *Radiology.* 2007;244(2):381-388.
26. Sardanelli F, Boetes C, Borisch B, et al. Magnetic resonance imaging of the breast: recommendations from the EUSOMA working group. *Eur J Cancer.* 2010;46(8):1296-1316.
27. Lohrke J, Frenzel T, Endrikat J, et al. 25 Years of Contrast-Enhanced MRI: Developments, Current Challenges and Future Perspectives. *Adv Ther.* 2016;33(1):1-28.
28. Berg WA, Blume JD, Cormack JB, et al. Combined screening with ultrasound and mammography vs mammography alone in women at elevated risk of breast cancer. *JAMA.* 2008;299(18):2151-2163.
29. Mango VL, Morris EA, David Dershaw D, et al. Abbreviated protocol for breast MRI: are multiple sequences needed for cancer detection? *Eur J Radiol.* 2015;84(1):65-70.
30. Kuhl CK. High-Throughput: The 5 Minute MR Scan (Breast Imaging). Paper presented at: ISMRM 2016; Singapore.
31. Moon M, Cornfeld D, Weinreb J. Dynamic contrast-enhanced breast MR imaging. *Magn Reson Imaging Clin N Am.* 2009;17(2):351-362.
32. Kuhl CK, Schild HH, Morakkabati N. Dynamic bilateral contrast-enhanced MR imaging of the breast: trade-off between spatial and temporal resolution. *Radiology.* 2005;236(3):789-800.
33. Jansen SA, Fan X, Karczmar GS, Abe H, Schmidt RA, Newstead GM. Differentiation between benign and malignant breast lesions detected by bilateral dynamic contrast-enhanced MRI: a sensitivity and specificity study. *Magnetic resonance in medicine : official journal of the Society of Magnetic Resonance in Medicine / Society of Magnetic Resonance in Medicine.* 2008;59(4):747-754.
34. Kuhl CK. Current status of breast MR imaging. Part 2. Clinical applications. *Radiology.* 2007;244(3):672-691.
35. Han M, Daniel BL, Hargreaves BA. Accelerated bilateral dynamic contrast-enhanced 3D spiral breast MRI using TSENSE. *J Magn Reson Imaging.* 2008;28(6):1425-1434.
36. Feng L, Grimm R, Block KT, et al. Golden-angle radial sparse parallel MRI: combination of compressed sensing, parallel imaging, and golden-angle radial sampling for fast and flexible dynamic volumetric MRI. *Magnetic resonance in medicine : official journal of the Society of Magnetic Resonance in Medicine / Society of Magnetic Resonance in Medicine.* 2014;72(3):707-717.
37. Korosec FR, Frayne R, Grist TM, Mistretta CA. Time-resolved contrast-enhanced 3D MR angiography. *Magnetic resonance in medicine : official journal of the Society of Magnetic Resonance in Medicine / Society of Magnetic Resonance in Medicine.* 1996;36(3):345-351.
38. Ramsay E, Causer P, Hill K, Plewes D. Adaptive bilateral breast MRI using projection reconstruction time-resolved imaging of contrast kinetics. *J Magn Reson Imaging.* 2006;24(3):617-624.
39. Dougherty L, Isaac G, Rosen MA, et al. High frame-rate simultaneous bilateral breast DCE-MRI. *Magnetic resonance in medicine : official journal of the Society of Magnetic Resonance in Medicine / Society of Magnetic Resonance in Medicine.* 2007;57(1):220-225.
40. Saranathan M, Rettmann D, Hargreaves BA, Lipson J, Daniel BL. High Spatio-temporal Resoltuion breast dynamic contrast enhanced MRI at 3T. Paper presented at: Proceedings of the 20th annual Meeting of ISMRM2012 Melbourne, Australia.
41. Henderson E, Rutt BK, Lee TY. Temporal sampling requirements for the tracer kinetics modeling of breast disease. *Magn Reson Imaging.* 1998;16(9):1057-1073.

42. Feng L, Axel L, Chandarana H, Block KT, Sodickson DK, Otazo R. XD-GRASP: Golden-angle radial MRI with reconstruction of extra motion-state dimensions using compressed sensing. *Magn Reson Med.* 2016;75(2):775-788.
43. Benkert T, Feng L, Sodickson DK, Chandarana H, Block KT. Free-breathing volumetric fat/water separation by combining radial sampling, compressed sensing, and parallel imaging. *Magn Reson Med.* 2016.
44. Schnall MD, Ikeda DM. Lesion Diagnosis Working Group report. *J Magn Reson Imaging.* 1999;10(6):982-990.
45. Jim J, Tao L. Dynamic MRI with compressed sensing imaging using temporal correlations. Paper presented at: 2008 5th IEEE International Symposium on Biomedical Imaging: From Nano to Macro; 14-17 May 2008, 2008.
46. Wang H, Miao Y, Zhou K, et al. Feasibility of high temporal resolution breast DCE-MRI using compressed sensing theory. *Med Phys.* 2010;37(9):4971-4981.
47. Chen L, Schabel MC, DiBella EV. Reconstruction of dynamic contrast enhanced magnetic resonance imaging of the breast with temporal constraints. *Magn Reson Imaging.* 2010;28(5):637-645.
48. Adluru G, Tasdizen T, Schabel MC, DiBella EV. Reconstruction of 3D dynamic contrast-enhanced magnetic resonance imaging using nonlocal means. *J Magn Reson Imaging.* 2010;32(5):1217-1227.
49. Smith DS, Welch EB, Li X, et al. Quantitative effects of using compressed sensing in dynamic contrast enhanced MRI. *Physics in Medicine and Biology.* 2011;56(15):4933-4946.
50. Block WF, Barger AV, Mistretta CA. Vastly Undersampled Isotropic Projection Imaging. International Society for Magnetic Resonance in Medicine; 2000; Denver, Colorado, USA.
51. Lu A, Brodsky E, Grist TM, Block WF. Rapid fat-suppressed isotropic steady-state free precession imaging using true 3D multiple-half-echo projection reconstruction. *Magn Reson Med.* 2005;53(3):692-699.
52. Chan RW, Ramsay EA, Cheung EY, Plewes DB. The influence of radial undersampling schemes on compressed sensing reconstruction in breast MRI. *Magn Reson Med.* 2012;67(2):363-377.
53. Barger AV, Block WF, Toropov Y, Grist TM, Mistretta CA. Time-resolved contrast-enhanced imaging with isotropic resolution and broad coverage using an undersampled 3D projection trajectory. *Magn Reson Med.* 2002;48(2):297-305.
54. Reeder SB, McKenzie CA, Pineda AR, et al. Water-fat separation with IDEAL gradient-echo imaging. *J Magn Reson Imaging.* 2007;25(3):644-652.
55. Brodsky EK, Holmes JH, Yu H, Reeder SB. Generalized k-space decomposition with chemical shift correction for non-Cartesian water-fat imaging. *Magn Reson Med.* 2008;59(5):1151-1164.
56. Kuperman VY, Alley MT. Differentiation between the effects of T1 and T2* shortening in contrast-enhanced MRI of the breast. *J Magn Reson Imaging.* 1999;9(2):172-176.
57. Ramadan S, Mulkern RV. Comment on ADC reductions in postcontrast breast tumors. *J Magn Reson Imaging.* 2010;31(1):262; author reply 263-264.
58. Pineda AR, Reeder SB, Wen Z, Pelc NJ. Cramer-Rao bounds for three-point decomposition of water and fat. *Magn Reson Med.* 2005;54(3):625-635.
59. Majumdar A, Ward RK. Exploiting rank deficiency and transform domain sparsity for MR image reconstruction. *Magn Reson Imaging.* 2012;30(1):9-18.
60. Zhang T, Alley M, Lustig M, Li X, Pauly J, Vasanawala S. Fast 3D DCE-MRI with sparsity and low-rank enhanced SPIRiT (SLR-SPIRiT). Paper presented at: Proceedings of the 21st Annual Meeting of ISMRM, Salt Lake City, Utah, USA2013.
61. Otazo R, Candes E, Sodickson DK. Low-rank plus sparse matrix decomposition for accelerated dynamic MRI with separation of background and dynamic components. *Magn Reson Med.* 2015;73(3):1125-1136.
62. Trzasko J, Manduca A, Borisch E. Local versus global low-rank promotion in dynamic MRI series reconstruction. Paper presented at: Proc. Int. Symp. Magn. Reson. Med2011.
63. Zhang T, Pauly JM, Levesque IR. Accelerating parameter mapping with a locally low rank constraint. *Magnetic resonance in medicine : official journal of the Society of Magnetic Resonance in Medicine / Society of Magnetic Resonance in Medicine.* 2015;73(2):655-661.

64. Zhang T, Cheng JY, Potnick AG, et al. Fast pediatric 3D free-breathing abdominal dynamic contrast enhanced MRI with high spatiotemporal resolution. *Journal of Magnetic Resonance Imaging.* 2015;41(2):460-473.
65. Lugauer F, Nickel D, Wetzl J, Kiefer B, Hornegger J, Maier A. Accelerating multi-echo water-fat MRI with a joint locally low-rank and spatial sparsity-promoting reconstruction. *MAGMA.* 2017;30(2):189-202.
66. Liang ZP. Spatiotemporal imaging with partially separable functions. *I S Biomed Imaging.* 2007:988-991.
67. McGivney DF, Pierre E, Ma D, et al. SVD compression for magnetic resonance fingerprinting in the time domain. *IEEE Trans Med Imaging.* 2014;33(12):2311-2322.
68. Pruessmann KP, Weiger M, Scheidegger MB, Boesiger P. SENSE: sensitivity encoding for fast MRI. *Magnetic resonance in medicine : official journal of the Society of Magnetic Resonance in Medicine / Society of Magnetic Resonance in Medicine.* 1999;42(5):952-962.
69. Jimenez JE, Henze Bancroft LC, Strigel MR, Johnson KM, Reeder SB, Block WF. Non-Cartesian Compressed Sensing with Fat/Water Decomposition: Feasibility Study for High Performance Breast DCE-MRI. Paper presented at: ISMRM 20152015; Toronto, CA.
70. Wright KL, Hamilton JI, Griswold MA, Gulani V, Seiberlich N. Non-Cartesian parallel imaging reconstruction. *J Magn Reson Imaging.* 2014;40(5):1022-1040.
71. Griswold MA, Jakob PM, Nittka M, Goldfarb JW, Haase A. Partially parallel imaging with localized sensitivities (PILS). *Magn Reson Med.* 2000;44(4):602-609.
72. Wang Z, Bovik AC, Sheikh HR, Simoncelli EP. Image quality assessment: from error visibility to structural similarity. *IEEE Trans Image Process.* 2004;13(4):600-612.
73. Levine E, Daniel B, Vasanawala S, Hargreaves B, Saranathan M. 3D Cartesian MRI with compressed sensing and variable view sharing using complementary poisson-disc sampling. *Magn Reson Med.* 2016.
74. Graff CG, Sidky EY. Compressive sensing in medical imaging. *Appl Opt.* 2015;54(8):C23-44.
75. Zhao B, Haldar JP, Brinegar C, Liang ZP. Low rank matrix recovery for real-time cardiac MRI. Paper presented at: 2010 IEEE International Symposium on Biomedical Imaging: From Nano to Macro; 14-17 April 2010, 2010.
76. Haldar JP, Liang ZP. Low-rank approximations for dynamic imaging. Paper presented at: 2011 IEEE International Symposium on Biomedical Imaging: From Nano to Macro; March 30 2011-April 2 2011, 2011.
77. Jimenez JE, Johnson KM, Henze Bancroft LC, et al. High Performance Volumetric 3T Breast Acquisition: A Foundation for Multi- Parametric Imaging. Paper presented at: ISMRM 20162016; Singapore.
78. Baron CA, Dwork N, Pauly JM, Nishimura DG. Rapid compressed sensing reconstruction of 3D non-Cartesian MRI. *Magn Reson Med.* 2017.
79. Warner E. The role of magnetic resonance imaging in screening women at high risk of breast cancer. *Top Magn Reson Imaging.* 2008;19(3):163-169.
80. Houssami N, Ciatto S, Macaskill P, et al. Accuracy and surgical impact of magnetic resonance imaging in breast cancer staging: systematic review and meta-analysis in detection of multifocal and multicentric cancer. *J Clin Oncol.* 2008;26(19):3248-3258.
81. Chhor CM, Mercado CL. Abbreviated MRI Protocols: Wave of the Future for Breast Cancer Screening. *AJR Am J Roentgenol.* 2017;208(2):284-289.
82. Leithner D, Wengert GJ, Helbich TH, et al. Clinical role of breast MRI now and going forward. *Clin Radiol.* 2017.
83. Grimm LJ, Soo MS, Yoon S, Kim C, Ghate SV, Johnson KS. Abbreviated screening protocol for breast MRI: a feasibility study. *Acad Radiol.* 2015;22(9):1157-1162.
84. Harvey SC, Di Carlo PA, Lee B, Obadina E, Sippo D, Mullen L. An Abbreviated Protocol for High-Risk Screening Breast MRI Saves Time and Resources. *J Am Coll Radiol.* 2016;13(11S):R74-R80.
85. Moschetta M, Telegrafo M, Rella L, Stabile Ianora AA, Angelelli G. Abbreviated Combined MR Protocol: A New Faster Strategy for Characterizing Breast Lesions. *Clin Breast Cancer.* 2016;16(3):207-211.

86. Rapacchi S, Natsuaki Y, Plotnik A, et al. Reducing view-sharing using compressed sensing in time-resolved contrast-enhanced magnetic resonance angiography. *Magn Reson Med.* 2015;74(2):474-481.
87. Tsao J, Kozerke S. MRI temporal acceleration techniques. *J Magn Reson Imaging.* 2012;36(3):543-560.
88. Kazemi K, Moghaddam HA, Grebe R, Gondry-Jouet C, Wallois F. Design and construction of a brain phantom to simulate neonatal MR images. *Comput Med Imaging Graph.* 2011;35(3):237-250.
89. Kotasidis FA, Tsoumpas C, Polycarpou I, Zaidi H. A 5D computational phantom for pharmacokinetic simulation studies in dynamic emission tomography. *Comput Med Imaging Graph.* 2014;38(8):764-773.
90. Pan Y, Qiu R, Gao L, et al. Development of 1-year-old computational phantom and calculation of organ doses during CT scans using Monte Carlo simulation. *Phys Med Biol.* 2014;59(18):5243-5260.
91. Gaass T, Bauman G, Potdevin G, Noel PB, Haase A. Rapid dynamic radial MRI via reference image enforced histogram constrained reconstruction. *J Magn Reson.* 2014;240:1-7.
92. Tremoulheac B, Dikaios N, Atkinson D, Arridge SR. Dynamic MR image reconstruction-separation from undersampled (k,t)-space via low-rank plus sparse prior. *IEEE Trans Med Imaging.* 2014;33(8):1689-1701.
93. Velikina JV, Samsonov AA. Reconstruction of dynamic image series from undersampled MRI data using data-driven model consistency condition (MOCCO). *Magn Reson Med.* 2015;74(5):1279-1290.
94. Le Y, Kipfer H, Majidi S, et al. Application of Time-Resolved Angiography With Stochastic Trajectories (TWIST)-Dixon in Dynamic Contrast-Enhanced (DCE) Breast MRI. *Journal of Magnetic Resonance Imaging.* 2013;38(5):1033-1042.
95. Henze LC, Moran CJ, Smith MR, et al. Deterministic Comparisons of Nonlinear Acceleration Methods Using a Realistic Digital Phantom. Paper presented at: Proceedings of the 18th ISMRM Scientific Meeting 20102010; Stockholm Sweden.
96. Henze LC, Moran CJ, Smith MR, et al. Digital Breast Phantom for Evaluating Dynamic Accelerated Imaging Methods. Paper presented at: Proceedings of the 18th ISMRM Scientific Meeting 20102010; Stockholm Sweden.
97. Henze Bancroft LC, Wu D, Bosca RJ, et al. The Impact of Accelerated Imaging on Breast DCE MRI: Analysis of a 3D Radial Reconstruction using a Digital Breast Phantom. Paper presented at: ISMRM Workshop MRI in the Management of Breast Disease: Past, Present and Future2015; San Francisco, CA.
98. Jimenez JE, Strigel RM, Johnson KM, Henze Bancroft LC, Reeder SB, Block WF. Feasibility of high spatiotemporal resolution for an abbreviated 3D radial breast MRI protocol. *Magn Reson Med.* 2018.
99. Jimenez JE, Henze Bancroft LC, Strigel RM, Johnson KM, Reeder SB, Block WF. Non-Cartesian Compressed Sensing with Fat/Water Decomposition: Feasibility Study for High Performance Breast DCE-MRI. Paper presented at: ISMRM 23rd Annual Meeting June, 2015, 2015; Toronto, Canada.
100. Jimenez JE, Johnson KM, Henze Bancroft LC, Strigel RM, Reeder SB, Block WF. High Performance Volumetric 3T Breast Acquisition: A Foundation for Multi-Parametric Imaging. . Paper presented at: ISMRM 24rd Annual Meeting May, 2016, 2016; Singapore.
101. Jimenez JE, Johnson KM, Henze Bancroft LC, Strigel RM, Reeder SB, Block WF. 10 Second Temporal Resolution of Early Enhancement Visualization: Framework for Fast Breast MRI Screening. Paper presented at: ISMRM 25rd Annual Meeting Apri, 2017, 2017; Honolulu, Hawaii.
102. Knoll F, Schwarzl A, Diwoky C, D. S. gpuNUFFT - An Open-Source GPU Library for 3D Gridding with Direct Matlab Interface. Paper presented at: ISMRM 22rd Annual Meeting May, 2014, 2014; Milan, Italy.
103. Zhou W, Bovik AC, Sheikh HR, Simoncelli EP. Image quality assessment: from error visibility to structural similarity. *IEEE Transactions on Image Processing.* 2004;13(4):600-612.
104. Kumar B, Kumar SB, Kumar C. Development of improved SSIM quality index for compressed medical images. Paper presented at: Image Information Processing (ICIIP), 2013 IEEE Second International Conference on; 9-11 Dec. 2013, 2013.
105. Khalifa F, Soliman A, El-Baz A, et al. Models and methods for analyzing DCE-MRI: a review. *Med Phys.* 2014;41(12):124301.
106. Haygood TM, Wang J, Atkinson EN, et al. Timed efficiency of interpretation of digital and film-screen screening mammograms. *AJR Am J Roentgenol.* 2009;192(1):216-220.

107. Berns EA, Hendrick RE, Solari M, et al. Digital and screen-film mammography: comparison of image acquisition and interpretation times. *AJR Am J Roentgenol.* 2006;187(1):38-41.
108. Morrison CK, Henze Bancroft LC, DeMartini WB, et al. Novel High Spatiotemporal Resolution Versus Standard-of-Care Dynamic Contrast-Enhanced Breast MRI: Comparison of Image Quality. *Invest Radiol.* 2017;52(4):198-205.
109. Oldrini G, Fedida B, Poujol J, et al. Abbreviated breast magnetic resonance protocol: Value of high-resolution temporal dynamic sequence to improve lesion characterization. *Eur J Radiol.* 2017;95:177-185.
110. Mann RM, Mus RD, van Zelst J, Geppert C, Karssemeijer N, Platel B. A novel approach to contrast-enhanced breast magnetic resonance imaging for screening: high-resolution ultrafast dynamic imaging. *Invest Radiol.* 2014;49(9):579-585.
111. Platel B, Mus R, Welte T, Karssemeijer N, Mann R. Automated characterization of breast lesions imaged with an ultrafast DCE-MR protocol. *IEEE Trans Med Imaging.* 2014;33(2):225-232.
112. Pineda FD, Medved M, Wang S, et al. Ultrafast Bilateral DCE-MRI of the Breast with Conventional Fourier Sampling: Preliminary Evaluation of Semi-quantitative Analysis. *Acad Radiol.* 2016;23(9):1137-1144.
113. Abe H, Mori N, Tsuchiya K, et al. Kinetic Analysis of Benign and Malignant Breast Lesions With Ultrafast Dynamic Contrast-Enhanced MRI: Comparison With Standard Kinetic Assessment. *AJR Am J Roentgenol.* 2016;207(5):1159-1166.
114. Daly CP, Jaeger B, Sill DS. Variable appearances of fat necrosis on breast MRI. *AJR Am J Roentgenol.* 2008;191(5):1374-1380.